

Cover Page



Universiteit Leiden



The handle <http://hdl.handle.net/1887/49076> holds various files of this Leiden University dissertation

Author: Sediq, A.S.

Title: Analysis of sub-visible particles in complex injectable formulations

Issue Date: 2017-05-09

Analysis of sub-visible particles in complex injectable formulations



Ahmad Shakeb Sediq
احمد شكيب صديق

This research is supported by the Dutch Technology Foundation STW, which is part of the Netherlands Organisation for Scientific Research (NWO) and partly funded by the Ministry of Economic Affairs (project number 12144)

Printed by ProefschriftMaken, Vianen, the Netherlands

Analysis of sub-visible particles in complex injectable formulations

Ahmad Shakeb Sediq

Cover: 'Microsphere comet' by Frank Oosterhoff. Veins as city streets resembling a fractal pattern of nature. Fractal: a curve or geometrical figure, each part of which has the same statistical character as the whole

PhD thesis, with summary in Dutch

Leiden University, the Netherlands

April 2017

ISBN:

Copyright: © 2017 Ahmad Shakeb Sediq. All rights reserved. No part of this thesis may be reproduced or transmitted in any form or by any means without written permission of the author.

Analysis of sub-visible particles in complex injectable formulations

Analyse van niet-zichtbare deeltjes in complexe injecteerbare formuleringen
(met een samenvatting in het Nederlands)

Proefschrift

ter verkrijging van de graad van Doctor aan de Universiteit Leiden,
op gezag van Rector Magnificus Prof. Mr. C.J.J.M. Stolker,
volgens besluit van het College voor Promoties
te verdedigen op 9 mei 2017 des middag te 15.00 uur.

door

Ahmad Shakeb Sediq

Geboren op 12 februari 1985 te Kabul, Afghanistan

Promotors

Prof.dr. W. Jiskoot

Prof.dr. G.J. Witkamp

Co-promotor

Dr. M.R. Nejadnik

Promotiecommissie

Prof.dr. Hubertus Irth, Leiden University, LACDR, Chair

Prof.dr. Meindert Danhof, Leiden University, LACDR, Secretary

Prof.dr. D.J.A. Crommelin, Utrecht University

Prof.dr. H.W. Frijlink, Groningen University

Prof.dr. H. Mørck Nielsen, University of Copenhagen, Denmark

**To Narges,
for her unending patience,
support and **love**.**

Table of contents

Chapter 1	9
General introduction and thesis outline	
Chapter 2	21
No touching! Abrasion of adsorbed protein is the root cause of sub-visible particle formation during stirring	
Chapter 3	45
Protein-polyelectrolyte interactions: Monitoring particle formation and growth by nanoparticle tracking analysis and flow imaging microscopy	
Chapter 4	63
Determination of the porosity of PLGA microparticles by tracking their sedimentation velocity using a flow imaging microscope (FlowCAM)	
Chapter 5	85
A flow imaging microscopy based method using mass-to-volume ratio to derive the porosity of PLGA microparticles	
Chapter 6	103
A label-free method for cell counting and viability determination using flow imaging microscopy	
Chapter 7	127
Summary and perspectives	
Appendices	135
Nederlandse samenvatting	
List of publications	
<i>Curriculum vitae</i>	

General introduction and thesis outline



A.S. Sediq, M.R. Nejadnik, W. Jiskoot

Division of Drug Delivery Technology, Cluster BioTherapeutics, Leiden Academic Centre for Drug Research (LACDR), Leiden University, Leiden, The Netherlands

Since the early encounters of humans with snakebites, it was obvious that the parenteral route is a very pronounced and probably efficient way of drug administration. This observation and the use of poisoned arrows by ancient tribes were followed by the experiments of Sir Christopher Wren in the 17th century. With the use of a bladder and quill for a syringe and needle, he injected wine, ale, opium and other substances into the veins of dogs and studied their effects¹. Over the following centuries, technological improvements and increasing knowledge of physiology and pharmacy resulted in the development of injections and infusions as routine medical practices in hospitals.

Direct injection and infusion into the blood provide rapid action compared with other routes of administration where the drug has first to be absorbed. These methods allow for achievement of optimum levels of the drug in the blood accurately and immediately. Possibility of application of injections in case of unconsciousness or uncooperative state of the patient is another advantage of these methods. Additionally, drugs that undergo inactivation after oral administration are better off through injection or infusion. The latter is especially the case for therapeutic proteins and peptides, which are vulnerable to proteolytic degradation in the gastro-intestinal tract, besides being poorly absorbed.

Although the highly efficient protective barriers in other routes of administration (e.g., skin and mucous membranes) are circumvented with injections and infusions, the introduction of microorganisms, impurities and other toxic agents can be an accompanying risk for these methods of delivery. Therefore, parenteral preparations must be as impeccable as possible with respect to purity, freedom from toxicity and contamination. Specifically for therapeutic protein products, sub-visible particles (SVP) have received a lot of attention as impurities in protein formulations². These impurities in therapeutic protein drug products are divided into two well-studied categories: protein aggregates and non-proteinaceous particles originating from packaging materials or excipients^{3,4}. Due to importance of the issue, several methods have been developed that allow for quantification and characterization of SVP and visible particles⁵.

These methods are also used for characterization of particulate drug delivery systems (DDS) that are by design based on SVP⁶. Many types of particulate DDS are available that differ by the site of drug action and the method of particle delivery (local vs. systemic). The performance of DDS depends on their size, shape and surface characteristics^{7,8}. Therefore, characterization of these systems with high accuracy and detailed output is crucial in the formulation development and the overall safety and efficacy of the DDS in the clinic.

More recently, cell therapy products have entered the pharmaceutical arena⁹. In this case the drug substances themselves, *i.e.* the cells, are SVP¹⁰. As the clinical safety and effectiveness of these products depend on the concentration and viability of cells, it is of utmost importance to have quantification and characterization

methods in place during manufacturing, product distribution and prior to administration. This thesis deals with the characterization of SVP in the above-mentioned types of products. Below, these products are briefly discussed together with the role of analytical techniques used to characterize SVP in these products. The last section of this chapter provides a short description of the aims and outline of this thesis.

Therapeutic protein formulations

The highly specific and complex function of a protein cannot be mimicked by small molecules; therefore, therapeutic proteins have prominent advantages over small molecule drugs in terms of functionality. In principle, a protein's functionality is accompanied by a highly specific action and less adverse effects as compared to small molecules¹¹. During the past few decades, protein therapeutics have become increasingly important for the treatment of chronic and life-threatening diseases and conditions. In the year 2013, a total number of 338 monoclonal antibodies, 20 interferons, 93 other recombinant proteins and 250 vaccines were reported to be in various phases of clinical trials¹².

The complex and large structure of these macromolecules, however, make them susceptible to conformational changes in the structure of the protein. These changes may occur during the production of the bulk substance, the formulation, storage, transportation or other treatments that a protein goes through. Conformational changes can among others lead to aggregation of the protein in solution¹³. The presence of aggregated therapeutic protein greatly compromises product quality and potentially drug safety¹⁴. Presence of aggregates has been linked to reduced drug efficacy, serious adverse effects and even death¹⁵. One needs to clarify the currently accepted nomenclature for differently sized aggregates. Considering the fact that aggregates are particulate species we extend this nomenclature further into other injectable systems discussed throughout this thesis. Visible particles are classified as particles seen during visual inspection, typically above 100 μm . Particles in the micrometer range that are not detected during visible inspection are called SVP (1 – 100 μm). The nanometer range is divided into the submicrometer range (100 – 1000 nm) and the nanometer range (size-exclusion chromatography high-molecular-weight species) (< 100 nm)¹⁶. The particles that appear in therapeutic protein products in the SVP range can, in turn, be assigned into three categories: (1) extrinsic particles or contaminants (materials that are not part of the drug product, package and/or process); (2) intrinsic particles (undesirable, non-proteinaceous materials related to the manufacturing, packaging and/or device itself); and (3) inherent particles (protein aggregates or formulation components). Particulate impurities other than protein aggregates, such as excipients and packing materials, can influence the product quality as well. For instance, sugars of pharmaceutical-grade quality¹⁷ and surfactants (such as polysorbate 20)¹⁸ have been

shown to be the source of particulate impurities in drug products. Another example of intrinsic particulate impurities are silicone oil droplets which leach into the protein solution from the glass barrel and the plunger of prefilled syringes¹⁹. These droplets can get coated with the protein from the solution and agglomerate to increase turbidity in the protein solution^{20,21}. The latter example of the silicone oil droplet induced agglomeration in protein solution highlights the heterogeneous composition of particles in therapeutic protein products²². In addition, SVP are often a very heterogeneous population of micron sized aggregates, which in case of protein aggregates can consist of subpopulations of reversible, native aggregates and irreversible, unfolded aggregates¹⁶.

The use of analytical tools to count, size and identify the type of particles in therapeutic protein products is the most crucial component of understanding and controlling the presence of these species. The complexity in composition and subpopulations, as sketched above, brings several analytical challenges to the process. In addition, the choice of the analytical method for characterization of SPV depends on the stage of development, which determines the available amount of the product under consideration. The measurement principle of the techniques used for characterization of protein aggregates, determines the boundaries and limitations of each particular technique. Many of these techniques are able to size and quantify SVP in solution, but not to identify the composition or nature of the particle (e.g., proteinaceous or non-proteinaceous). To overcome analytical limitations and boundaries for characterization of protein aggregates, it makes sense to combine methods with different underlying principles²³.

Controlled release formulations

With respect to DDS we limit our work and discussion in this thesis to controlled release formulations in the SVP range, in particular microspheres. Microspheres are here defined as particulate systems where the drug is dispersed in the matrix of a carrier material. The aim of these drug products lies in the improvement in safety and/or efficacy of an active pharmaceutical ingredient (API). Rate-controlled and targeted release is often used as a tool to avoid toxic levels of an API in plasma while maintaining therapeutic concentrations for prolonged periods of time.

The aim of the STW project number 12144 was to develop a novel process for the coating of dry protein-containing cores with a shell consisting of oppositely charged polyelectrolytes (polymers containing charged or ionizable groups), and subsequently analytical methods to characterize and evaluate the performance of these DDS. Therefore in this thesis, particle characteristics of DDS based on hydrophilic polyelectrolyte complexes and hydrophobic polymers are studied. In polyelectrolyte complexes, the (mainly) electrostatic driven interaction of the polyelectrolyte (polymers containing charged or ionizable groups) with

the drug can lead to formation of controlled release particulate systems³⁰. In the category of hydrophobic drug carriers, poly lactic-co-glycolic acid (PLGA) is currently the most studied for small molecules and biologics, with almost 10 marketed drug products³¹. The great advantage of PLGA is its biocompatibility and biodegradability³² and the ability to modify the hydrophobicity by changing the lactic acid / glycolic acid ratio of the polymer³³. Particle characteristics are important quality attributes of microparticulate DDS that could affect the clinical performance of the product^{37,39}. For instance, the size and shape of the particles affect important quality parameters of product, such as release rate of the drug³⁷. Moreover, particle porosity has been reported to influence the loading and kinetics of the drug release³⁸. The latter will also be influenced by the extent and strength of interactions between the polymer and the drug.

Different techniques are available for studying shape, surface morphology and porosity of microspheres. Optical microscopy and scanning electron microscopy (SEM) are probably the most employed methods for studying particle shape, size and surface morphology. With respect to the measurement of the average size of microspheres, laser diffraction (LD) techniques are widely used as well. For the measurements of porosity, techniques employing gas adsorption and mercury intrusion are commonly used. In addition, SEM can be used to determine porosity when cryo-cutting techniques are used as a pretreatment for the particle-containing sample.

Cell therapy products

This field of pharmaceutical product development has its roots in human stem cell therapy and tissue and organ transplantations. Two main principles by which cells facilitate therapeutic action are recognized: (1) engraftment, differentiation and long term replacement of damaged tissue⁴⁰ and (2) release of cytokines, chemokines and growth factors to facilitate self-healing of an organ or region⁴¹. Currently a variety of products from multiple cell sources are approved for use⁴².

An important quality attribute of cell therapy products (CTP) is the concentration of viable cells, which in general are required to obtain the desired effect. These attributes (together with a purity and surface marker evaluation) are characteristics to be tested during different stages of CTP development. Moreover, in clinical practice the viability of the product needs to be attained before administration⁴³. As the manufacturing of CTP is becoming more sophisticated and complex, certain institutions, such as the US-based National Institute of Health (NIH) and National Heart, Lung and Blood Institute (NHLBI) have designed a so-called Production Assistance for Cellular Therapies (PACT) program to support researchers with the manufacturing⁴⁴.

From a formulation point of view there is currently very limited knowledge about what additives

to use for improving stability of the therapeutic compound (the cells), except for addition of osmotic agents such as NaCl. Several procedures during the production, transport, storage and even administration to the patient can potentially harm the cells and trigger cell death^{45,46}. Therefore, stability, consistency and comparability tests are performed to ensure that product potency is preserved under different circumstances encountered from production up to bedside administration⁴³. Many different cell assay analysis methods exist for cell viability determination. Nevertheless, the greatest challenge in CTP development is the inability to reliably characterize critical cell attributes. National Institute of Standards & Technology (NIST) has published an article on a number of strategies that could be used to ensure measurement confidence⁴⁷. Techniques employed for cell counting and viability determination vary in the nature of the test sample (e.g., starting material, in-process sample and final drug product) as well as in the required performance of the test. An assessment of viability without counting will be likely of little use and therefore a single method that provides both parameters will in most situations be the most efficient solution⁴⁷.

Methods to count cells mostly depend on the ability of the method to distinguish a cell from other particulates, such as visualization (e.g., microscopy), light scattering (e.g., flow cytometry) and electrical impedance. For measuring the concentration of viable cells, labeling with a fluorescent dye is normally required. Trypan blue⁴⁸ (passes the membrane of dead cells) and propidium iodide (passes ruptured cell membranes and becomes fluorescent upon binding nucleic acid⁴⁹) are frequently used dyes for this purpose. Two well-known cell viability assays are hemocytometry and flow cytometry. Hemocytometry is a very fast method to determine the total cell concentration and percent of (viable) cells in a sample that is spiked with a dye under a microscope⁴⁸. In a flow cytometer single cells from a cell suspension pass through the designated fluorescence and light scattering detectors. A scatter plot of the scattering signal (which is related to the type and size of the cell) and fluorescence signal (representing the viability) is plotted, and with that the percentage of viable cells can be derived. Flow cytometry-based methods can be very accurate and reproducible; however, determination of the cell concentration is not easily attained. Therefore, the search for new techniques and methods for qualitative and quantitative analysis of CTP may contribute to improved quality control of this emerging group of pharmaceutical products.

Aim and outline of this thesis

The aim of this thesis is to explore novel applications and capabilities of a number of particle analysis techniques to characterize complex injectable formulations, including (aggregated) protein solutions, protein-polyelectrolyte complexes, PLGA microspheres and cells. The outcome of our research should lead to (further)

application of these tools for characterization of complex injectable formulations and therewith improve the quality of pharmaceutical products used in modern healthcare. The research described in Chapter 2 concerns an investigation of the cause of stirring induced protein aggregation, in order to unravel the mechanism behind this well-known mechanical source of particle formation. To this end, size-exclusion chromatography, nanoparticle tracking analysis and Micro-Flow Imaging (MFI; a flow imaging microscope) were used. In Chapter 3, the same combination of analytical techniques is utilized to study the kinetics of the formation and growth of protein-polyelectrolyte complexes driven by electrostatic interactions.

In Chapter 4 and 5 novel applications of flow imaging microscopy techniques for the characterization of PLGA microspheres are introduced. The focus of Chapter 4 lies in investigating the ability of FlowCAM (a flow imaging microscope) to be used as a tool to analyze the sedimentation behavior of these particles, in order to deduce their porosity. In Chapter 5 MFI is used to measure the total volume of microspheres in a suspension with known microsphere concentration in order to determine the batch porosity of PLGA microspheres.

In Chapter 6 MFI- and FlowCAM-based label-free methods are presented for counting and assessing the viability of B-lineage acute lymphatic leukemia cells. Chapter 7 summarizes the main findings and conclusions of the work described in this thesis. In addition, the future of particle analysis techniques in the field of pharmaceutical formulation development is discussed.

References

1. Feldmann H 2000. History of injection. *Laryngorhinootologie* 79(4):7.
2. Carpenter JF, Randolph TW, Jiskoot W, Crommelin DJ, Middaugh CR, Winter G, Fan YX, Kirshner S, Verthelyi D, Kozlowski S, Clouse KA, Swann PG, Rosenberg A, Cherney B 2009. Overlooking subvisible particles in therapeutic protein products: gaps that may compromise product quality. *Journal of pharmaceutical sciences* 98(4):1201-1205.
3. Carpenter J, Cherney B, Lubinecki A, Ma S, Marszal E, Mire-Sluis A, Nikolai T, Novak J, Ragheb J, Simak J 2010. Meeting report on protein particles and immunogenicity of therapeutic proteins: filling in the gaps in risk evaluation and mitigation. *Biologicals* 38(5):602-611.
4. Singh SK, Afonina N, Awwad M, Bechtold-Peters K, Blue JT, Chou D, Cromwell M, Krause HJ, Mahler HC, Meyer BK, Narhi L, Nesta DP, Spitznagel T 2010. An Industry Perspective on the Monitoring of Subvisible Particles as a Quality Attribute for Protein Therapeutics. *Journal of pharmaceutical sciences* 99(8):3302-3321.
5. Zölls S, Tantipolphan R, Wiggenhorn M, Winter G, Jiskoot W, Friess W, Hawe A 2012. Particles in therapeutic protein formulations, Part 1: overview of analytical methods. *Journal of*

pharmaceutical sciences 101(3):914-935.

6. Kohane DS 2007. Microparticles and nanoparticles for drug delivery. *Biotechnol Bioeng* 96(2):203-209.
7. He Y, Park K 2016. Effects of the Microparticle Shape on Cellular Uptake. *Molecular pharmaceuticals* 13(7):2164-2171.
8. Patino T, Soriano J, Barrios L, Ibanez E, Nogues C 2015. Surface modification of microparticles causes differential uptake responses in normal and tumoral human breast epithelial cells. *Sci Rep* 5:11371.
9. Mason C, Brindley DA, Culme-Seymour EJ, Davie NL 2011. Cell therapy industry: billion dollar global business with unlimited potential. *Regen Med* 6(3):265-272.
10. Mount NM, Ward SJ, Kefalas P, Hyllner J 2015. Cell-based therapy technology classifications and translational challenges. *Philos Trans R Soc Lond B Biol Sci* 370(1680):20150017.
11. Leader B, Baca QJ, Golan DE 2008. Protein therapeutics: a summary and pharmacological classification. *Nature reviews Drug discovery* 7(1):21-39.
12. PhRMA. 2013. *Biologic Medicines in Development*. ed., Washington DC: PhRMA. p 8.
13. Frokjaer S, Otzen DE 2005. Protein drug stability: a formulation challenge. *Nature reviews Drug discovery* 4(4):298-306.
14. Shekunov BY, Chattopadhyay P, Tong HH, Chow AH 2007. Particle size analysis in pharmaceuticals: principles, methods and applications. *Pharmaceutical research* 24(2):203-227.
15. Services UDoHaH. 2009. Q4B Evaluation and Recommendation of Pharmacopoeial Texts for Use in the ICH Regions Annex 3 Test for Particulate Contamination: Subvisible Particles General Chapter. In Administration FaD, editor, ed., Rockville: USDHHS.
16. Narhi LO, Schmit J, Bechtold-Peters K, Sharma D 2012. Classification of protein aggregates. *Journal of pharmaceutical sciences* 101(2):493-498.
17. Weinbuch D, Cheung JK, Ketelaars J, Filipe V, Hawe A, den Engelsman J, Jiskoot W 2015. Nanoparticulate Impurities in Pharmaceutical-Grade Sugars and their Interference with Light Scattering-Based Analysis of Protein Formulations. *Pharmaceutical research* 32(7):2419-2427.
18. Tomlinson A, Demeule B, Lin B, Yadav S 2015. Polysorbate 20 Degradation in Biopharmaceutical Formulations: Quantification of Free Fatty Acids, Characterization of Particulates, and Insights into the Degradation Mechanism. *Molecular pharmaceuticals* 12(11):3805-3815.
19. Chantelau E, Berger M, Bohlken B 1986. Silicone oil released from disposable insulin syringes. *Diabetes Care* 9(6):672-673.
20. Jones LS, Kaufmann A, Middaugh CR 2005. Silicone oil induced aggregation of proteins. *Journal of pharmaceutical sciences* 94(4):918-927.
21. Thirumangalathu R, Krishnan S, Ricci MS, Brems DN, Randolph TW, Carpenter JF 2009. Silicone oil- and agitation-induced aggregation of a monoclonal antibody in aqueous solution.

Journal of pharmaceutical sciences 98(9):3167-3181.

22. Ripple DC, Dimitrova MN 2012. Protein particles: What we know and what we do not know. Journal of pharmaceutical sciences 101(10):3568-3579.

23. Filipe V, Hawe A, Carpenter JF, Jiskoot W 2013. Analytical approaches to assess the degradation of therapeutic proteins. *Trac-Trend Anal Chem* 49:118-125.

24. Cao S, Jiang, Y., Narhi, L. 2010. A light obscuration method specific for quantifying subvisible particles in protein therapeutics. *Pharm Forum* 36(3).

25. Werk T, Volkin DB, Mahler HC 2014. Effect of solution properties on the counting and sizing of subvisible particle standards as measured by light obscuration and digital imaging methods. *European journal of pharmaceutical sciences : official journal of the European Federation for Pharmaceutical Sciences* 53:95-108.

26. Weinbuch D, Zölls S, Wiggenghorn M, Friess W, Winter G, Jiskoot W, Hawe A 2013. Micro-flow imaging and resonant mass measurement (Archimedes)--complementary methods to quantitatively differentiate protein particles and silicone oil droplets. *Journal of pharmaceutical sciences* 102(7):2152-2165.

27. Narhi LO, Jiang Y, Cao S, Benedek K, Shnek D 2009. A critical review of analytical methods for subvisible and visible particles. *Curr Pharm Biotechnol* 10(4):373-381.

28. Corvari V, Narhi LO, Spitznagel TM, Afonina N, Cao S, Cash P, Cecchini I, DeFelippis MR, Garidel P, Herre A, Koulov AV, Lubiniecki T, Mahler HC, Mangiagalli P, Nesta D, Perez-Ramirez B, Polozova A, Rossi M, Schmidt R, Simler R, Singh S, Weiskopf A, Wuchner K 2015. Subvisible (2-100 µm) particle analysis during biotherapeutic drug product development: Part 2, experience with the application of subvisible particle analysis. *Biologicals* 43(6):457-473.

29. Kliche W, Herre, A., Garidel, P. 2012. Microscopic methods for particle characterisation in protein pharmaceuticals *Analysis of aggregates and particles in protein pharmaceuticals*, ed., New Jersey: John Wiley & Sons.

30. Tong WJ, Song XX, Gao CY 2012. Layer-by-layer assembly of microcapsules and their biomedical applications. *Chem Soc Rev* 41(18):6103-6124.

31. Mundargi RC, Babu VR, Rangaswamy V, Patel P, Aminabhavi TM 2008. Nano/micro technologies for delivering macromolecular therapeutics using poly(D,L-lactide-co-glycolide) and its derivatives. *J Control Release* 125(3):193-209.

32. Freiberg S, Zhu XX 2004. Polymer microspheres for controlled drug release. *International journal of pharmaceutics* 282(1-2):1-18.

33. Anderson JM, Shive MS 2012. Biodegradation and biocompatibility of PLA and PLGA microspheres. *Adv Drug Deliver Rev* 64:72-82.

34. Patil SD, Burgess, D.J. 2010. Pharmaceutical development of modified-release parenteral dosage forms using bioequivalence (BE), Quality by Design (QbD), and In Vitro In Vivo Correlation (IVVC) principles. In Shargel L, Kanfer, I., editor *Generic drug product development speciality*

dosage forms, ed., New York: Informa Healthcare USA, Inc. p 26.

- 35.** Zidan AS, Habib MJ, Khan MA 2008. Process analytical technology: nondestructive evaluation of cyclosporine A and phospholipid solid dispersions by near infrared spectroscopy and imaging. *Journal of pharmaceutical sciences* 97(8):3388-3399.
- 36.** idan AS, Sammour OA, Hammad MA, Megrab NA, Habib MJ, Khan MA 2008. Process analytical technology: non-destructive assessment of anastrozole entrapment within PLGA microparticles by near infrared spectroscopy and chemical imaging. *J Microencapsul* 25(3):145-153.
- 37.** Kumar R, Palmieri MJ 2010. Points to Consider when Establishing Drug Product Specifications for Parenteral Microspheres. *Aaps Journal* 12(1):27-32.
- 38.** Klose D, Siepmann F, Elkharraz K, Krenzlin S, Siepmann J 2006. How porosity and size affect the drug release mechanisms from PLIGA-based microparticles. *International journal of pharmaceutics* 314(2):198-206.
- 39.** Martinez M, Rathbone M, Burgess D, Huynh M 2008. In vitro and in vivo considerations associated with parenteral sustained release products: a review based upon information presented and points expressed at the 2007 Controlled Release Society Annual Meeting. *J Control Release* 129(2):79-87.
- 40.** Jackson KA, Majka SM, Wang H, Pocius J, Hartley CJ, Majesky MW, Entman ML, Michael LH, Hirschi KK, Goodell MA 2001. Regeneration of ischemic cardiac muscle and vascular endothelium by adult stem cells. *J Clin Invest* 107(11):1395-1402.
- 41.** Yagi H, Soto-Gutierrez A, Parekkadan B, Kitagawa Y, Tompkins RG, Kobayashi N, Yarmush ML 2010. Mesenchymal stem cells: Mechanisms of immunomodulation and homing. *Cell transplantation* 19(6):667-679.
- 42.** Administration UFaD. 2016. Marketed cellular, tissue and gene therapy products. ed.: US Department of Health and Human Services.
- 43.** Stroncek DF, Jin P, Ren J, Feng J, Castiello L, Civini S, Wang E, Marincola FM, Sabatino M 2010. Quality assessment of cellular therapies: the emerging role of molecular assays. *Korean J Hematol* 45(1):14-22.
- 44.** Lindblad RW, Ibenana L, Wagner JE, McKenna DH, Hei DJ, Hematti P, Couture LA, Silberstein LE, Armant M, Rooney CM, Gee AP, Welniak LA, Mondoro TH, Wood DA, Styers D 2015. Cell therapy product administration and safety: data capture and analysis from the Production Assistance for Cellular Therapies (PACT) program. *Transfusion* 55(3):674-679.
- 45.** Moviglia GA, Vina RF, Brizuela JA, Saslavsky J, Vrsalovic F, Varela G, Bastos F, Farina P, Etchegaray G, Barbieri M, Martinez G, Picasso F, Schmidt Y, Brizuela P, Gaeta CA, Costanzo H, Brandolino MM, Merino S, Pes ME, Veloso MJ, Rugilo C, Tamer I, Shuster GS 2006. Combined protocol of cell therapy for chronic spinal cord injury. Report on the electrical and functional recovery of two patients. *Cytotherapy* 8(3):202-209.

- 46.** Leverett LB, Hellums JD, Alfrey CP, Lynch EC 1972. Red blood cell damage by shear stress. *Biophysical journal* 12(3):257-273.
- 47.** Simon CG, Lin-Gibson S, Elliott JT, Sarkar S, Plant AL 2016. Strategies for Achieving Measurement Assurance for Cell Therapy Products. *Stem Cell Transl Med* 5(6):705-708.
- 48.** Strober W 2001. Trypan blue exclusion test of cell viability. *Current protocols in immunology* / edited by John E Coligan [et al] Appendix 3:Appendix 3B.
- 49.** Riccardi C, Nicoletti I 2006. Analysis of apoptosis by propidium iodide staining and flow cytometry. *Nature protocols* 1(3):1458-1461.

No Touching! **Abrasion of Adsorbed Protein is the Root Cause of** **Sub-Visible Particle Formation during Stirring**



A.S. Sediq¹, R.B. van Duijvenvoorde¹, W. Jiskoot^{1,*}, M.R. Nejadnik^{1,*}

¹ Division of Drug Delivery Technology, Leiden Academic Centre for Drug Research (LACDR), Leiden University, Leiden, the Netherlands

The chapter was published in the *Journal of Pharmaceutical Sciences*:
J Pharm Sci 2016 105: 519-529

Abstract

This study addressed the effect of contact sliding during stirring of a monoclonal antibody solution on protein aggregation, in particular in the nano- and micrometer size range. An overhead stirring set-up was designed in which the presence and magnitude of the contact between the stir bar and the container could be manipulated. A solution of 0.1 mg/mL of a monoclonal antibody (IgG) in PBS was stirred at 300 rpm at room temperature. At different time points, samples were taken and analyzed by nanoparticle tracking analysis, flow imaging microscopy and size-exclusion chromatography. In contrast to non-contact stirred and unstirred samples, the contact stirred sample contained several-fold more particles and showed a significant loss of monomer. No increase in oligomer content was detected. The number of particles formed was proportional to the contact area and the magnitude of the normal pressure between the stir bar and the glass container. Extrinsic DCVJ fluorescence indicated a conformational change for contact stirred protein samples. Presence of polysorbate 20 inhibited the formation of micron sized aggregates. We suggest a model in which abrasion of the potentially destabilized, adsorbed protein leads to aggregation and renewal of the surface for adsorption of a fresh protein layer.

Introduction

Therapeutic proteins have gained a paramount place in modern pharmaceuticals, accounting for more than 70% of the total revenue generated by the ten best-selling pharmaceuticals¹. The share of therapeutic proteins in the pharmaceuticals under development is also getting bigger while the probability of regulatory approval from entering clinical development is 32% for therapeutic proteins versus 13% for small-molecule drugs^{2,3}. In this category of pharmaceuticals, monoclonal antibodies account for almost half of the sales⁴. The benefits of therapeutic monoclonal antibodies have been proven to be of great value in many life-threatening diseases including cancer, inflammatory and immune diseases, such as rheumatoid arthritis^{5,6}.

Despite this important role of therapeutic proteins in pharmacotherapy, their marginal stability remains an important challenge in formulation, storage, shipping, and delivery of these drugs. Stability issues very often imply aggregation of proteins, which could lead to immunogenicity^{7,8} and/or reduced efficacy of the drug⁹. Therefore, regulatory authorities have developed guidelines for quality control of protein drug formulations which often contain upper limits for the concentration of visible and sub-visible particles (including protein aggregates) present in parenteral drug products¹⁰⁻¹².

Many external factors that cause the aggregation of therapeutic proteins have been identified^{13,14}. Among those, mechanical stresses in form of shaking and stirring of liquid protein formulations¹⁵⁻²¹ have been shown to potentially induce considerable amounts of protein aggregates. These types of stress factors are encountered commonly at different stages from manufacturing process up to bedside administration to the patient. Recently, Kiese et al. showed that stirring of a liquid IgG1 formulation results in large numbers of micron sized aggregates, whilst the consequence of shaking was limited to formation of (high-molecular-weight) oligomers and was dependent on presence of an air-filled headspace in a bottle¹⁵. It was also shown that polysorbate 20 had a protective effect on antibody formulations against aggregation. The authors have listed several parameters, including shear, interfacial effects, and cavitation, that could potentially lead to severe aggregation of protein during stirring. Bee et al. ruled out the effect of high shear force on the aggregation of an antibody²². There are studies that have addressed the effects of other parameters on protein aggregation, however, the exact underlying mechanism of stirring stress-induced aggregation is still not fully understood.

In a typical stirring-stress study, stirring involves a constant contact sliding of the surface of a stir bar against the solid surface of a container. Such contact would disturb a critical solid-liquid interface that is a target for protein adsorption. Interestingly, however, to our knowledge the effect of the contact sliding of the solid surfaces, as present during the stirring, on aggregation of proteins has not been investigated.

In this study, we addressed the effect of contact sliding during stirring of a liquid monoclonal antibody protein formulation on aggregation of the protein. For this purpose a stirring configuration has been designed in which the presence, magnitude, and normal pressure of the contact between the solid surfaces can be manipulated. The aggregation of the antibody was monitored by size-exclusion chromatography, nanoparticle tracking analysis, and flow imaging microscopy. Our results indicate that contact sliding-triggered abrasion of adsorbed protein is the key to the formation of micron sized aggregates induced by stirring.

Materials and Methods

Materials

Phosphate buffered saline (PBS; 8.2 g/L NaCl, 3.1 g/L Na₂HPO₄·12H₂O, 0.3 g/L NaH₂PO₄·2H₂O, pH 7.4) was obtained from Braun (B. Braun Melsungen AG, Germany) and filtered by using a 0.22- μ m polyethersulfone-based syringe driven filter unit (Millex GP, Millipore, Carrigtwohill, Ireland). Polysorbate 20, sodium phosphate dibasic dihydrate, sodium phosphate monobasic dihydrate, sodium azide, sodium sulfate and 9-(2,2-dicyanovinyl) julolidine (DCVJ) were obtained from Sigma (Sigma-Aldrich, Steinheim, Germany). Ethanol was purchased from Biosolve (Biosolve B.V., Valkenswaard, The Netherlands). Ultrapure water (18.2 M Ω .cm) was dispensed by using a Purelab Ultra water purification system (ELGA LabWater, Marlow, UK). A monoclonal human IgG1 (IgG), formulated at 65 mg/mL in 10 mM sodium citrate buffer containing 5% sucrose at pH 6.0 as described before²³⁻²⁵, was used as a model protein. This stock solution was diluted to a concentration of 0.1 mg/mL IgG in PBS, either with or without 0.01% (w/v) polysorbate 20. In addition, a solution of 0.5 mg/mL IgG in PBS without polysorbate 20 was also prepared. Furthermore, a monoclonal human antibody of the IgG1 subclass (IgG-BI), kindly provided by Boehringer Ingelheim (Biberach, Germany), myoglobin (from equine skeletal muscle) and bovine serum albumin (BSA), both purchased from Sigma (Sigma-Aldrich, Steinheim, Germany), were used as model proteins in a small set of experiments.

Mechanical stress conditions

The stirring stress was generated at room temperature by magnetic stirring or an in-house designed overhead stirring system. For the magnetic stirring system a Teflon-coated stir bar with a diameter of 8 mm and a length of 40 mm, a flat-bottom crystallizing glass (diameter of 70 mm) (cat. no. 2131141; Duran; Schott, Mainz, Germany) and a magnetic stirrer (RCT basic IKAMAG, IKA-Werke GmbH, Staufen, Germany), operating at a constant rate of 300 rpm, were used. The overhead stirring system (Figure 1) was used to study the effects of surface contact, contact area, and force generated by the stir bar on the glass surface. For this series of experiments a rod was used to fix an in-house designed stir bar made of

polyether ether ketone. The shape and dimensions of this bar were similar to the one used with magnetic stirring experiments. The effect of surface contact was investigated by stirring 80 mL of IgG solution at 300 rpm while the stir bar contact slid over the glass surface. A balance placed underneath the glass container was used to monitor the force applied by the stir bar (force calculated through multiplication of the displayed mass and gravitational force), which was in this case 5.88 N. Similarly, non-contact stirring was performed by stirring with 5 mm space between the stir bar and the surface of the glass container. As negative control an equal amount of IgG solution was left for 270 min unstirred in the same type of crystallizing glass at room temperature. An additional control consisted of stirring with contact sliding (or magnetic stirring) of protein free PBS.

All the above-mentioned stirring conditions were applied for polysorbate-free IgG solutions. In addition, the contact sliding stirring experiments were performed with polysorbate-containing IgG solutions.

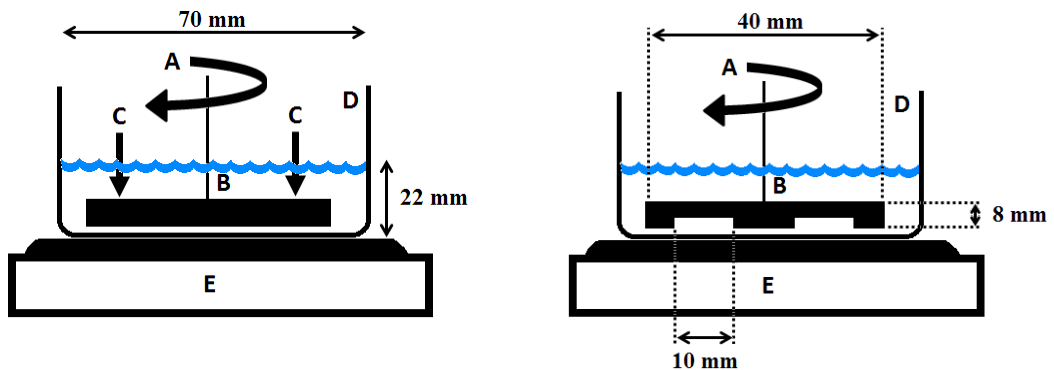


Figure 1: Scheme of the experimental set-up for the overhead stirring system used in this study. The rotor (A) turned the stir bar (B) with a rotation speed of 300 rpm, while the normal force (C) applied to the bottom of the glass container (D) during the contact mode was monitored by the balance (E). Stirring in the absence of any contact was performed by rotating the stir bar at a distance of ~5 mm from the bottom of the container. Bottom figure: the system with a reduced contact area by using a stir bar with cavities on its lower surface.

stirring with 5 mm space between the stir bar and the surface of the glass container. As negative control an equal amount of IgG solution was left for 270 min unstirred in the same type of crystallizing glass at room temperature. An additional control consisted of stirring with contact sliding (or magnetic stirring) of protein free PBS. All the above-mentioned stirring conditions were applied for polysorbate-free IgG solutions. In addition, the contact sliding stirring experiments were performed with polysorbate-containing IgG solutions. In order to investigate the effect of the contact area, a modified stir bar with the same dimensions, but half the contact area, was used while the normal force upon contact was reduced to 2.94 N to keep the applied pressure the same. In addition, the stir bar with full contact

area was used with a reduced normal force of 1.96 N, to study the effect of pressure. The samples were taken at different time points according to the scheme depicted in Figure 2 and immediately analyzed.

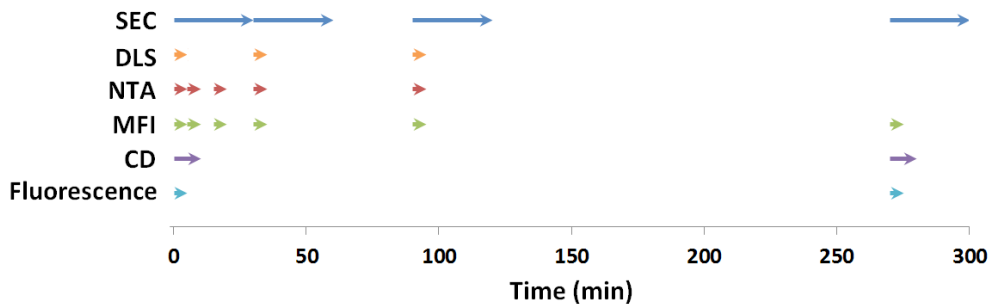


Figure 2: Schematic overview of the sampling time points for each type of measurement performed in this study. The length of each rod indicates the approximate analysis time per sample, including sample pretreatment and handling.

In order to investigate whether the results are applicable to other antibodies and proteins, the contact and non-contact stirring together with the negative control experiments were also performed with three other protein solutions, namely 0.1 mg/mL BSA, 0.1 mg/mL IgG-BI and 0.5 mg/mL myoglobin, all in PBS.

Size-exclusion chromatography

High pressure size-exclusion chromatography (SEC) was performed to quantify the amount of IgG monomer and oligomers in the unstressed and mechanically stressed samples. This was executed on an Agilent 1200 chromatography system (Agilent Technologies, Palo Alto, California) combined with a Wyatt Eclipse (Wyatt Technology Europe GmbH, Dernbach, Germany). A Yarra 3 μm SEC-2000 column (300 \times 7.8 mm) coupled with a Yarra Security Guard precolumn (Phenomenex, Torrance, CA, USA) was used. One mL of the samples was centrifuged (18,000 \times g for 15 minutes) to remove large particles and 100 μL of the supernatants were injected, while separation was performed at a flow rate of 0.5 mL/min. The mobile phase consisted of 100 mM sodium phosphate, 100 mM sodium sulfate, and 0.05 % w/v sodium azide at pH 7.2. Ultraviolet absorption detection was performed at 280 nm. In order to calculate the monomer decrease after stress, the areas under the curve (AUC) of the UV signal of the monomer peak were used. Standard curves were obtained by using pure IgG samples of known concentrations.

Dynamic light scattering

DLS measurements were performed with a Malvern Zetasizer Nano ZS (Malvern, Herrenberg, Germany). For the collection and analysis of data the Dispersion Technology

Software version 7.03 from Malvern was used. Five hundred μL of each sample was measured in single-use polystyrene half-micro cuvettes (Fischer Emergo, Landsmeer, The Netherlands) with a path length of 10 mm.

Nanoparticle tracking analysis

Nanoparticle tracking analysis (NTA) was performed with a NanoSight LM20 (NanoSight Ltd., Amesbury, United Kingdom) equipped with a 640 nm laser and operating at an angle of 173° with respect to the flow cell (100 x 80 x 10 μm). Samples were injected into the chamber by an automatic pump (Harvard Apparatus, catalog no. 98-4362, Holliston, USA) using a sterile 1-mL syringe (BD Discardit II, Franklin Lakes, New Jersey). The settings were optimized for NTA analysis of solutions containing high quantities of micrometer sized particles, based on a previous study²⁶. For each sample a 90 s video was captured with the shutter set at 1495 and the gain at 400. Videos were analyzed by using the NTA 2.0 Build 127 software. The following settings were used for tracking of the particles: background extract on; brightness 0; gain 1.00; blur size 3x3; detection threshold 10, viscosity equal to that of water. All other parameters were set to the automatic adjustment mode. Only particles in the 100 – 800 nm size range were included in the analysis.

Flow imaging microscopy

A Micro-Flow Imaging (MFI) system (MFI5200, ProteinSimple, Santa Clara, USA), equipped with a silane coated flow cell (1.41 x 1.76 x 0.1 mm) and controlled by the MFI View System Software (MVSS) version 2, was used for flow imaging microscopy analysis. The system was flushed with 4 mL purified water at 6 mL/min prior to each measurement. The flow cell cleanliness was checked visually between measurements. The background was zeroed by flowing PBS and performing the 'optimize illumination' procedure. Samples of 0.5 mL with a pre-run volume of 0.2 mL were analyzed at a flow rate of 0.17 mL/min and a fixed camera shot rate of 22 flashes per second. The data recorded by the MVSS was analyzed with MFI View Analysis Suite (MVAS) version 1.2. For each sample, stuck, edge, and slow-moving particles were removed by the software before data analysis. The equivalent circular diameter (ECD), which is the diameter of a circle that has an area equal to that of the particle imaged by MFI, was calculated and presented as a measure of the particle size (1-100 μm).

Circular dichroism

Far-UV circular dichroism (CD) was used to study the secondary structure of the protein before and after stirring. The measurements were performed with a Jasco J-815 CD spectrometer in combination with a Jasco PTC- 423S temperature controller (Jasco International,

Tokyo, Japan) at 25°C. The samples were measured in quartz cuvettes (Hellma GmbH, Muellheim, Germany) with a path length of 1 mm. Circular dichroism spectra were collected in a continuous scanning mode from 200 to 250 nm. The measurements were performed at a scanning speed of 50 nm/min, a response time of 2 s, a bandwidth of 1 nm, a sensitivity of 100 m°, steps of 0.5 nm, and an accumulation of 6 scans. Using the Spectra Analysis Software (version 1.53.04, Jasco), the spectra were background corrected by subtracting the spectrum of the buffer. Data were calculated to mean residue ellipticity according to previously described equations²⁵ by using a mean amino acid residue weight of 113.

Intrinsic and extrinsic fluorescence spectroscopy

Intrinsic and extrinsic fluorescence measurements were conducted with an FS920 fluorescence spectrometer (Edinburgh Instruments, Edinburgh, UK) at 25 °C using quartz cuvettes with a path length of 10 mm. For intrinsic fluorescence measurements, tryptophan was selectively excited at 295 nm. Changes in emission spectra will reveal alterations in the tertiary structure of IgG²⁷. The emission spectra were recorded from 300 to 500 nm using emission and excitation slits of 3 nm, a dwell time of 0.5 s, steps of 0.5 nm, and a cumulative addition of three scans for each spectrum. All spectra were corrected by subtracting the emission spectrum of the buffer measured under the same conditions as the samples. For extrinsic fluorescence spectroscopy DCVJ was used, which allows detection of changes in protein structure²⁸, also in polysorbate-containing solutions²⁹. For this part of the study an additional stress condition (thermal stress) was incorporated as a positive control, in order to get a general idea on the relative extent of the conformational changes introduced by stirring stress²⁹. To induce thermal stress, 1.5 mL of polysorbate-containing and polysorbate-free IgG solutions were heated for 10 minutes at 75°C in a 1.5-ml reaction tubes (Eppendorf, Hamburg, Germany) using a thermomixer (Eppendorf, Hamburg, Germany). The aggregation of antibodies under these conditions was thoroughly investigated previously and is reported elsewhere^{23,25,29}. The used temperature was aggregation onset temperature of the IgG and no visible precipitation was observed after this treatment. For each tested condition 50 µL of a 100 µM DCVJ stock solution was added to 950 µL protein solution to achieve a dye concentration of 5 µM. IgG/DCVJ mixtures were measured within 30 min after dye addition. DCVJ was excited at 452 nm and an emission scan from 470 to 650 nm was performed. The measurements were performed with slits of 3 nm, steps of 1 nm and a dwell time of 0.5 second.

Results

Protein aggregation induced by magnetic stirring

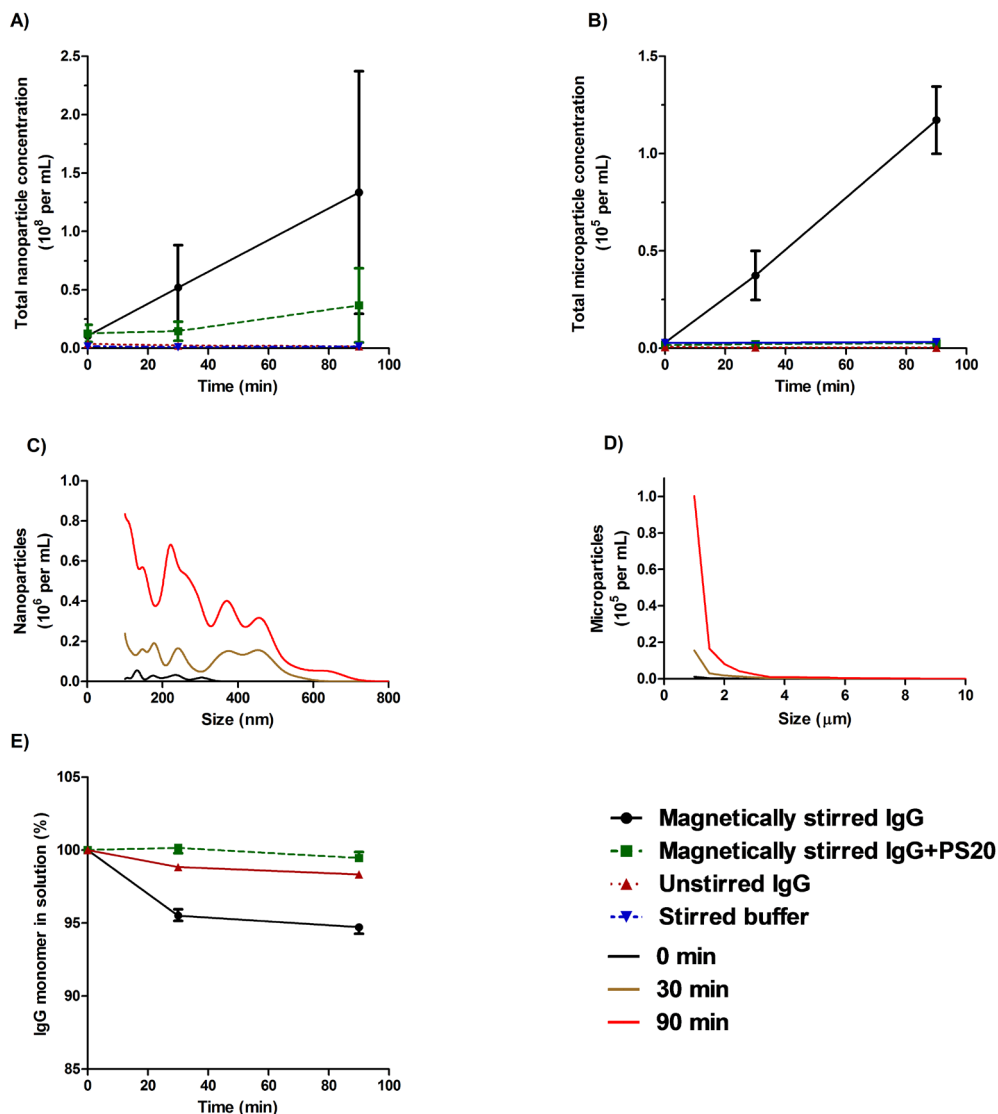


Figure 3: Effect of magnetic stirring on protein aggregation. Aggregation was monitored as function of time for magnetically stirred IgG solution (contact stirring) with and without 0.01% polysorbate 20 (PS20), unstirred IgG solution, and stirred PBS. Plots show the total concentrations of A) nanometer sized particles as measured by NTA and B) micron sized particles as measured by MFI; C) nanometer particle size distribution of contact stirred solution as measured by NTA and D) micrometer particle size distribution of contact stirred solution as measured by MFI; E) percentages of monomeric IgG still in solution as measured by SEC. All the graphs show the average and standard deviation of triplicate experiments, except for panel C and D, which show the results of one of the replicates.

Magnetic stirring of IgG solution for 90 min resulted in the formation of large numbers of particles in the size range of about 100 nm to 3 μm , as detected by NTA and MFI (Figure 3A-B). In particular, the formation of up to 135,000 micron sized particles per mL with a consistent average size of 1.60 μm and an irregular shape (Figure 4) was observed by MFI.




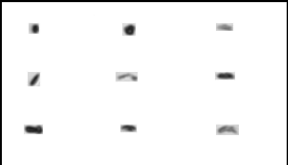



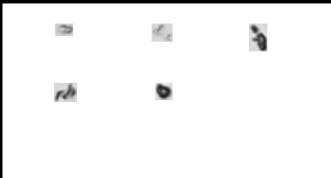

	Magnetically stirred	Non-contact stirred	Contact stirred
5 - 10 μm			
10 - 15 μm			
15 - 25 μm			

Figure 4: Examples of MFI images of particles detected in magnetically stirred (after 90 min), non-contact stirred (after 270 min) and contact stirred (after 270 min and 5.88 N pressure) IgG solutions.

The number of particles increased over time and stirring led to generation of more nanometer- and micron sized particles continuously (Figure 3C-D). SEC analysis revealed a decrease of more than 5 % in monomer content after 90 min, but no increase in the amount of (high molecular weight) oligomers, as shown in Figure 3E and 5. DLS measurements revealed an increase in the Z-average diameter and PDI already in the first measurement after the start of magnetic stirring (results not shown). Since DLS analysis was not sufficiently distinctive for samples containing substantial numbers of micron sized particles, it was not used for follow-up experiments.

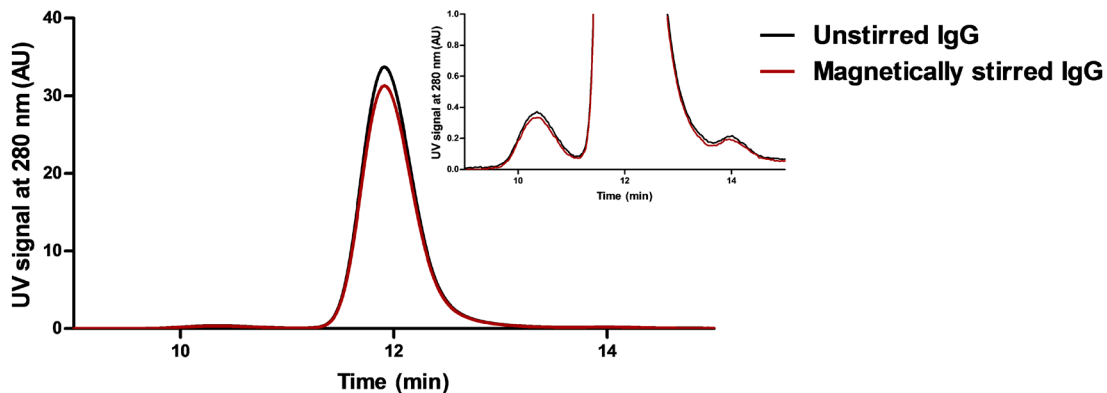


Figure 5: Representative SEC chromatograms of unstirred and magnetically stirred IgG solution. The insert shows a zoom-in view of the monomer and oligomer peak.

Unstirred IgG solution and stirred placebo solution (PBS) did not show any particle formation. Stirred IgG solution containing 0.01% polysorbate 20 did not exhibit any increase in the number of micron sized particles (MFI, Figure 3B) or monomer loss (SEC, Figure 3E), but did show an increase over time in nanometer sized particles (NTA, Figure 3A), albeit to a lesser extent than the stirred polysorbate-free IgG solution.

Effect of contact sliding on protein aggregation and micron sized particle formation

In this part of the study we employed an overhead stirring system, where the contact of the stir bar with the container surface could be manipulated (Figure 1). NTA and MFI analysis indicated that stirring with contact sliding of polysorbate-free IgG solution created high numbers of particles. At this stirring condition the average total nanometer sized particle concentration increased from 0.1×10^8 per mL at $t = 0$ to 1.8×10^8 per mL after 90 minutes, as observed by NTA (Figure 6A and C). Moreover, MFI showed an increase in the average total micron sized particle concentration from about 1000 ($t = 0$) up to 1.7×10^6 per mL with an average particle size of $1.78 \mu\text{m}$ after 270 min of stirring (Figure 6B and D), while SEC showed a 10% decrease of IgG monomer content in solution (Figure 6E). In contrast, non-contact stirred protein solution showed only a minor increase in both nanometer- and micron sized particle counts, without a significant decrease in monomer content. For both contact and non-contact stirred samples, particles with a size above $5 \mu\text{m}$ had irregular shapes (Figure 4).

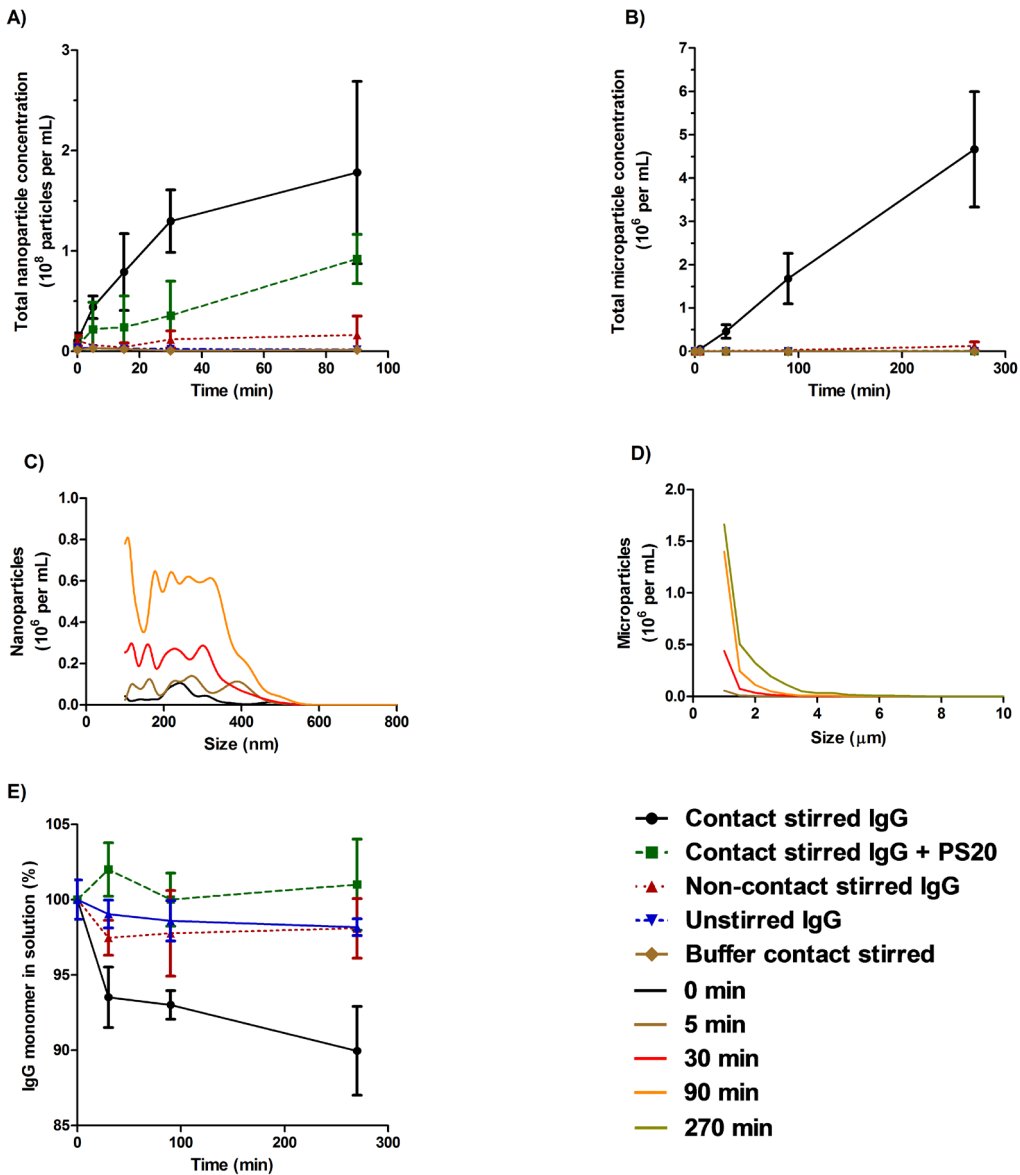


Figure 6: Effect of contact stirring and non-contact stirring on protein aggregation.

Aggregation was monitored as function of time for IgG solution with and without 0.01% polysorbate 20 (PS20) stirred with contact sliding of the stir bar over the glass surface (pressure 5.88 N), IgG solution without polysorbate 20 stirred without contacting the glass, unstirred IgG solution, and stirred PBS. Plots show the total concentration of A) nanometer sized particles of contact stirred solution as measured by NTA and B) micron sized particles of contact stirred solution as measured by MFI; C) nanometer particle size distribution as measured by NTA and D) micrometer particle size distribution as measured by MFI; E) percentages of monomeric IgG still in solution as measured by SEC. All the graphs show the average and standard deviation of triplicate experiments, except for panel C and D, which show the results of one of the replicates.

The results for unstirred IgG, contact stirred PBS and contact stirred polysorbate-containing IgG solution were very similar to those obtained for the corresponding samples in the magnetic stirring study (cf. Figure 3 and 6). Again, unstirred protein samples and stirred PBS did not show any significant increase in nanometer- and micron sized particle counts, and no IgG monomer loss was found in unstirred IgG solution. In the contact stirred IgG solution containing 0.01% polysorbate 20 the generation of micron sized particles was substantially inhibited and hardly any decrease in monomer concentration was seen, whereas the number of particles in the nanometer range was slightly increased.

When the IgG concentration in the solution was increased to 0.5 mg/mL and contact stirring was applied, the micron sized particle concentration reached almost 3.0×10^6 per mL after 270 minutes (Figure 7), with an average size of 2.98 μm . The monomer content decreased with 4.9% after 270 minutes of contact stirring. Because of the high number of micron sized particles, which interfered with the NTA measurements, the concentration of nanometer sized particles could not be reliably assessed.

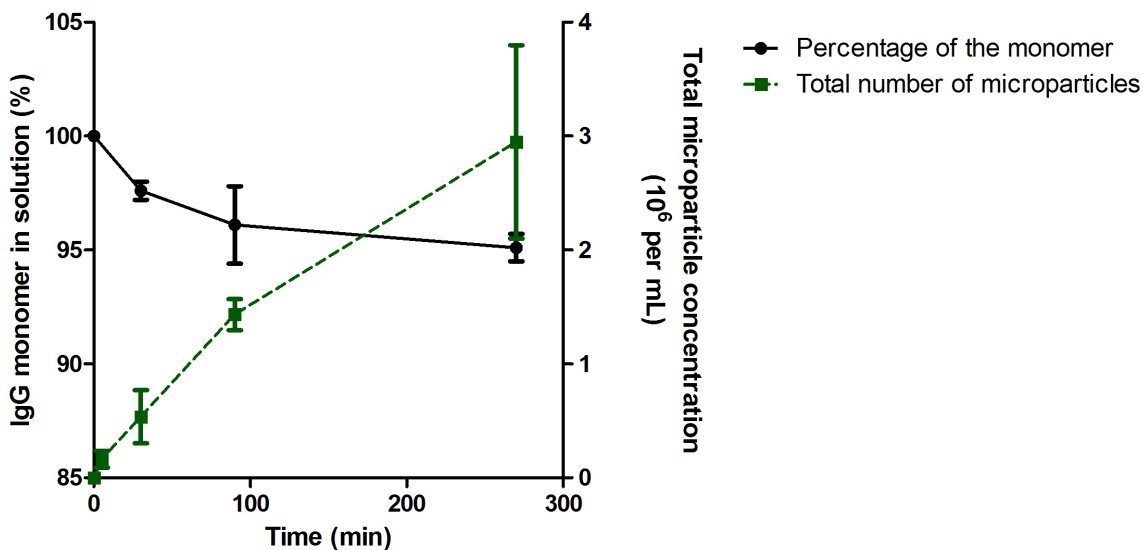


Figure 7: Contact stirring of 0.5 mg/mL IgG solution. The decrease in IgG monomer concentration is shown in black circles and is depicted on the left y-axis. The green triangles show the total number of micrometer-sized particles, with the values depicted on the right y-axis. All the graphs show the average and standard deviation of triplicate experiments.

Effect of contact area and normal pressure of the contact sliding on micron sized particle formation

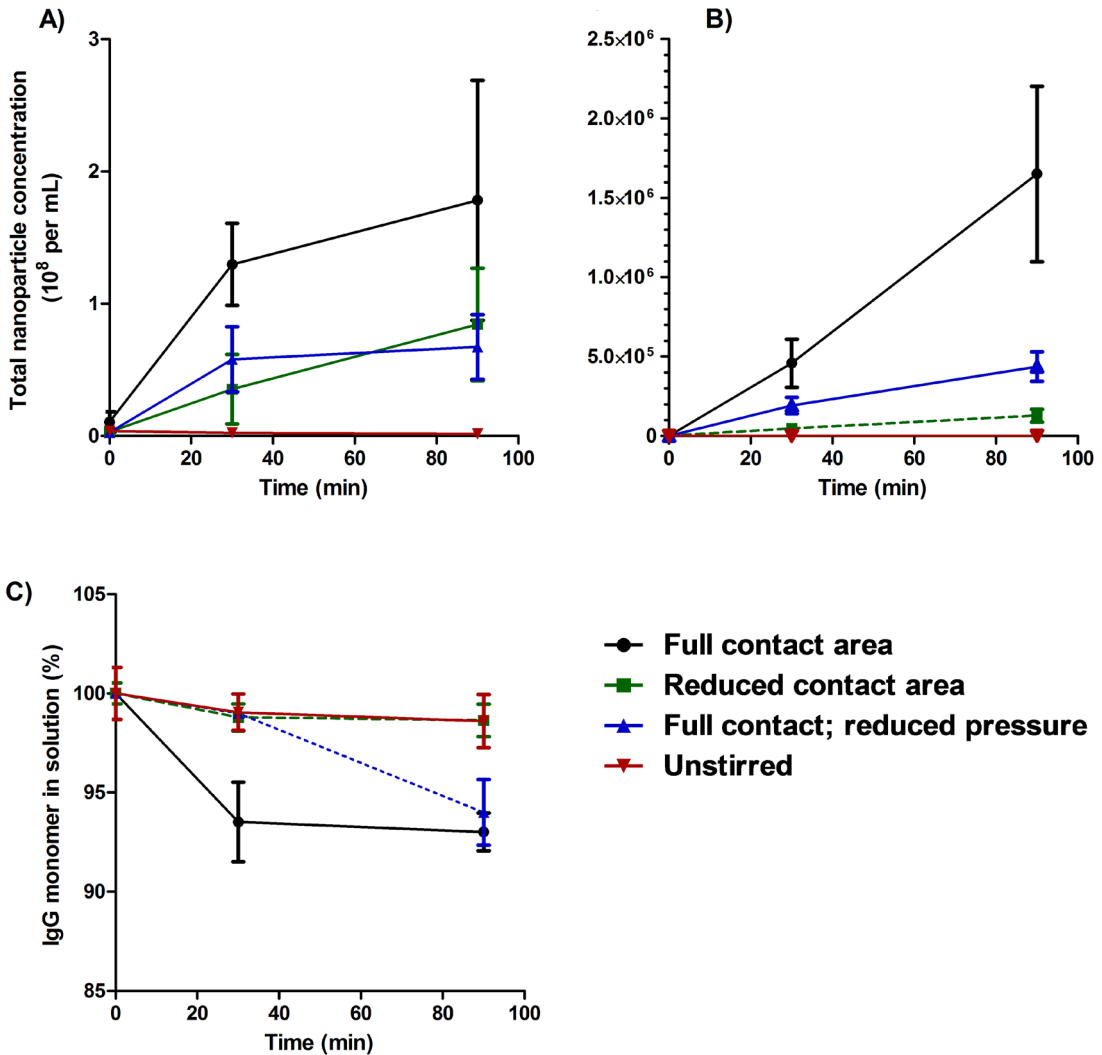


Figure 8: Effect of contact area and normal pressure on stirring-induced protein aggregation. Aggregation was monitored as function of time for IgG solution stirred with the full contact area, IgG solution stirred with reduced contact area, IgG solution stirred with reduced pressure, and unstirred IgG solution. Plots show the total concentration of A) nanometer sized particles as measured by NTA and B) micron sized particles as measured by MFI; and C) percentages of monomeric IgG still in solution as measured by SEC. All the graphs show the average and standard deviation of triplicate experiments.

In the first part of this stirring experiment, the effect of the contact area between the stir bar and the bottom of the container on the magnitude of aggregation was investigated. As shown by the number of nanometer- and micron sized particles per mL (Figure 8A and

B), stirring for 90 min with a reduced contact area generated fewer particles compared to full contact area (4.4×10^5 vs. 1.7×10^6 micron sized particles per mL, respectively). The monomer content was significantly decreased only in the stirring set-up with full contact sliding area (Figure 8C).

The second part of this experiment concerned the effect of normal pressure. The concentration of both nanometer- and micron sized particles after stirring for 90 min with reduced normal pressure (1.96 N) was less than that upon stirring with full pressure (5.88 N), while monomer losses in SEC of 6% (reduced pressure) and 7% (full pressure) were comparable ($p = 0.42$, Student's t-test).

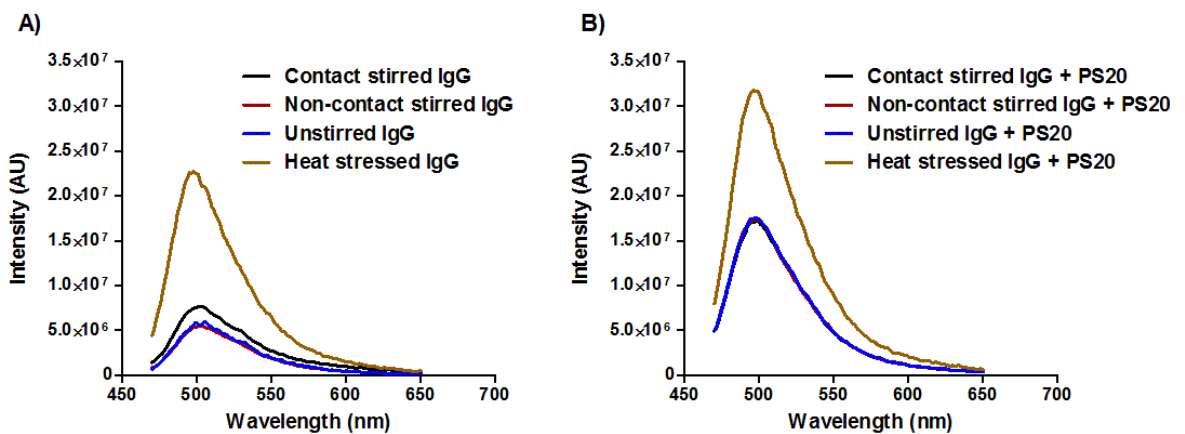


Figure 9: Steady-state fluorescence spectra of DCVJ spiked into IgG solution stirred with contact sliding of the bar over the glass surface (black), IgG solution without contacting the glass (red), unstirred IgG solution (blue), and heat stressed IgG (brown) in A) absence and B) presence of 0.01% polysorbate 20.

The secondary and tertiary structure of IgG in untreated, contact sliding, and non-contact stirred IgG solutions was studied by using far-UV CD and intrinsic fluorescence spectroscopy, respectively. These experiments did not reveal any alteration in secondary and tertiary conformation under any of the stirring conditions (data not shown). In contrast, extrinsic fluorescence measurements with DCVJ showed a slight increase in fluorescence intensity in the spectrum of the contact stirred polysorbate-free IgG solution as compared to unstirred and non-contact stirred IgG solutions (Figure 9A), although less than for the heat stressed control. Interestingly, the polysorbate-containing IgG formulation exposed to contact stirring showed a similar spectral intensity as the unstirred and non-contact stirred control samples (Figure 9B), indicating that polysorbate indirectly inhibited the induction of conformational changes during contact stirring.

Stirring of other protein solutions

The stirring experiments with and without contact sliding together with the unstirred control experiment were also performed with another monoclonal IgG antibody, BSA and myoglobin. As shown in Table 1, contact stirring of all the three protein solutions led to significant increases in the numbers of both nanometer- and micron sized particles, whereas this was not the case for the corresponding unstirred and non-contact stirred protein solutions. However, according to SEC analysis only IgG-BI solution showed a significant monomer content decrease after 270 minutes of contact stirring, while in none of the samples oligomers were detected (results not shown).

Table 1: Summary of the effect of non-contact stirring and contact stirring on aggregation of 3 other proteins.

	Unstirred			270 minutes non-contact stirring			270 minutes contact stirring		
	IgG-BI	BSA	Myo	IgG-BI	BSA	Myo	IgG-BI	BSA	Myo
Percentage of monomer (\pm SD)	100.0 \pm 0.2	100.0 \pm 0.2	100.0 \pm 1.7	98.8 \pm 1.3	99.1 \pm 2.2	98.4 \pm 1.8	93.8 \pm 2.4 *	97.2 \pm 3.3	98.9 \pm 0.6
Total number of nanoparticles ($10^8/\text{mL} \pm$ SD)	0.07 \pm 0.04	0.14 \pm 0.04	0.02 \pm 0.00	0.03 \pm 0.02	0.19 \pm 0.03	0.30 \pm 0.05	1.37 \pm 0.34 *	1.40 \pm 0.15 *	1.29 \pm 0.11 *
Total number of microparticles ($10^3/\text{mL} \pm$ SD)	0.20 \pm 0.01	16.21 \pm 1.18	0.0786 \pm 0.0132	2.53 \pm 0.30	11.28 \pm 0.08	2.51 \pm 1.91	957.21 \pm 184.74 *	78.64 \pm 13.21 *	168.41 \pm 33.42 *

* Significant increase/decrease compared to unstirred and non-contact stirred sample ($P < 0.05$)

Discussion

Stirring stress is commonly applied in forced degradation studies of protein pharmaceuticals³⁰. This study is the first one comparing contact stirring versus non-contact stirring with respect to induction of protein aggregation. The overall results clearly show that contact sliding of the stir bar over the surface of the container plays a key role in stirring-induced protein aggregation and indicate that shear alone does not induce aggregation, in line with a study by Bee et al.²². Corroborating previous studies on stirring-induced aggregation^{15,31-33}, magnetic stirring led to a significant increase in the number of nanometer- and micron sized particles. The imaged particles by MFI indicated that a large quantity of the particles were a few micrometers in size. No increase in number of micron sized particles was observed when only the buffer solution was magnetically stirred, indicating that particles formed in magnetically stirred IgG solution were proteinaceous. This increase in number of particles was accompanied with a clear decrease in the protein monomer content in absence of oligomers, suggesting a severe and rapid particle formation due to stirring. A five-fold

higher IgG concentration resulted in not only larger numbers and sizes of micron sized particles, but also appearance of visible particles. These events were accompanied by a faster relative monomer content decrease compared to the experiments done at an IgG concentration of 0.1 mg/mL. The underlying reason for this faster decrease in monomer content could be two-fold: a) the more abundant the monomer in solution becomes, the faster the solid surface gets covered with protein and b) the presence of a higher protein concentration would facilitate any potential aggregation via monomer addition.

Based on the method described by Barnard and co-workers³⁴, where it is assumed that particles are spherical and consist of 75% protein and 25% water, after 90 min of stirring the amount of protein in the nanometer- and micron sized particle fractions was calculated to be less than 0.01% and about 1.6%, respectively, of the total protein mass. This is less than what would be expected, considering the monomer loss observed in SEC (ca. 5%). In contrast, when using the overhead system in the contact mode the amount of protein in the particles generated in the contact stirred IgG solution (stirring time 270 min) was estimated to be about 19.4% of total protein, whereas the monomer loss in SEC was about 10%, i.e., in this case the apparent total recovery was above 100%.

These discrepancies may be explained by the inaccuracy of the assumptions (spherical shape and 75% protein content in a particle) made in this method. Kalonia et al. proposed a refinement of particle volume calculation based on the morphological parameters (aspect ratio and circularity) of the particles provided by the MFI³⁵. Even so, when a majority of the micron sized particles is smaller than 5 μm , the resolution of the images is not sufficient to reliably derive the morphological parameters. From an analytical point of view a few other arguments can contribute to the error as well. One of those is the inability of both NTA and MFI to accurately size heterogeneous protein particles with a size around 1 μm , i.e., at about the upper and lower size limit, respectively, of the instrument. In addition, all the methods used in this study are based on different analytical principles, which could lead to some level of inconsistency between orthogonal techniques³⁶.

In order to study the effects of the contact between the stir bar and the container, an overhead system that allows stirring in both contact and non-contact modes was used. Stirring without a contact between the stir bar and the glass container did not lead to the formation of large amounts of aggregates. In contrast, stirring in contact mode led to the formation of millions of micron sized particles along with substantial loss of IgG monomer in solution, similar to the observations in magnetic stirring. A DCVJ fluorescence assay, which probes the microenvironment of protein molecules^{28,37}, indicated some conformational changes in the protein sample that was contact-stirred. Intrinsic fluorescence and CD were not sensitive enough to pick up this change in protein conformation. Likely, only a small fraction of the total protein amount are structurally altered, which can be sensitively picked

up by the fluorescent dye assay but not by the other spectroscopic methods which mainly probe the bulk of unaffected, native monomeric protein.

Based on the collective data, we suggest the following model for the mechanism of aggregation induced by magnetic stirring of protein solutions, as summarized in Figure 10. After attachment to a solid surface, proteins often undergo conformational changes^{38,39}. An adsorbed protein molecule with a perturbed state can facilitate adsorption of more protein molecules, leading to aggregation on the surface. Contact sliding of the bar abrades the formed protein layer (consisting of perturbed monomers and/or aggregates) off the surface, releasing the perturbed protein or protein aggregate into the bulk, which may be followed by further aggregation in solution, eventually leading to the formation of nanometer- and micron sized aggregates. Subsequent to the removal of the adsorbed protein layer, the cycle of protein adsorption starts again and abrasion of the new layer is repeated by sliding of the bar on the glass surface. This also explains why (contact) stirring stress in general is harsher than shaking stress^{15,33}.

In line with the proposed aggregation mechanism, the addition of polysorbate 20 had a clear inhibitory effect on IgG aggregation and conformational changes in contact-stirred samples. Several studies have indicated that the major mechanism of polysorbates in stabilizing protein involves the preferential adsorption of the surfactant at the interfaces^{40,41}. In our system, the presence of polysorbate 20 in the IgG formulation is expected to greatly reduce the adsorption of the protein to the stir bar and the container surface, and therewith hampers the process of stirring-induced structural changes in the protein and subsequent aggregation. It has to be realized, however, that the presence of polysorbate 20 did not totally avoid the formation of nanometer sized particles during contact stirring (Figure 3A and 6A), whereas the polysorbate-containing IgG solution that was non-contact stirred showed no increase in nanometer sized particles at all. This might indicate that in the contact stirred polysorbate-containing solution aggregation may be happening but is greatly delayed. So, avoiding contact sliding during stirring and adding a surfactant will have a synergetic benefit in reduction of stirring-induced protein aggregation.

It should be noted that adsorption of proteins is a known phenomenon for most engineering materials, unless there are measures taken to prevent or reduce the adsorption. In a small experiment with a Coomassie blue staining procedure we showed that IgG indeed adsorbed to solid surfaces of glass and stir bar used in this study; we also observed that the adsorption was inhibited to a great extent when polysorbate 20 was present (see *Supporting Information* for details). In addition, we have studied the stirring induced protein aggregation also with a stirring system using a glass stir bar. These conditions led to formation of particles and loss of monomer as well. However, the glass bar had a different shape and size compared to the others used in this study and therefore the results were not included.

The stronger beneficial effect of polysorbate 20, compared to avoidance of surface contact, can be explained by the fact that surfactants reduce the disposition of protein at the air-water interface too. Stirring, either with or without contact sliding of the stir bar, induces continuous refreshment of the air-water interface⁴². Just as the solid-liquid interface, the air-water interface is a source of adsorption, structural changes and subsequent aggregation of the protein adsorbed to this interface, as has been observed in shaking stress studies^{15,42,43}. At this stage, it is worth noting that the friction of the two solid surfaces can create a local temperature increase and therefore the effect of this parameter on the protein aggregation cannot be ruled out. However, our data shows that contact stirring of polysorbate 20 containing IgG solutions did not cause (considerable) protein aggregation, while the local heat creation would occur under these conditions as well.

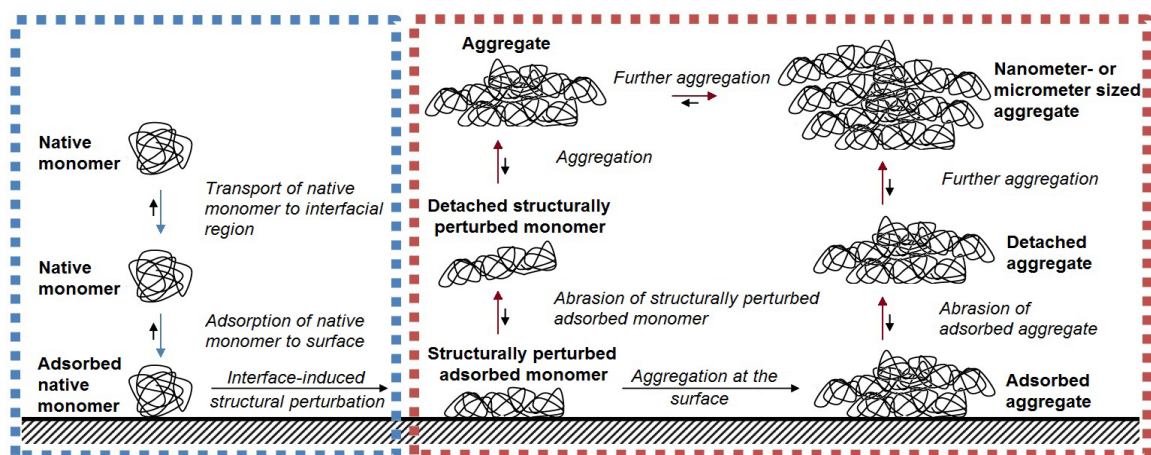


Figure 10: Schematic representation of the suggested mechanism of stirring-induced protein aggregation. The left part (framed in blue) depicts the process of protein adsorption onto solid surfaces with potential perturbation of the native structure of the protein upon adsorption. This process is followed by aggregation at the surface and in the bulk (framed in red). Contact sliding results in abrasion of the adsorbed protein layer, leading to renewal of the surface for adsorption of a fresh protein layer. Addition of surfactants, such as polysorbate 20, and avoidance of contact stirring will inhibit the steps shown as blue and red arrows, respectively.

In order to further validate the model proposed in Figure 10, effects of the pressure between the stir bar and the container and contact area of the two solid surfaces on protein aggregation were studied. The extent of aggregation was shown to be influenced by adjusting the contacting area or reducing the pressure applied by the stir bar on the glass surface. Compared to stirring with normal pressure, the number of micron sized particles was less when the pressure between the stir bar and the bottom of the container was

reduced, but with equal extent of monomer loss. Even less micron sized particles were found when the contact area was reduced, with no monomer loss over the studied time range. Reduction in normal pressure will directly affect the shear force applied on the glass surface. This in turn reduces the effective detachment of perturbed protein (layer) in the bulk solution. Another plausible explanation holds its origin in the flatness of the interacting surfaces. A smooth surface will still have 'hills' and 'valleys', even if lots of efforts have been made to get it as flat as possible. Together with plastic or elastic properties of a certain surface (e.g., a stirring bar or a container surface), the pressure can have a significant effect on the effective contact area ⁴⁴, the poor control of which in general may have a negative impact on the reproducibility of stirring-stress studies.

In our study we have shown that the phenomenon of contact sliding-induced protein aggregation holds true for another different antibody and two other model proteins as well. Although not all of the tested proteins showed a significant loss of monomer content, still a considerable increase in particle concentration was observed for each of them, suggesting that the phenomenon observed is broadly applicable to proteins in general.

Prevention of protein aggregation from mechanical stress can be best achieved by adding surfactants and avoiding contact sliding of a stirring element and the inner surfaces of the container. The potential effects of contact sliding and abrasion are applicable to several systems other than stirring. For instance, Peters et al. showed that an increase in the aspiration and dispensing frequency during compounding of highly concentrated therapeutic protein solutions leads to enhanced protein aggregation⁴⁵. In a different study, Colombié et al. ⁴⁶ showed that stirring-induced aggregation leads to irreversible inactivation of lysozyme. This may have been caused by aggregation, which was unfortunately not addressed in this particular report. The same group investigated the effect of the glass-liquid interface size on lysozyme activity by introducing glass (micro)spheres before turbine-assisted stirring was started ³¹. The effect of sliding of the particles over each other and over the surface of the container may have played a significant role in the reduced lysozyme activity observed. In a more recent study of Mehta and coworkers ⁴⁷ showed that repeated rupture of a layer of silicone oil overlaid on the surface of aqueous solutions of monoclonal antibody resulted in the formation of nanometer- and micron sized particles and substantial losses of monomer. This stress method is from a mechanistic point of view very similar to the one investigated in our work, and the two studies indicate that release or abrasion of (perturbed) monomers and/or aggregates adsorbed at either oil-water or solid-water interface leads to formation of proteinaceous particles in the bulk. Therefore, it is of great importance that the role of contact sliding between the solid surfaces in protein aggregation is recognized and taken into account when designing manufacture, formulation, and handling protocols for therapeutic proteins, as well as when setting up stirring stress studies.

Conclusion

Mechanical stress is one of the reasons that proteins aggregate during different stages of manufacturing and practical use in clinical settings. The data presented herein indicate that for stirring stress, contact sliding of the stir bar over the surface of the container plays a critical role in induction of protein aggregation. Our data suggests that abrasion of proteins adsorbed on solid surfaces leads to progressive protein particle formation in bulk solution, which can be best inhibited by avoiding contact of the stirring device with the container surface and adding a surfactant.

References

1. Mitragotri S, Burke PA, Langer R. 2014. Overcoming the challenges in administering biopharmaceuticals: formulation and delivery strategies. *Nat Rev Drug Discov* 13(9):655-672.
2. Eichler HG, Aronsson B, Abadie E, Salmonson T. 2010. New drug approval success rate in Europe in 2009. *Nat Rev Drug Discov* 9(5):355-356.
3. Crunkhorn S. 2013. Enhanced chance of success for protein replacement therapies. *Nat Rev Drug Discov* 12(6):414-414.
4. Dimitrov DS. 2012. Therapeutic proteins. *Method Mol Biol* 899:1-26.
5. Bhutani D, Vaishampayan UN. 2013. Monoclonal antibodies in oncology therapeutics: present and future indications. *Expert Opin Biol Th* 13(2):269-282.
6. Kotsovilis S, Andreakos E. 2014. Therapeutic human monoclonal antibodies in inflammatory diseases. *Method Mol Biol* 1060:37-59.
7. Torosantucci R, Schoneich C, Jiskoot W. 2014. Oxidation of therapeutic proteins and peptides: structural and biological consequences. *Pharm Res* 31(3):541-553.
8. Ratanji KD, Derrick JP, Dearman RJ, Kimber I. 2014. Immunogenicity of therapeutic proteins: influence of aggregation. *J Immunotox* 11(2):99-109.
9. Chirmule N, Jawa V, Meibohm B. 2012. Immunogenicity to Therapeutic Proteins: Impact on PK/PD and Efficacy. *AAPS J* 14(2):296-302.
10. Medicine EDFTQO 2010. Ph.Eur. 2.9.19, Pharmacopoeia Europaea, 7th ed., Particulate contamination: Sub-visible particles.
11. USP. 2012. USP/NF General Chapter <1046> Cellular and Tissue-Based Products. In Convention USP, editor, Rockville, MO.
12. USP. 2014. USP/NF General Chapter <787> Subvisible Particulate Matter in Therapeutic Protein Injections. In Convention USP, editor, Rockville, MO.
13. Wang W, Li N, Speaker S. 2010. External Factors Affecting Protein Aggregation. In Wang W, Roberts CJ, editors. *Aggregation of therapeutic proteins*, ed.: John Wiley & Sons, Inc. p 86.
14. Mahler HC, Friess W, Grauschopf U, Kiese S. 2009. Protein aggregation: pathways, induction factors and analysis. *J Pharm Sci* 98(9):2909-2934.

15. Kiese S, Pappenberg A, Friess W, Mahler HC. 2008. Shaken, not stirred: mechanical stress testing of an IgG1 antibody. *J Pharm Sci* 97(10):4347-4366.
16. Lim JY, Kim NA, Lim DG, Kim KH, Jeong SH. 2014. Effects of thermal and mechanical stress on the physical stability of human growth hormone and epidermal growth factor. *Arch Pharm Res*.
17. Macchi F, Hoffmann SV, Carlsen M, Vad B, Imperato A, Rischel C, Otzen DE. 2011. Mechanical stress affects glucagon fibrillation kinetics and fibril structure. *Langmuir* 27(20):12539-12549.
18. Abbas SA, Sharma VK, Patapoff TW, Kalonia DS. 2012. Opposite effects of polyols on antibody aggregation: thermal versus mechanical stresses. *Pharm Res* 29(3):683-694.
19. Basu P, Krishnan S, Thirumangalathu R, Randolph TW, Carpenter JF. 2013. IgG1 aggregation and particle formation induced by silicone-water interfaces on siliconized borosilicate glass beads: a model for siliconized primary containers. *J Pharm Sci* 102(3):852-865.
20. Devineni D, Gonschorek C, Cicerone MT, Xu YM, Carpenter JF, Randolph TW. 2014. Storage stability of keratinocyte growth factor-2 in lyophilized formulations: Effects of formulation physical properties and protein fraction at the solid-air interface. *Eur J Pharm Biopharm* 88(2):332-341.
21. Telikepalli SN, Kumru OS, Kalonia C, Esfandiary R, Joshi SB, Middaugh CR, Volkin DB. 2014. Structural Characterization of IgG1 mAb Aggregates and Particles Generated Under Various Stress Conditions. *J Pharm Sci* 103(3):796-809.
22. Bee JS, Stevenson JL, Mehta B, Svitel J, Pollastrini J, Platz R, Freund E, Carpenter JF, Randolph TW. 2009. Response of a concentrated monoclonal antibody formulation to high shear. *Biotechnol Bioeng* 103(5):936-943.
23. Filipe V, Hawe A, Jiskoot W. 2010. Critical evaluation of Nanoparticle Tracking Analysis (NTA) by NanoSight for the measurement of nanoparticles and protein aggregates. *Pharm Res* 27(5):796-810.
24. Filipe V, Poole R, Oladunjoye O, Braeckmans K, Jiskoot W. 2012. Detection and characterization of subvisible aggregates of monoclonal IgG in serum. *Pharm Res* 29(8):2202-2212.
25. Filipe V, Kukrer B, Hawe A, Jiskoot W. 2012. Transient molten globules and metastable aggregates induced by brief exposure of a monoclonal IgG to low pH. *J Pharm Sci* 101(7):2327-2339.
26. Sediq AS, Nejadnik MR, El Bialy I, Witkamp GJ, Jiskoot W. 2015. Protein-polyelectrolyte interactions: Monitoring particle formation and growth by nanoparticle tracking analysis and flow imaging microscopy. *Eur J Pharm Biopharm* 93:339-345.
27. Lakowicz JR. 2006. Principles of fluorescence spectroscopy. 3rd ed., New York: Springer. p xxvi, 954 p.
28. Hawe A, Sutter M, Jiskoot W. 2008. Extrinsic fluorescent dyes as tools for protein characterization. *Pharm Res* 25(7):1487-1499.

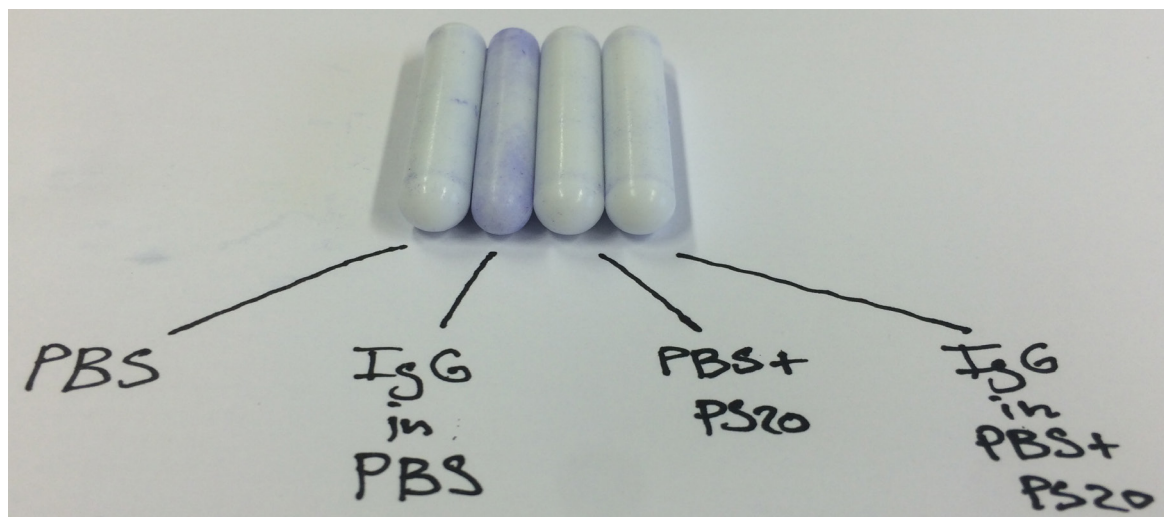
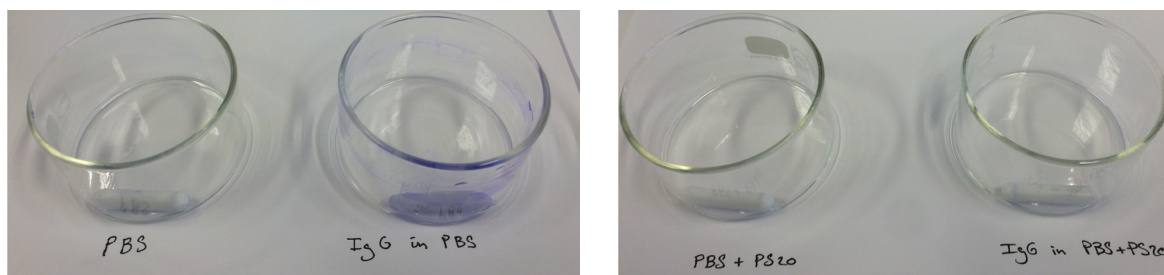
- 29.** Hawe A, Filipe V, Jiskoot W. 2010. Fluorescent Molecular Rotors as Dyes to Characterize Polysorbate-Containing IgG Formulations. *Pharm Res* 27(2):314-326.
- 30.** Hawe A, Wiggenghorn M, van de Weert M, Garbe JHO, Mahler HC, Jiskoot W. 2012. Forced degradation of therapeutic proteins. *J Pharm Sci* 101(3):895-913.
- 31.** Colombie S, Gaunand A, Lindet B. 2001. Lysozyme inactivation under mechanical stirring: effect of physical and molecular interfaces. *Enzyme Microb Tech* 28(9-10):820-826.
- 32.** Ishikawa T, Kobayashi N, Osawa C, Sawa E, Wakamatsu K. 2010. Prevention of Stirring-Induced Microparticle Formation in Monoclonal Antibody Solutions. *Biol Pharm Bull* 33(6):1043-1046.
- 33.** Mahler HC, Muller R, Friess W, Delille A, Matheus S. 2005. Induction and analysis of aggregates in a liquid IgG1-antibody formulation. *Eur J Pharma Biopharm* 59(3):407-417.
- 34.** Barnard JG, Singh S, Randolph TW, Carpenter JF. 2011. Subvisible Particle Counting Provides a Sensitive Method of Detecting and Quantifying Aggregation of Monoclonal Antibody Caused by Freeze-Thawing: Insights Into the Roles of Particles in the Protein Aggregation Pathway. *J Pharm Sci* 100(2):492-503.
- 35.** Kalonia C, Kumru OS, Prajapati I, Mathaes R, Engert J, Zhou SX, Middaugh CR, Volkin DB. 2015. Calculating the Mass of Subvisible Protein Particles with Improved Accuracy Using Microflow Imaging Data. *J Pharm Sci* 104(2):536-547.
- 36.** Filipe V, Hawe A, Carpenter JF, Jiskoot W. 2013. Analytical approaches to assess the degradation of therapeutic proteins. *Trend Anal Chem* 49:118-125.
- 37.** Kung CE, Reed JK. 1989. Fluorescent Molecular Rotors - a New Class of Probes for Tubulin Structure and Assembly. *Biochemistry-US* 28(16):6678-6686.
- 38.** Norde W, Haynes CA. 1995. Reversibility and the mechanism of protein adsorption. *ACS Symp Ser* 602:26-40.
- 39.** Nejadnik MR, Deepak FL, Garcia CD. 2011. Adsorption of Glucose Oxidase to 3-D Scaffolds of Carbon Nanotubes: Analytical Applications. *Electroanal* 23(6):1462-1469.
- 40.** Joshi O, McGuire J, Wang DQ 2008. Adsorption and Function of Recombinant Factor VIII at Solid-Water Interfaces in the Presence of Tween-80. *J Pharm Sci* 97(11):4741-4755.
- 41.** Zhang MQ, Ferrari M. 1997. Reduction of albumin adsorption onto silicon surfaces by Tween 20. *Biotechnol Bioeng* 56(6):618-625.
- 42.** Maa YF, Hsu CC. 1997. Protein denaturation by combined effect of shear and air-liquid interface. *Biotechnol Bioeng* 54(6):503-512.
- 43.** Treuheit MJ, Kosky AA, Brems DN. 2002. Inverse relationship of protein concentration and aggregation. *Pharm Res* 19(4):511-516.
- 44.** Bowden FP, Tabor D. 1938. The area of contact between stationary and between moving surfaces. *P Roy Soc a-Math Phy* 169:22.

45. Peters BJM, Capelle MAH, Arvinte T, van de Garde EMW. 2013. Validation of an automated method for compounding monoclonal antibody patient doses Case studies of Avastin (R) (bevacizumab), Remicade (R) (infliximab) and Herceptin (R) (trastuzumab). *Mabs-Austin* 5(1):162-170.

46. Colombie S, Gaunand A, Rinaudo M, Lindet B. 2000. Irreversible lysozyme inactivation and aggregation induced by stirring: kinetic study and aggregates characterisation. *Biotechnol Lett* 22(4):277-283.

47. Mehta SB, Lewus R, Bee JS, Randolph TW, Carpenter JF. 2015. Gelation of a monoclonal antibody at the silicone oil-water interface and subsequent rupture of the interfacial gel results in aggregation and particle formation. *J Pharm Sci* 104(4):1282-1290.

Supporting information



Visual appearance of the containers and stir bar after stirring and staining procedure. In brief, 80 mL PBS or protein solution was stirred at 300 rpm for 30 min. The solutions were discarded, and container and stir bar were rinsed thoroughly with PBS. Subsequently, 80 mL 0.2% (w/w) Coomassie blue R-250 in 10% acetic acid was added and the samples were incubated for 30 min. The dye solution was removed, the glass and stir bar were extensively rinsed with 10% acetic acid.

Protein-polyelectrolyte interactions: monitoring particle formation and growth by nanoparticle tracking analysis and flow imaging microscopy



Ahmad S. Sediq¹, M. Reza Nejadnik¹, Inas El Bialy¹, Geert J. Witkamp², and Wim Jiskoot^{1,1}

¹ Division of Drug Delivery Technology, Leiden Academic Centre for Drug Research (LACDR), Leiden University, 2333 CC Leiden, The Netherlands

² Biotechnology Department, Delft University of Technology, 2628 CA Delft, The Netherlands

The chapter was published in the *European Journal of Pharmaceutics and Biopharmaceutics*:
Eur J Pharm Biopharm 2015 93: 339-345

Abstract

The purpose of this study was to investigate the formation and growth kinetics of complexes between proteins and oppositely charged polyelectrolytes. Equal volumes of IgG and dextran sulfate (DS) solutions, 0.01 mg/ml each in 10 mM phosphate, pH 6.2, were mixed. At different time points, samples were taken and analyzed by nanoparticle tracking analysis (NTA), Micro-Flow Imaging (MFI) and size-exclusion chromatography (SEC). SEC showed a huge drop in monomer content (approximately 85%) already 2 minutes after mixing, while a very high nanoparticle (size up to 500 nm) concentration (ca. 9×10^8 /mL) was detected by NTA. The nanoparticle concentration gradually decreased over time, while the average particle size increased. After a lag time of about 1.5 h, a steady increase in microparticles was measured by MFI. The microparticle concentration kept increasing up to about 1.5×10^6 /mL until it started to slightly decrease after 10 h. The average size of the microparticles remained in the low- μm range (1-2 μm) with a slight increase and broadening of the size distribution in time. The experimental data could be fitted with Smoluchowski's perikinetic coagulation model, which was validated by studying particle growth kinetics in IgG:DS mixtures of different concentrations. In conclusion, the combination of NTA and MFI provided novel insight into the kinetics and mechanism of protein-polyelectrolyte complex formation.

Introduction

The interaction between proteins and polyelectrolytes has been receiving increasing attention in pharmaceutical sciences because of the growing importance of protein drugs¹. The latter is mainly related to their specificity and the lack of toxic metabolites, resulting in considerably less interference with untargeted biological processes and, hence, less adverse effects and increased clinical efficiency². Successfully developing protein drugs, however, requires the availability of highly pure protein batches as well as suitable formulations that guarantee the physical and chemical stability of the protein³⁻⁵ until its delivery at the target site.

Polyelectrolytes are a major group of the macromolecules that have shown to offer advantages in purification^{6,7}, stabilization⁸ and delivery of therapeutic proteins^{9,10}. Polyelectrolytes are suitable as component of protein delivery systems because they can be selected with specific hydrophilicity, versatile charge properties, biodegradability, natural origin, and roles in preventing aggregation and denaturation of proteins¹¹⁻¹⁴. Moreover, polyelectrolytes have been used to increase the amount of protein loaded onto the surface of solid microneedles and microparticles via layer-by-layer deposition of oppositely charged proteins and polyelectrolytes^{15,16}. Furthermore, polyelectrolyte-mediated precipitation methods have been used in protein purification processes¹⁷ to decrease the number of isolation steps at a low cost. This approach is considered to be more selective than the use of other precipitants, such as ammonium sulfate or organic solvents¹⁸. In addition, another advantage of polyelectrolyte-assisted precipitation along with protein co-precipitation techniques¹⁹ is that these methods do not require organic solvents that could be harmful to the protein as well as the environment. The molecular interaction involves electrostatic interactions between charged surfaces of the protein and oppositely charged groups of the polyelectrolyte²⁰. The onset of complexation depends on several parameters, such as pH, ionic strength, protein/polyelectrolyte ratio and physico-chemical characteristics of the protein and the polyelectrolyte (e.g., charge, size)^{21,22}. These interactions create insoluble complexes, which then aggregate further to form larger particles that will eventually precipitate from the solution²³. The process of particle growth depends not only on the nature of the particles, but also on external factors, such as temperature, stirring and sedimentation²⁴.

A great challenge in the direct assessment of protein-polyelectrolyte interactions has been the lack of techniques that are able to simultaneously detect, characterize and quantify (sub)visible particles that form upon complexation of protein and polyelectrolyte. Emerging particle analysis techniques^{25,26}, however, may provide reliable ways to monitor protein-polyelectrolyte complex formation and growth. In the nanometer range, nanoparticle tracking analysis (NTA) is a valuable technique that counts and sizes particles in a suspension. In

the flow-cell of NTA, the particles scatter a beam of laser light, which is detected through a microscope and recorded into a video exhibiting the movement of particles in the suspension. The displacement of individual particles, or the Brownian motion, in a plane is tracked in time to deduce the individual particle size²⁷⁻³⁰. In the micrometer size range, flow imaging microscopy techniques, such as, Micro-Flow Imaging (MFI), are currently gaining ground as established methods for micron-size particle sizing and counting³¹⁻³⁴. The principle of detection is based on the change in the light intensity passing through a particle compared to the background. Based on the captured images the particle size and count are derived. The same images can be used to assess several morphological aspects of individual particles, like aspect ratio and transparency. The aim of this study was to develop a method based on the combination of NTA and MFI to monitor and characterize the process of particle formation and growth during protein-polyelectrolyte complexation, assisted by size-exclusion chromatography (SEC) to quantify the amount of unbound protein monomer. A monoclonal antibody was used as a model protein and dextran sulfate as a model polyelectrolyte. The experimental data for a few different experimental conditions were fitted with Smoluchowski's perikinetic coagulation model^{35,36}.

Materials and Methods

Materials

Dextran sulfate (from *Leuconostoc* spp., Mw = 5000), sodium phosphate dibasic dihydrate, sodium phosphate monobasic dihydrate, sodium azide and sodium sulfate (pKa < 2) were obtained from Sigma (Sigma-Aldrich, Steinheim, Germany). Ultrapure water (18.2 MΩ.cm) was dispensed by using a Purelab Ultra water purification system (ELGA LabWater, Marlow, UK). A monoclonal human IgG1 subclass (IgG; pI = 8.4), formulated at 65 mg/ml in 10 mM sodium citrate buffer containing 5% sucrose at pH 6.0, described before^{29,37,38}, was used as a model protein. Stock solutions of 0.01 mg/ml of IgG in aqueous solution of 10 mM phosphate buffer, pH 6.2 (filtered by using a 0.22-μm polyethersulfone-based syringe driven filter unit (Millex GP, Millipore, Ireland)), was prepared. The same buffer was used to prepare stock solutions of 0.01 mg/ml dextran sulfate. In preliminary studies we found that a low buffer concentration and a pH value lower than 7 are beneficial for the formation of IgG-dextran sulfate complexes. Addition of the protein or polyelectrolyte had no effect on the pH of 6.2.

Mixing, incubation and sampling procedure

A volume of 13 mL of the IgG stock solution was poured into a graduated glass cylinder (Duran®, Hirschmann, Eberstadt, Germany), with an inner diameter of 1.4 cm and a height of 14.9 cm. 13 mL of the dextran sulfate stock solution was added to the IgG solution.

Subsequently, the IgG/dextran sulfate mixture was homogenized by gentle pipetting up and down 15 times, and then incubated for a period of 14 hours. In order to avoid unwanted movements and temperature fluctuations (as these might affect the kinetics of the particle growth), the glass container was kept on a sturdy bench where the analytical instruments were located. The first sample was taken immediately after mixing. The sampling was continued for 840 min after preparation according to the scheme shown in Figure 1.

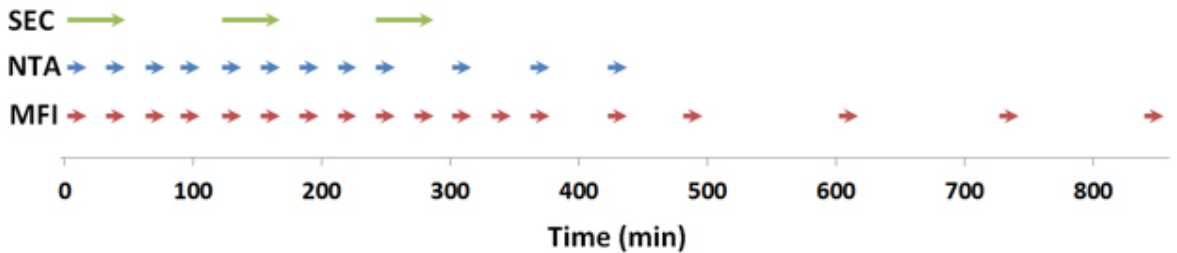


Figure 1: Schematic overview of the sampling time points for each type of measurement performed in this study. The length of each rod indicates the approximate analysis time per sample, including sample pretreatment and handling.

Samples were directly used for the different analyses, unless otherwise stated. The experiment was performed twice. During the experiment the room temperature in the lab was monitored (23 ± 0.8 °C). In order to prepare samples for quantification of the free protein monomer content, 1 mL of the sample was centrifuged in a 1.5 mL Eppendorf tube at $18,000 \times g$ for 15 minutes. A hundred μL from the top part of the liquid was taken and immediately used for measurement of the monomer content by using SEC. The supernatant was analyzed by NTA to confirm that it was free of particles (results not shown).

In order to check the applicability of the method to other formulations and to validate whether Smoluchowski's perikinetic coagulation model (see below) describes the particle formation process, additional mixing experiments were performed with two different concentrations of IgG and dextran sulfate in the starting materials, namely 0.005 and 0.02 mg/mL (instead of 0.01 mg/mL). The experimental procedure was kept the same, except that the particle formation process was monitored for only 270 min.

Size-exclusion chromatography

High pressure size-exclusion chromatography (SEC) was performed to quantify the amount of free IgG monomer in the solution in absence and presence of dextran sulfate. This was executed on an Agilent 1200 chromatography system (Agilent Technologies, Palo Alto, California) combined with a Wyatt Eclipse (Wyatt Technology Europe GmbH, Dernbach, Germany). A Yarra 3 μm SEC-2000 column (300×7.8 mm) coupled with a Yarra Security Guard precolumn (Phenomenex, Torrance, CA, USA) was used. Centrifuged

(18,000 x g for 15 minutes) samples (100 μ L) were injected and separation was performed at a flow rate of 0.5 mL/min. The mobile phase consisted of 100 mM sodium phosphate, 100 mM sodium sulfate, and 0.05 % w/v sodium azide at pH 7.2. Ultraviolet absorption detection was performed at 280 nm. In order to calculate the monomer decrease after complexation, the areas under the curve (AUC) of the UV signal were used.

Nanoparticle tracking analysis

NTA was performed at room temperature ($23 \pm 0.5^\circ\text{C}$) with a NanoSight LM20 (NanoSight Ltd., Amesbury, United Kingdom) equipped with a 640 nm laser and operating at an angle of 173° with respect to the flow cell (100 x 80 x 10 μm). Samples were taken from the mixture vessel by using a sterile 1 mL syringe (BD Discardit II, New Jersey). The contents of the syringe were injected into the chamber by an automatic pump (Harvard apparatus, Catalog no 98-4362). For each sample a 90 s video was captured with shutter set at 1495 and gain at 400. The video was analyzed by using the NTA 2.0 Build 127 software. The following settings were used for tracking of the particles: background extract on; brightness 0; gain 1.00; blur size 3x3; detection threshold 10, viscosity equal to that of water. All other parameters were set to the automatic adjustment mode.

Flow imaging microscopy

A Micro-Flow Imaging (MFI) system (MFI5200, ProteinSimple, Santa Clara, USA), equipped with a silane coated flow cell (1.41 x 1.76 x 0.1 mm) and controlled by the MFI View System Software (MVSS) version 2, was used for flow imaging microscopy analysis. The system was flushed with 4 mL purified water at 6 mL/min prior to each measurement. The flow cell cleanliness was checked visually between measurements. The background was zeroed by flowing 10 mM phosphate buffer, pH 6.2, and performing the 'optimize illumination' procedure. Samples of 0.5 mL with a pre-run volume of 0.2 mL were analyzed at a flow rate of 0.17 mL/min and a fixed camera rate of 22 flashes per second.

The data recorded by the MVSS was analyzed with MFI View Analysis Suite (MVAS) version 1.2. For each sample, stuck, edge and slow moving particles were removed by the software before data analysis. The equivalent circular diameter (ECD), which is the diameter of a circle that has an area equal to that of the particle imaged by MFI, was calculated and presented as a measure of the particle size.

Theoretical calculations

Fitting the experimental data with Smoluchowski's perikinetic coagulation model

The experimental data were plotted such that they illustrate the changes in total particle concentration over time, as particle collision leads to fusion into larger particles. These

changes were fitted by a one-phase exponential decay equation:

$$N(t) = N_0 e^{-\frac{\ln 2}{\tau_{exp}} t} \quad \text{Eq. 1}$$

from which N_0 (the initial total particle concentration) and τ_{exp} (the experimental half-life, i.e., the time at which the total concentration of particles reduces to half) were obtained. Knowing the initial total number of particles N_0 , Smoluchowski's perikinetic coagulation theory was used to predict a theoretical half-life (τ_{theor}) by assuming that all particle collisions lead to fusion:

$$\tau_{theor} = \frac{3\mu}{4K_B T N_0^2} \quad \text{Eq. 2}$$

where μ is the viscosity of the buffer, K_B the Boltzmann constant and T the absolute temperature. The sticking probability (α), defined as the fraction of particles remaining in contact after collision²⁴, was calculated from the ratio between τ_{theor} and τ_{exp} :

$$\alpha = \frac{\tau_{theor}}{\tau_{exp}} = \frac{3\mu}{\tau_{exp} 4K_B T N_0^2} \quad \text{Eq. 3}$$

Equation 1 was used to fit the experimental data for measurements with different starting concentrations (using GraphPad Prism version 5). Subsequently, the collision efficiency for each condition was calculated and compared.

Results

In order to monitor the particle formation and growth we performed simultaneous NTA and MFI measurements at different time points after mixing equal volumes of IgG and dextran sulfate solutions, yielding a final concentration of 0.05 mg/ml IgG and 0.05 mg/ml dextran sulfate. The amount of free IgG was measured by SEC after spinning down the formed particles.

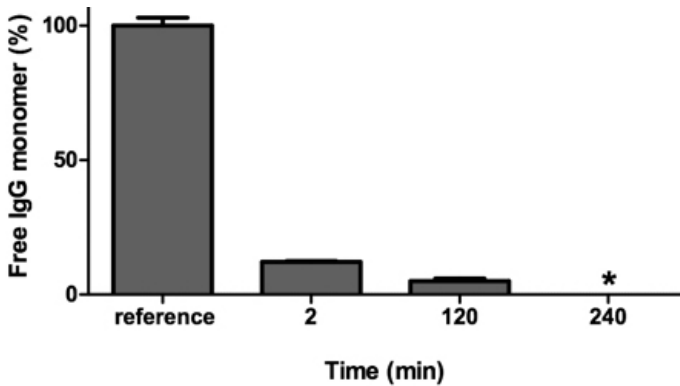


Figure 2: SEC results of centrifuged IgG/dextran sulfate (1:1 w/w, total concentration 0.01 mg/ml) mixtures, shown as percentage of IgG left in the solution at different incubation time points. The reference bar is 0.01 mg/ml IgG solution diluted twofold with 10 mM phosphate

buffer, pH 6.2. The measurement at 4 hours after preparation did not show any IgG peak at all (*).

The amount of free IgG monomer in the control (IgG alone) and prepared dextran sulfate/IgG mixture taken at three specified time points (see Figure 1) as measured by SEC is shown in Figure 2. The appearance of the pellet after spinning down the mixture was a solid precipitate.

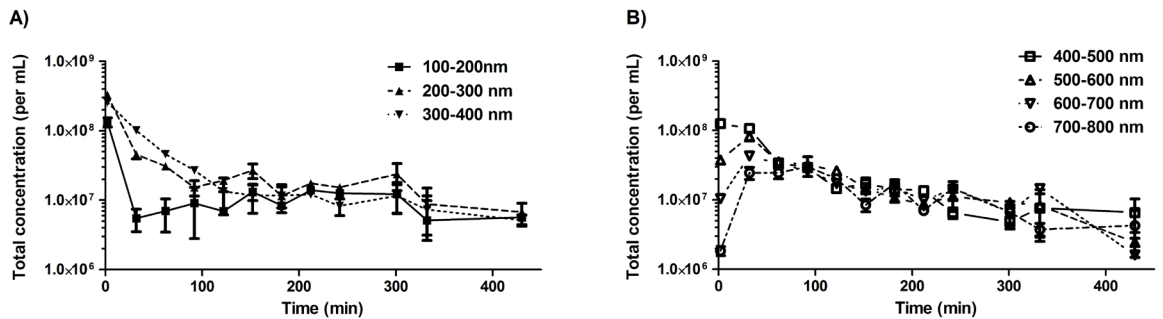


Figure 3: Results of NTA of IgG/dextran sulfate (1:1 w/w, total concentration 0.01 mg/ml) mixtures as function of incubation time. Graphs show the total particle concentrations (logarithmic scale) for each 100-nm wide size category within the size range between 100-800 nm at different time points (A: 101-400 nm; B: 401-800 nm). The size categories were split into two graphs for sake of clarity. The results of duplicate experiments are incorporated in the graphs, where each dot represents the mean and the bars the highest and lowest value. The connecting lines serve as a guidance to clarify the progress of the particle concentration of the different populations.

Compared to the reference sample, all samples showed a great decrease in free IgG monomer content, down to 12%, 5% and 0%, at 2, 120 and 240 min, respectively, after starting the incubation. Even though this SEC column showed to be suitable to separate

up to IgG tetramers, no oligomer peaks were detected by SEC for any of the samples, suggesting that the IgG monomers are rapidly included in particles that are too large to pass the SEC column and/or particles that are spun down during the centrifugation step prior to SEC analysis.

Nanoparticle tracking analysis (NTA)

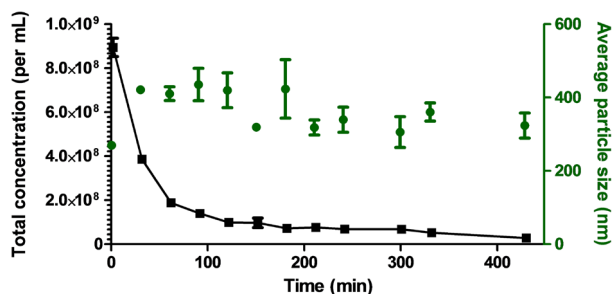


Figure 4: Total particle concentration within the 100-800 nm size range (black squares) and average particle size (green circles) of IgG/dextran sulfate (1:1 w/w, total concentration 0.01 mg/ml) mixtures, measured with NTA as function of

experiments are incorporated in the graph, where each data point represents the mean and the bars the higher and the lower value.

The generated size distribution curves obtained from NTA were sliced in segments of 100 nm bins and the total concentrations of particles within these segments at different time points were plotted. The lower detection limit of NanoSight is about 40 nm (depending on the light scattering properties of the particles), therefore the segmentation was started from 100 nm. Size bins over 800 nm were not included because no reliable data could be obtained (further explained in the Discussion section). The total concentrations of particles in the categories between 100 and 500 nm were relatively high and decreased with time already from the beginning (Figure 3A), whereas the larger size ranges showed an increase in particle concentration after the start of the experiment, which gradually stabilized and started to decrease at later time points (Figure 3B). The total nanoparticle concentration (population with a size between 100-800 nm) and the associated average particle size of this population over time are shown in Figure 4. The total particle concentration decreased exponentially with an increase in mean size in the first hour of the study timespan.

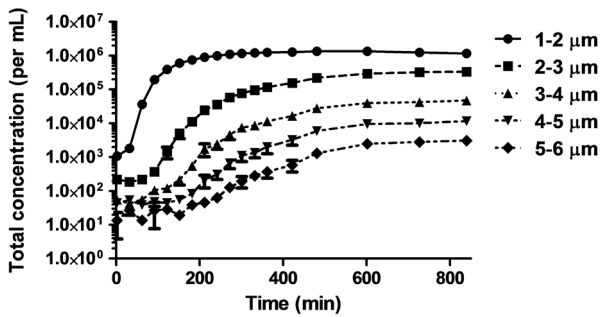


Figure 5: Results of MFI of IgG/dextran sulfate (1:1 w/w, total concentration 0.01 mg/ml) mixtures as function of incubation time. Graph shows the total particle concentrations (logarithmic scale) for each 1- μ m wide size category within the size range between 1-6 μ m at different time

points. The results of duplicate experiments are incorporated in the graph, where each dot represents the mean and the bars the highest and the lowest value.

Flow imaging microscopy was used to monitor the concentration and size distribution of particles in the micrometer-size range. Figure 5 shows the particle concentration as function of time, plotted by grouping the particles in 1- μ m wide size bins, displayed up to 6 μ m (the contribution of larger particles to the total particle count was negligible).

The particle concentration in the size range covered by the MFI instrument started to increase rapidly from about 1.5 hour after the start of the experiment. These particles were mainly in the size range between 1-2 μ m. Interestingly, when the rate of increase in the concentration of 1-2 μ m particles started to decrease, particles in the range of 2-3 μ m began to form at a fast rate; when the increase in concentration of the latter size range started to level off, 3-4 μ m sized particles started to form. Similar trends continued to happen successively for the larger particle sizes too. The total concentration of μ m-range particles increased over time and reached its maximum at about 10 h, after which it started to drop gradually, while the average size of the particles increased gradually over time after an apparent decrease within the first minutes of the experiment (Figure 6).

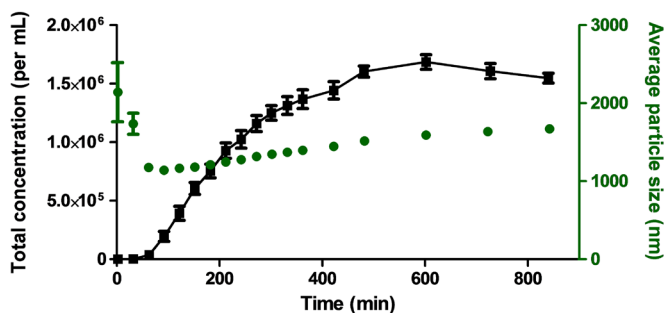


Figure 6: Total particle concentration within the 1-6 μ m size range (black squares) and average particle size (green circles) of IgG/dextran sulfate (1:1 w/w, total concentration 0.01 mg/ml) mixtures, measured with MFI as function of incubation time.

The results of duplicate experiments are incorporated in the graph, where each data point represents the mean and the bars the higher and the lower value.

NTA and flow imaging microscopy results combined

In order to visualize the overall development of particle formation and growth, as studied

by NTA and MFI, the raw data generated by each method was used to plot the distribution of particles of different sizes over time in a single graph (Figure 7).

This graph shows that a large number of nm-range particles were detected soon after the mixing of the protein and the polyelectrolyte, while no μm -range particles were detected at early time points. The particle size progressively increased with incubation time and the trend was clear toward the formation of μm -range particles within hours and a simultaneous decrease in the number of nm-range particles.

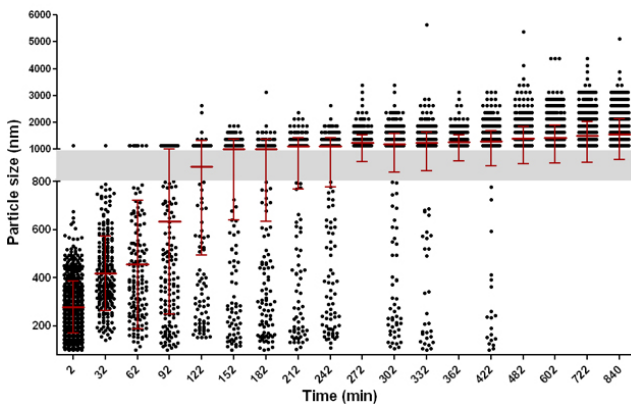


Figure 7: Graphical representation of the particle growth in IgG/dextran sulfate (1:1 w/w, total concentration

0.01 mg/ml) mixtures, as monitored by NTA and MFI (based on the data sets shown in Figures 3-6). Scatter plot shows the size of individual particles (dots) detected by NTA and MFI in a volume of 50 μL at each time point (non-linear time

axis). Particles detected by NTA measurements are shown in the lower part (100-800 nm), the ones from MFI in the upper part (1000-6000 nm). The grey bar represents the area that is not covered by both techniques. For each time point, the calculated average size and the corresponding standard deviation are indicated in red.

Fitting the experimental data into Smoluchowski's perikinetic coagulation model

The decrease in total particle concentration measured with NTA and MFI were fitted in a one-phase exponential decay formula (Eq. 1). For the concentration of 0.01 mg/ml the fitted exponential decay resulted in a N_0 value of 1.29×10^9 particles per mL and a τ_{exp} of 12.8 minutes (95% confidence intervals (CI): 8.1 – 31.1 minutes). With the help of Eq. 2 deduced N_0 value, the τ_{theor} was calculated to be 2.5 minutes. The sticking probability can be either calculated by taking the ratio of τ_{theor} to τ_{exp} or directly from the deduced N_0 and τ_{exp} values and the help of Eq. 3. For the condition with 0.01 mg/ml of total material concentration resulted in an average sticking probability of 0.19 (95% CI: 0.08 – 0.31).

The same data fitting approach was applied for two other concentrations with equal IgG:dextran sulfate ratio. The rationale behind the chosen condition was the assumption that the nature of the particles, hence the kinetics of the coagulation, will stay the same. The best-fit curves for the different studied conditions are shown in Figure 8. The curves indicate that the lowest concentration of the mixture shows a much slower decay, hence a larger τ_{exp} (41.6 minutes (95% CI: 25.8 – 107.9 minutes) for a total concentration of

0.005 mg/ml, versus 14.1 minutes (95% CI: 10.2 – 22.6 minutes) for 0.02 mg/ml), compared to the higher concentrations. Note that the NTA measurement of the 0.02 mg/ml sample at the first time point indicated a higher average size, compared to the other concentrations. This indicates that the particle coagulation for that concentration had proceeded to a further stage. Figure 8 also presents the average sticking probabilities (average values: 0.16 for 0.005 mg/ml; 0.19 for 0.01 mg/ml; 0.18 for 0.02 mg/ml). The average values were not significantly different (one-way Anova test: $P = 0.9573$).

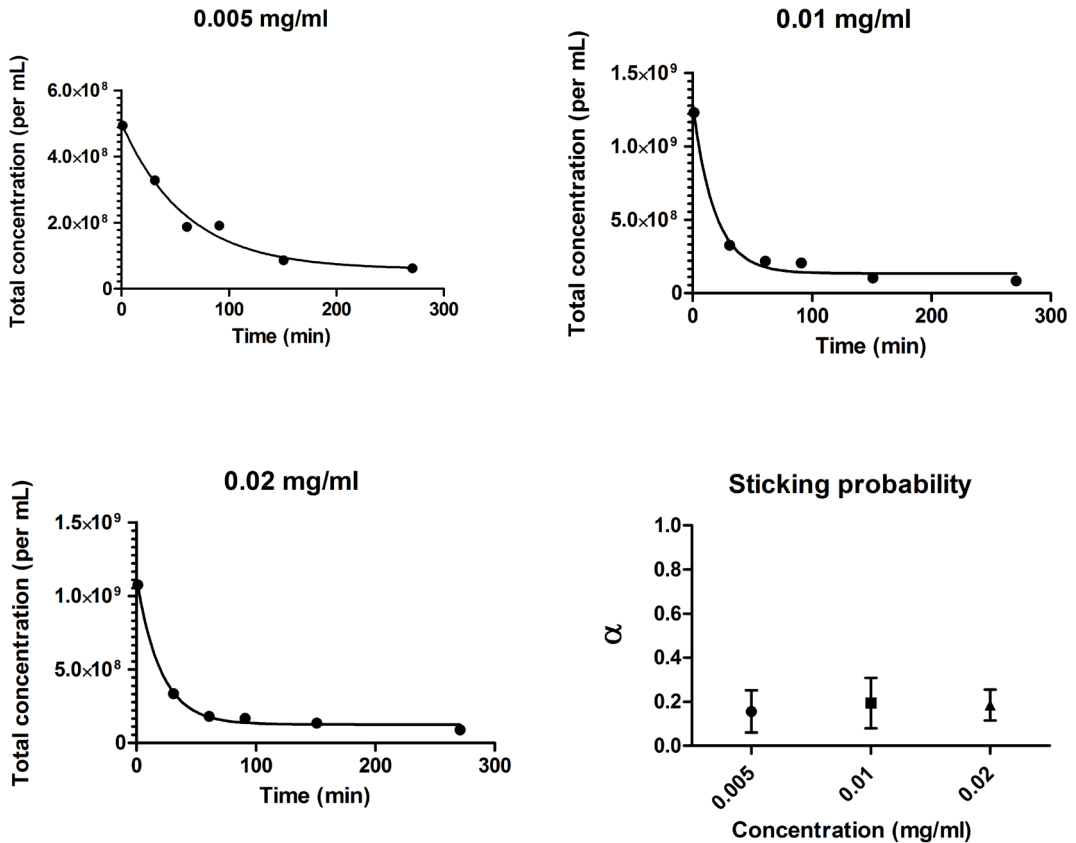


Figure 8: Total particle concentration over time for samples with 0.005, 0.01 and 0.02 mg/ml of each starting solution are shown. The solid lines show the best fit curve gained by using Equation 1 as a model. The graph in lower right corner presents the sticking probability calculated with the help of Equation 2 and 3. The error bars represent the 95% confidence interval.

Discussion

In this study we have shown the applicability of the combination of NTA and MFI for monitoring the particle formation and growth, when a dextran sulfate solution is added to an IgG solution. Analysis of particle concentration and size in both the nanometer- and the

micrometer-size range as function of time provides a good insight into the kinetics of the particle formation process, in terms of both particle size and particle concentration. As soon as the protein and the polyelectrolyte are mixed, the solution becomes supersaturated and electrostatic interactions lead to rapid formation of protein-polyelectrolyte complexes¹¹. At this point nucleation occurs with the appearance of primary particles, which is associated with a rapid loss of free monomeric IgG as demonstrated in our study by SEC analysis (Figure 2). This observation is in line with the literature reporting that the stage of aggregation of primary particles³⁹ into flocks is the rate-limiting step in the formation and growth of larger particles⁴⁰.

In this study NTA proved to be a valuable tool to study the interaction kinetics in the early stage, where no micron-sized agglomerates are formed yet. However, the progressive increase in larger particle concentrations made the NTA measurements increasingly difficult to perform and eventually impossible. This is due to inaccuracies caused by the presence of large particles (over 800 nm) with multiple scattering centers that rapidly change position, which erroneously leads to the detection of apparent very small particles (smaller than 100 nm).

Moreover, their brightness and size leads to masking and overlapping of particles. In addition, above this size the Brownian motion becomes very low, leading to additional inaccuracies²⁸. This was the reason for applying NTA only for the first part of the coagulation process (up to 440 min) and excluding the particles with sizes larger than 800 nm and smaller than 100 nm. Continuously decreasing concentrations of particles in the lower nanometer size range (101-400 nm) were accompanied by an initial increase followed by a moderate decrease in concentrations of larger nanoparticles (> 400 nm), as shown in Figure 3. The exponential decrease in total nanoparticle concentration (Figure 4) indicates that over time the smaller particles coagulated in order to form larger particles. However, the average particle size measured by NTA only increased at the start and afterwards remained fairly constant. That can be explained by the chosen lower limit for the NTA data (101 nm), leading to underestimation of the number of smaller particles²⁹.

In the later stage of the coagulation process, when the particle size entered the micrometer range, MFI took over the role of NTA to monitor particle growth. By displaying the measured microparticle size classes in 1- μ m bins, the consistency and precision of the technique in monitoring the particle growth process was revealed (Figure 5). The course of the total particle concentration showed a rapid growth, starting at about 90 minutes, and began to decrease slightly after about 600 minutes (Figure 6). This indicates that around this moment the low-nanometer particle population became depleted, while the growth within the micrometer range continued. The average particle size provided by the MFI was very large at the start, with a broad range, while the particle counts were very low. These results

are comparable to those obtained when only IgG or dextran sulfate solution was measured, pointing to the presence of small amounts of particulate impurities or contaminants in the starting materials. The average particle size by the end of the experiment was well below 5 μm , which is too small to provide us with reliable morphological parameters²⁷. The perikinetic coagulation theory, developed by Smoluchowski about a century ago, predicts the kinetics of particle growth due to Brownian motion driven collision of particles, with subsequent fusion into larger particles^{35,36}. This theory has been frequently used to derive information about the time evolution of the particle concentration as they cluster together. For instance, Fisher et al. used a Smoluchowski based population-balance model to describe the precipitation behavior of lysozyme by polyacrylic acid⁴¹. Chen et al. used Smoluchowski's perikinetic coagulation theory to describe the effect of mixing conditions on the flocculation kinetics of proteins in wastewater⁴². In our study the experimental data was fitted with a simple exponential decay model (Eq. 1), in order to deduce the initial particle concentration (N_0) and the experimental half-life (τ_{exp}). This was performed for 3 different concentrations of the starting materials (with equal mass ratios of the components in each). The physicochemical nature of the formed complexes restricts the success of each collision to fuse into a new larger particle. In case of protein-polyelectrolyte particles the surface could possess a net charge⁴³, which causes repulsion of similarly charged particles. However, polyelectrolyte bridging in-between particles is the main mechanism behind coagulation of protein-polyelectrolyte complexes⁴⁴. With respect to this restriction, the Smoluchowski model has some limitations, such as the assumptions that the colliding particles are spherical; every collision involves two particles of identical initial size; and each collision leads to a successful fusion²⁴, meaning that the sticking probability is unity and independent of the particle size. This is very unlikely and probably explains the difference between the experimental and theoretical half-life. With the deduced parameters from the fitting, we have calculated the collision efficiencies, which matched very well between the samples with different IgG and dextran sulfate concentrations.

Conclusion

The combination of NTA and MFI allowed us to analyze the growth kinetics of IgG/dextran sulfate complexes. Our data suggest that electrostatic interactions between IgG and dextran sulfate rapidly lead to the formation of particles. Due to particle collision these primary particles fuse and start to increase in size, leading to a rapid decrease in total nanoparticle concentration and a concomitant increase of new particles that grow further till they reach a size of 1-2 μm . The particle formation process could be described with the coagulation theory of Smoluchowski, provided that a collision efficiency term was introduced. Our approach provides novel insight into the kinetics and mechanism of protein-polyelectrolyte

complex formation and can be applied to other systems, such as complexes between polyelectrolytes and proteins, DNA, or other biomacromolecules.

References

1. Eichler HG, Aronsson B, Abadie E, Salmonson T 2010. New drug approval success rate in Europe in 2009. *Nature reviews Drug discovery* 9(5):355-356.
2. Leader B, Baca QJ, Golan DE 2008. Protein therapeutics: a summary and pharmacological classification. *Nature reviews Drug discovery* 7(1):21-39.
3. Mahler HC, Fischer S, Randolph TW, Carpenter JF. 2010. Protein aggregation and particle formation: effects of formulation, interfaces, and drug product manufacturing operations. In Wang W, Roberts CJ, editors. *Aggregation of therapeutic proteins*, ed., New Jersey: John Wiley & Sons. p 30.
4. Torosantucci R, Schoneich C, Jiskoot W 2014. Oxidation of therapeutic proteins and peptides: structural and biological consequences. *Pharmaceutical research* 31(3):541-553.
5. Wang W, Nema S, Teagarden D 2010. Protein aggregation--pathways and influencing factors. *International journal of pharmaceutics* 390(2):89-99.
6. Boeris V, Balce I, Vennapusa RR, Arevalo Rodriguez M, Pico G, Lahore MF 2012. Production, recovery and purification of a recombinant beta-galactosidase by expanded bed anion exchange adsorption. *J Chromatogr B Analyt Technol Biomed Life Sci* 900:32-37.
7. Xu Y, Mazzawi M, Chen K, Sun L, Dubin PL 2011. Protein purification by polyelectrolyte coacervation: influence of protein charge anisotropy on selectivity. *Biomacromolecules* 12(5):1512-1522.
8. Chang AC, Gupta RK 1996. Stabilization of tetanus toxoid in poly(DL-lactic-co-glycolic acid) microspheres for the controlled release of antigen. *Journal of pharmaceutical sciences* 85(2): 129-132.
9. Amidi M, Mastrobattista E, Jiskoot W, Hennink WE 2010. Chitosan-based delivery systems for protein therapeutics and antigens. *Adv Drug Deliv Rev* 62(1):59-82.
10. Nagpal K, Singh SK, Mishra DN 2010. Chitosan nanoparticles: a promising system in novel drug delivery. *Chem Pharm Bull (Tokyo)* 58(11):1423-1430.
11. Basak Kayitmazer A, Seeman D, Minsky BB, Dubin PL, Xu Y 2013. Protein-polyelectrolyte interaction. *Soft Matter* 9:30.
12. Crouzier T, Szarpak A, Boudou T, Auzely-Velty R, Picart C 2010. Polysaccharide-blend multilayers containing hyaluronan and heparin as a delivery system for rhBMP-2. *Small* 6(5): 651-662.
13. Gormally MV, McKibben RK, Johal MS, Selassie CR 2009. Controlling tyrosinase activity on charged polyelectrolyte surfaces: a QCM-D analysis. *Langmuir : the ACS journal of surfaces and colloids* 25(17):10014-10019.

- 14.** Lu Y, Wittemann A, Ballauff M 2009. Supramolecular Structures Generated by Spherical Polyelectrolyte Brushes and their Application in Catalysis. *Macromol Rapid Comm* 30(9-10): 806-815.
- 15.** De Temmerman ML, Rejman J, Vandenbroucke RE, De Koker S, Libert C, Grooten J, Demeester J, Gander B, De Smedt SC 2012. Polyelectrolyte LbL microcapsules versus PLGA microparticles for immunization with a protein antigen. *J Control Release* 158(2):233-239.
- 16.** Saurer EM, Flessner RM, Sullivan SP, Prausnitz MR, Lynn DM 2010. Layer-by-Layer Assembly of DNA- and Protein-Containing Films on Microneedles for Drug Delivery to the Skin. *Biomacromolecules* 11(11):3136-3143.
- 17.** McDonald P, Victa C, Carter-Franklin JN, Fahrner R 2009. Selective Antibody Precipitation Using Polyelectrolytes: A Novel Approach to the Purification of Monoclonal Antibodies. *Biotechnol Bioeng* 102(4):1141-1151.
- 18.** Holler C, Zhang CM 2008. Purification of an acidic recombinant protein from transgenic tobacco. *Biotechnol Bioeng* 99(4):902-909.
- 19.** Golubovic M, van Hateren SH, Ottens M, Witkamp GJ, van der Wielen LAM 2007. A method for lipase co-precipitation in a biodegradable protein matrix. *Biotechnol Bioeng* 98(6):1209-1218.
- 20.** Becker AL, Henzler K, Welsch N, Ballauff M, Borisov O 2012. Proteins and polyelectrolytes: A charged relationship. *Curr Opin Colloid In* 17(2):90-96.
- 21.** Cooper CL, Dubin PL, Kayitmazer AB, Turksen S 2005. Polyelectrolyte-protein complexes. *Curr Opin Colloid In* 10(1-2):52-78.
- 22.** Kizilay E, Kayitmazer AB, Dubin PL 2011. Complexation and coacervation of polyelectrolytes with oppositely charged colloids. *Adv Colloid Interfac* 167(1-2):24-37.
- 23.** Clark KM, Glatz CE 1987. Polymer dosage considerations in polyelectrolyte precipitation of protein. *Biotechnol Progr* 3:6.
- 24.** Meyer CJ, Deglon DA 2011. Particle collision modeling - A review. *Miner Eng* 24(8):719-730.
- 25.** Carpenter JF, Chemey B, Rosenberg AS. 2012. The critical need for robust assay for quantitation and characterization of aggregates of therapeutic proteins. In Mahler HC, Jiskoot W, editors. *Analysis of aggregates and particles in protein pharmaceuticals*, ed., New Jersey: John Wiley & Sons.
- 26.** Zolls S, Tantipolphan R, Wiggenghorn M, Winter G, Jiskoot W, Friess W, Hawe A 2012. Particles in therapeutic protein formulations, Part 1: Overview of analytical methods. *Journal of pharmaceutical sciences* 101(3):914-935.
- 27.** Anderson W, Kozak D, Coleman VA, Jamting AK, Trau M 2013. A comparative study of submicron particle sizing platforms: accuracy, precision and resolution analysis of polydisperse particle size distributions. *J Colloid Interface Sci* 405:322-330.
- 28.** Carr B, Wright M. 2013. Nanoparticle tracking analysis: A review of applications and usage 2010-2012. ed., Amesbury: NanoSight Ltd.

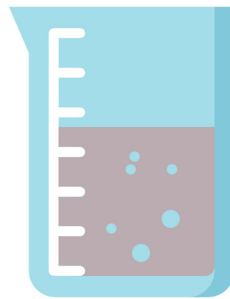
- 29.** Filipe V, Hawe A, Jiskoot W 2010. Critical evaluation of Nanoparticle Tracking Analysis (NTA) by NanoSight for the measurement of nanoparticles and protein aggregates. *Pharmaceutical research* 27(5):796-810.
- 30.** Van der Meeren P, Kasinos M, Saveyn H 2012. Relevance of two-dimensional Brownian motion dynamics in applying nanoparticle tracking analysis. *Methods in molecular biology* 906:525-534.
- 31.** Pedersen JS, Persson M 2014. Unmasking translucent protein particles by improved micro-flow imaging algorithms. *Journal of pharmaceutical sciences* 103(1):107-114.
- 32.** Telikepalli SN, Kumru OS, Kalonia C, Esfandiary R, Joshi SB, Middaugh CR, Volkin DB 2014. Structural Characterization of IgG1 mAb Aggregates and Particles Generated Under Various Stress Conditions. *Journal of pharmaceutical sciences* 103(3):796-809.
- 33.** Weinbuch D, Zolls S, Wiggenghorn M, Friess W, Winter G, Jiskoot W, Hawe A 2013. Micro-flow imaging and resonant mass measurement (Archimedes)--complementary methods to quantitatively differentiate protein particles and silicone oil droplets. *Journal of pharmaceutical sciences* 102(7):2152-2165.
- 34.** Zolls S, Weinbuch D, Wiggenghorn M, Winter G, Friess W, Jiskoot W, Hawe A 2013. Flow imaging microscopy for protein particle analysis--a comparative evaluation of four different analytical instruments. *The AAPS journal* 15(4):1200-1211.
- 35.** Smoluchowski M 1916. Drei Vorträge über Diffusion, Brownsche Molekularbewegung und Koagulation von Kolloidteilchen. *Physikalisch Zeitschrift* 17:28.
- 36.** Smoluchowski M 1917. Versuch einer mathematischen Theorie der Koagulationskinetik kolloider Lösungen. *Zeitschrift Fur Physikalische Chemie* 92:39.
- 37.** Filipe V, Kukrer B, Hawe A, Jiskoot W 2012. Transient molten globules and metastable aggregates induced by brief exposure of a monoclonal IgG to low pH. *Journal of pharmaceutical sciences* 101(7):2327-2339.
- 38.** Filipe V, Poole R, Oladunjoye O, Braeckmans K, Jiskoot W 2012. Detection and characterization of subvisible aggregates of monoclonal IgG in serum. *Pharmaceutical research* 29(8):2202-2212.
- 39.** Parker TG, Dalgleish DG 1997. The use of light-scattering and turbidity measurements to study the kinetics of extensively aggregating proteins: alpha-casein. *Biopolymers* 16:14.
- 40.** Kim WS, Hirasawa I, Kim WS 2001. Effects of experimental conditions on the mechanism of particle aggregation in protein precipitation by polyelectrolytes with a high molecular weight. *Chem Eng Sci* 56:9.
- 41.** Fisher RR, Glatz CE 1988. Polyelectrolyte precipitation of proteins: II. Models of the particle size distributions. *Biotechnol Bioeng* 32(6):786-796.
- 42.** Chen LA, Serad GA, Carbonell RG 1998. Effect of mixing conditions on flocculation kinetics of wastewaters containing proteins and other biological compounds using fibrous materials and

polyelectrolytes. Brazilian Journal of Chemical Engineering 15:10.

43. Carlsson F, Malmsten M, Linse P 2003. Protein-polyelectrolyte cluster formation and redissolution: a Monte Carlo study. J Am Chem Soc 125(10):3140-3149.

44. Chen W, Walker S, Berg JC 1992. The Mechanism of Floc Formation in Protein Precipitation by Polyelectrolytes. Chem Eng Sci 47(5):1039-1045.

Determination of the porosity of PLGA microparticles by tracking their sedimentation velocity using a flow imaging microscope (FlowCAM)



A.S. Sediq¹, S.K.D. Waasdorp¹, M.R. Nejadnik¹, M.M.C. van Beers^{1,2}, J. Meulenaar²,
R. Verrijck², W. Jiskoot^{1,*}

¹ Division of Drug Delivery Technology, Cluster BioTherapeutics, Leiden Academic Centre for Drug Research (LACDR), Leiden University, Leiden, the Netherlands

² Dr. Reddy's Laboratories Ltd., IPDO Leiden, the Netherlands.

Abstract

Purpose. To investigate whether particle sedimentation velocity tracking using a flow imaging microscope (FlowCAM) can be used to determine microparticle porosity.

Methods. Two different methods were explored. In the first method the sedimentation rate of microparticles was tracked in suspending media with different densities. The porosity was calculated from the average apparent density of the particles derived by intra- or extrapolation to the density of a suspending medium in which the sedimentation velocity was zero. In the second method, the microparticle size and sedimentation velocity in one suspending fluid were used to calculate the density and porosity of individual particles by using the Stokes' law of sedimentation.

Results. Polystyrene beads of different sizes were used for the development, optimization and validation of the methods. For both methods we found porosity values that were in excellent agreement with the expected values. Both methods were applied to determine the porosity of three PLGA microparticle batches with different porosities (between about 4 and 52%). With both methods we obtained microparticle porosity values similar to those obtained by mercury intrusion porosimetry.

Conclusion. We developed two methods to determine average microparticle density and porosity by sedimentation velocity tracking, using only a few milligrams of powder.

Introduction

Formulating active pharmaceutical ingredients (API) in controlled release systems is a potent strategy to maintain drug levels for prolonged periods within the therapeutic window, which may increase the efficiency of therapy, reduce the costs and improve patient compliance and comfort (1). Owing to their long clinical experience and favorable performance in terms of biodegradability and biocompatibility, PLGA microparticles fulfill the needs for controlled release in the area of parenteral pharmaceutical formulations, with a number of FDA approved drug products on the market today (2).

The porosity or void fraction of poly lactic-co-glycolic acid (PLGA) microparticles is a critical parameter known to affect the release kinetics of encapsulated drugs (3-5). Current approaches to determine the porosity of particulate drug delivery systems are based on established methods used in agricultural, petrochemical and constructional engineering (6). Among the available methods, mercury intrusion porosimetry (MIP) and gas (nitrogen) adsorption based methods are the most common and informative ones, because both can measure the pore size and its distribution. In addition, mercury porosimetry has the advantage of having certified reference material and standard measurement protocols (7). However, each of these methods has a number of major drawbacks. For instance, both methods require large amounts of sample (200-300 mg) for a single measurement. In addition, with MIP the difficulties are seen in distinguishing intra- and interparticulate pores (8). Besides, presence of enclosed pores may need additional MIP measurements with grinded material (9) and ink-bottle shaped and interconnected pores can lead to underestimation of the pore size (8). Toxic metal waste is yet another reason that would make the application of MIP less favorable. In contrast to MIP, with gas adsorption methods both open and enclosed pores are measured; however, the process of pressure equilibration may be very slow, resulting in long-lasting measurements for a single sample. Last but not least, although fully automated equipment is commercially available for both methods, such equipment is expensive and not available in many pharmaceutical laboratories.

Taking into account the drawbacks of the methods described above, there is need for a more straightforward method requiring small amounts of sample for deriving the overall porosity of (pharmaceutical) particulate systems. Considering the developments in flow imaging instruments with respect to image quality, sizing precision and accuracy (10) and their increasingly widespread use in pharmaceutical laboratories, we have evaluated sedimentation velocity tracking using a flow imaging microscope (FlowCAM) for measuring the density and porosity of PLGA microparticles. To our knowledge, in spite of the simplicity of the concept, a sedimentation based approach has not been used before to measure particle porosity. The velocity of a settling particle depends among other parameters on the size of the particle and the density difference between the liquid and the particle (11).

The density of each component of a microparticle (e.g., PLGA matrix, drug, and liquid or air filling the pores) contributes proportionally to the total microparticle density, and can therefore be used to calculate the porosity of a microparticle.

Here we present two methods using a FlowCAM to determine the porosity of PLGA microparticles. The results show that both methods generate porosity values close to those obtained with MIP, but require much smaller amounts of sample.

Materials and Methods

Materials

Cesium chloride (CsCl), polysorbate 80 and ethanol were obtained from Sigma (Sigma-Aldrich, Steinheim, Germany). Phosphate buffered saline (PBS; 8.2 g/L NaCl, 3.1 g/L Na₂HPO₄·12H₂O, 0.3 g/L NaH₂PO₄·2H₂O, pH 7.4) was purchased from Braun (B. Braun Melsungen AG, Germany) and filtered with a 0.22- μ m polyethersulfone-based syringe-driven filter unit (Millex GP, Millipore, Carrigtwohill, Ireland). Ultrapure water (18.2 M Ω .cm) was dispensed by using a Purelab Ultra water purification system (ELGA LabWater, Marlow, UK). Non-porous polystyrene sizing standards of different sizes (29.8 \pm 0.4, 50.2 \pm 0.5 and 69.1 \pm 0.8 μ m) were purchased from Duke Scientific (through Thermo Scientific, Fremont, CA, USA). Three batches of dried PLGA microparticles were kindly provided by Dr. Reddy's (IPDO, Leiden, the Netherlands). One of these batches (batch 1) contained no active pharmaceutical ingredient (API). The other two batches (2 and 3) were loaded with different amounts of an API. The microparticle batches had different porosities as measured with MIP, namely 4.0, 21.6, and 51.9% for batch 1, 2 and 3, respectively. The residual water content and residual organic solvent content of each PLGA microparticle batch were found to be lower than 0.5% (w/w) and were not taken into account.

Surface morphometry using scanning electron microscopy

Scanning electron microscopy (SEM, Nova NanoSEM, FEI, Eindhoven, the Netherlands) was used for high resolution imaging of the surface of PLGA microparticles. Microparticles were coated with a thin layer of gold in order to increase the surface conductivity. The instrument was operated at 15 kV and images were taken at magnifications between 50 and 400x.

Sample preparation for sedimentation velocity tracking

Solutions of PBS containing 0.01% (w/v) polysorbate 80 (PBS-T) were prepared with varying fluid densities by adding different concentrations of CsCl. Polysorbate 80 was included to facilitate wetting of the microparticles. The concentration of CsCl ranged from 0 – 75% (w/w), resulting in fluid densities ranging from about 1000 - 1655 kg/m³. The

density and viscosity of the used suspending fluids were observed to be dependent on the concentration of CsCl, and were taken into account in further calculations. All the measurements were performed at room temperature. A few drops of the concentrated polystyrene sizing standards were added to 10 mL of the PBS-T / CsCl solutions. For each polystyrene standard suspension, the sedimentation of 50 – 100 particles was tracked using FlowCAM. In order to study PLGA microparticle sedimentation, an appropriate amount of microparticles was suspended in PBS-T / CsCl to achieve a microparticle concentration of about 0.25 mg/mL (corresponding to approximately 7000 - 15000 particle counts/mL). These relatively low particle concentrations were chosen in order to avoid physical agglomeration and optical coincidence of settling particles. After addition of the suspending medium to the microparticles, the suspension was sonicated for 20 minutes and left at ambient conditions for at least 3 hours prior to analysis.

FlowCAM set-up for sedimentation velocity tracking

A FlowCAM VS1 system (Fluid Imaging Technologies, Yarmouth, ME, USA) equipped with a 300- μ m Field of View (FOV300; 300 μ m depth and 1500 μ m width) cell and 4x magnification lens was used in this study. VisualSpreadsheet software version 3 was used to control the system and to process the data. Prior to each measurement, the flow cell was rinsed with 2 mL particle-free suspending medium corresponding to the sample being measured. The background was calibrated by manually priming 0.5 mL of the same particle-free suspending medium. Hereafter, 1.5 mL of the sample was loaded and FlowCAM measurement was started with a flow rate of 0.20 mL/min and a camera rate of 10 frames/s. As soon as the sample had completely filled the flow cell and tubing (based on the volume estimated from the flow cell and tubing dimensions), the tubing was disconnected from the pump and both tubing ends were clamped to create a closed system in which there is no liquid flow. The analysis was stopped manually as soon as a sufficient number of particles was tracked (50 – 100 particles). The sample volume was set to 10 mL in the software settings to avoid premature, automatic termination of the analysis.

Sedimentation velocity from FlowCAM data

In order to optimize the measurement and to minimize the risk of tracking impurities or particles with anomalous settling behavior, the following particle inclusion criteria were used:

1. Edge gradient (average intensity of the pixels making up the outside border of a particle) values between 100 – 200 a.u. and aspect ratio values above 0.9. This criterion selects only particles that are in focus.
2. A distance of at least twice the diameter between the left/right edge of the particle and

vertical sides of the flow cell (determined with the help of X-coordinate and the known width of the field of view). This criterion discards particles that undergo retardation in velocity due to the left and right edges of the flow cell.

3. A straight vertical movement path of the particle found when the X- and Y-coordinates at each image is plotted (i.e., X-coordinate does not change more than 5 pixels during the entire track).

4. A constant particle displacement as a function of time.

In this way, only accurately sized particles without any unordinary settling motion were used for sedimentation velocity tracking.

The particles with properties that met the aforementioned criteria were extracted from the entire set of raw data. The Y-coordinate values (expressed in pixels) were converted to metric distances, with the use of image scale (named calibration factor in VisualSpreadsheet). After plotting the time (in seconds) against metric displacement, the velocity was found as slope of the linear regression with the help of Excel 2010 software.

In addition, the average values for properties such as area based diameter (ABD, the diameter based on a circle with an area that is equal to the projected particle area) and aspect ratio were extracted for each tracked particle.

Method 1: PLGA microparticle porosity from sedimentation velocity in fluids with varying densities (density-matching method)

The first approach that was used to derive the density and, subsequently, the porosity of analyzed particles consisted of tracking the individual particle sedimentation velocity in fluids with different densities. For each bead or microparticle suspension, the sedimentation velocity of individual particles was derived as described above. In order to normalize the derived velocities (v , in m/s) for particle size, they were divided by the corresponding average square diameter (calculated from ABD values; d^2 , in m^2). The resulting particle size-normalized sedimentation velocity (v/d^2 , in $m^{-1}s^{-1}$) values were based on the relation between velocity and diameter found in Stokes' law of sedimentation, as shown in Eq. 1:

$$v = \frac{(\rho_p - \rho_f)}{18\mu} g d^2 \quad \text{Eq. 1}$$

where ρ_p and ρ_f are the particle and fluid densities (in kg/m^3), respectively, μ is the dynamic viscosity of the fluid (in $kg/m.s$) and g is the gravitational acceleration (m/s^2). Note that (particle size-normalized) sedimentation velocity values will be positive for settling particles and negative for floating particles.

Subsequently, the average v/d^2 values for each bead size or PLGA microparticle batch

in different suspending media were plotted against the density of the corresponding suspending medium. Assuming that the particle would stagnate when its density is equal to that of the liquid, the intercept of a linear regression with the X-axis (density axis) was taken as the average particle density of the concerning polystyrene bead or PLGA microparticle batch. In case of a porous particle containing an active pharmaceutical ingredient (API), the particle density will be the sum of the fractional densities of (i) the matrix ($f_{\text{PLGA}} \times \rho_{\text{PLGA}}$), (ii) the API ($f_{\text{API}} \times \rho_{\text{API}}$) and (iii) the pores ($f_{\text{pore}} \times \rho_{\text{pore}}$). Assuming that the pores are filled with air (i.e., $\rho_{\text{pore}} = 0$; further explained in the *Discussion* section), Eq. 2 was used to calculate the density derived particle porosity (φ in %) (6):

$$\varphi = \frac{\rho_{\text{solid}} - \rho_p}{\rho_{\text{solid}}} 100\% \quad \text{Eq. 2}$$

where in which ρ_{solid} is the density of the solids, i.e., API and the PLGA matrix, and f_{API} and f_{PLGA} are the weight fractions of the API and the PLGA, respectively, in the solids content (derived from the drug loading in percent).

Method II: PLGA microparticle porosity from sedimentation velocity using Stokes' law (Stokes derived method)

For the second method only the particles tracked in a suspending fluid having a density close, but not equal, to the expected particle density were used. As compared to high sedimentation velocities, low sedimentation velocities result in more accurate density determinations, because of the large number of 2D-coordinate data points gained from a large number of images taken during the particle tracking time lapse. Subsequently, the density and resulting porosity of individual particles were calculated, by means of Stokes' law.

Bach et al. derived equations for calculating the density of a settling particle in a fluid (12). Here, we used the same approach, but with porosity of the particle as the final outcome. The Stokes' law of sedimentation was used as a starting point for the calculations. This formula gives a mathematical description for the drag force exerted on spherical objects when the Reynolds number is very small ($Re \ll 0.1$) (13). The Reynolds numbers associated with the relative flow of particles tracked in our study were calculated to be $\ll 0.01$, using Eq. 3:

$$Re = \frac{vd\rho_f}{\mu} \quad \text{Eq. 3}$$

Incorporating equivalent of ρ_p from equation 2 in equation 1, and rewriting it to porosity (%) leaves us with the following:

$$\varphi = \frac{\rho_{solid} - (\rho_f + \frac{18\mu v}{gd^2})}{\rho_{solid}} 100\% \quad \text{Eq. 4}$$

In our calculations, in case of particle diameters equal to or larger than 50 μm we also applied a correction for the sedimentation velocity with respect to the retarding effect by the presence of the FlowCAM cell wall:

$$v_{wc} = \frac{v_{measured}}{1 - k(\frac{d}{D})} \quad \text{Eq. 5}$$

Here, the experimentally measured velocity ($v_{measured}$) is corrected for coefficient of drag (k), particle diameter (d) and the shortest distance of the particle edge and the wall (D), to eventually gain the velocity corrected for the wall effect (v_{wc}). The coefficient of drag depends on the shape of the space where settling takes place, and had a value of 1.004 (12). We also took into account the effect of particle shape on the sedimentation velocity. For this purpose, based on the FlowCAM and SEM images, we have used the corrections specifically for prolate ellipsoid shapes (14):

$$v = v_{wc} \frac{\frac{8}{3}(\beta^2 - 1)}{\frac{\beta(3\beta^2 - 2)}{(\beta^2 - 1)^{\frac{1}{2}}} \tan^{-1}\left((\beta^2 - 1)^{\frac{1}{2}}\right) - \beta} \quad \text{Eq. 6}$$

where

$$\beta = \frac{1}{AR}$$

where β is the reciprocal aspect ratio. As seen in equation 6, the final velocity (v) is achieved by correcting the wall-effect-corrected velocity (v_{wc}) using the average aspect ratio of each particle from the analyzed FlowCAM data.

Results

Sedimentation velocity data processing and analysis set-up using polystyrene beads

FlowCAM was used to determine the sedimentation velocity of microparticles in aqueous liquids. The velocity value was then used to derive the density of the microparticles. From the density and known composition of the microparticles the porosity was calculated.

Derivation of the sedimentation criteria to include a particle in the density calculations, corrections for influential parameters on the sedimentation (e.g., wall and shape effect) and the validation of the method were studied and performed by using polystyrene beads of three different sizes. In the supplementary document the development of the first selection criterion (Supplementary Figure S1) and the wall correction (Supplementary Figure S2) are explained in detail.

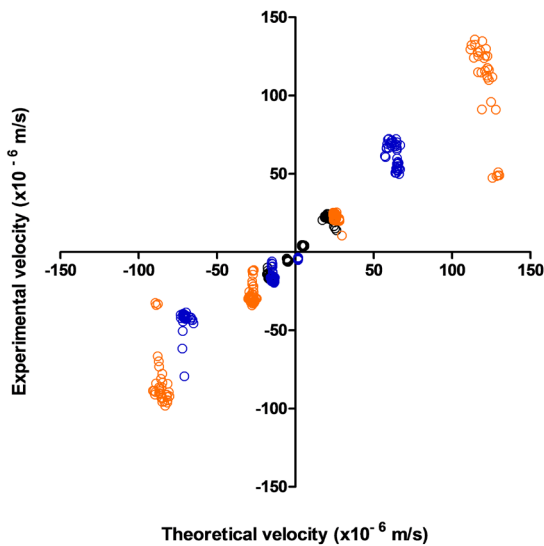


Figure 1: Theoretical sedimentation velocities plotted against experimental sedimentation velocities of polystyrene size standards suspended in liquids with different densities: 30- μm beads (black circles), 50- μm beads (blue circles) and 70- μm beads (orange circles). For the 50- μm and 70- μm beads, a correction for the wall effect was applied. The theoretical sedimentation velocity was calculated by using the measured size of the concerning particle and the bead density (1050 kg/m^3) as provided by the manufacturer.

Figure 1 shows that the experimental sedimentation velocities (corrected for the wall effect) of all the polystyrene beads are in excellent correspondence with the theoretical values. This indicates that determining the density through measurement of the sedimentation velocity using a FlowCAM is possible for particles widely ranging in size and density difference (with respect to the suspending liquid), when applying the inclusion criteria named in *Materials*

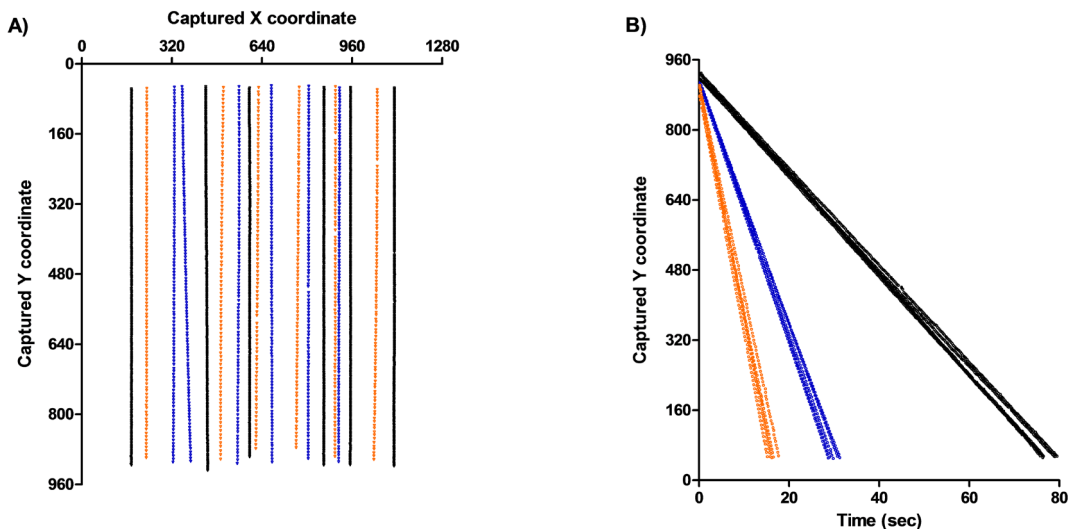


Figure 2: Polystyrene bead displacements in the 2-dimensional plain (graph A) and in time (graph B). The position of a settling particle in each image captured by FlowCAM is given by the X- and Y-coordinates in terms of pixel number from the lower left corner. This way the path of a settling particle can be derived, by making a scatter plot of the coordinates against the tracked time. This is illustrated in graph A for a number of beads of each polystyrene size standard (30- μm beads in black; 50- μm beads in blue; 70- μm beads in orange). In graph B the displacement in the Y-axis over time of the particles from graph A are shown. The slopes of these lines represent individual settling velocities (pix/s).

The complete data set of the particles fulfilling the inclusion criteria was extracted from the raw data and the physical displacement through the field of view was visualized by plotting the X- and Y-coordinates, as shown in Figure 2A. At this point only the particles with a settling distance from the left or right flow cell border of at least two times the particle diameter and showing a vertical settling path were selected to be included in the analysis. In the last step of data processing, the vertical displacement was plotted against time, for individual particles, where the slope of the deduced line corresponds to the sedimentation velocity of the particle. Figure 2B illustrates that the slopes, representing the sedimentation velocities, increase with increasing polystyrene bead size, as expected.

The same polystyrene beads of different sizes were used to validate the two methods applied in our study. For *Method 1* (the density-matching method), particle sedimentation velocities were determined in liquids with different densities and the results are shown in Figure 3. The relation between fluid density and particle size-normalized sedimentation velocity (v/d^2) was shown to be linear (R^2 above 0.97), with nearly the same slope for all beads (-2206 ± 45 vs. -2127 ± 87 ; -2253 ± 36 for 30-, 50- and 70- μm beads, respectively).

Method validation using polystyrene beads

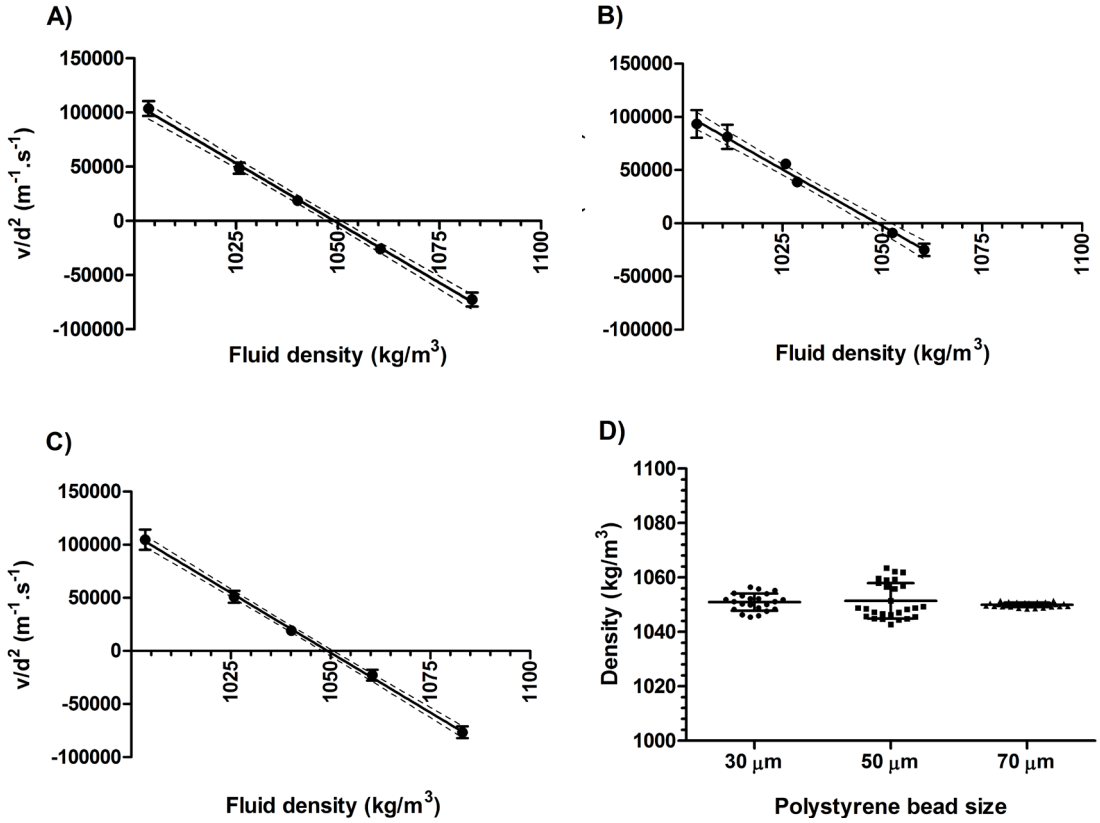


Figure 3: The validation results of the two sedimentation based methods for porosity measurements, using polystyrene size standards. Panels A – C show the relation between fluid density and particle size-normalized sedimentation velocity (v/d^2) for 30- μm , 50- μm and 70- μm beads, respectively. Each data point represents the average and standard deviation of the v/d^2 derived from tracking of at least 20 individual particles in the corresponding fluid density. The linear relation between fluid density and sedimentation velocity is denoted as the solid line, with the 95% confidence of interval of the linear relation between the dashed lines. Note that only for 50- μm and 70- μm beads the attained velocities were corrected for the wall effect. Panel D shows density distributions of the investigated polystyrene beads in fluids closest to the nominal polystyrene density (i.e., fluid density of 1040, 1052 and 1060 kg/m^3 , respectively, for 30-, 50- and 70- μm beads).

Using linear regression on the data points helped finding the intercept with the X-axis, which corresponds to the average density of the corresponding particles. In case of polystyrene beads the derived particle density appeared to be statistically equal to the reference values from the manufacturer (see Table 1). Altogether, these results demonstrate the validity of the method.

For *Method II* (the Stokes derived method) only the data from a fluid having a density close to the expected bead density was used in order to obtain sedimentation velocity values with the highest possible accuracy. As explained in the *Materials and Methods* section, the individual particle velocities were used to calculate the particle density through Stokes' law of sedimentation, after corrections for shape and wall effect. The results listed in Table 1 show that the polystyrene bead densities determined for each bead size were comparable to the specifications from the manufacturer. With *Method II* the density distribution of the polystyrene beads could be derived, as shown in Figure 3D. Moreover, from the ratio of the calculated and given density distribution the porosity distributions were derived. The porosity values of polystyrene beads were calculated to be in the range of $0.1 \pm 0.1\%$ for 30 and 50 μm beads and $0.0 \pm 0.1\%$ for the 70 μm beads, which is in excellent agreement with the expected value of zero for solid beads.

In conclusion, we have established two valid methods to determine microparticle density and porosity based on sedimentation velocity tracking. In addition, with *Method II*, one is able to derive the density distribution and hence the porosity distribution.

Sedimentation velocity tracking for determining PLGA microparticle porosity

The shape of the PLGA microparticles was studied by using the images and morphological data provided by FlowCAM as well as with SEM imaging (Figure 4). Batches 1 and 2 appeared to have predominantly spherical particles with a smooth surface, whereas batch 3 contained mainly misshaped particles, with highly irregular surfaces. Also with FlowCAM, these morphological properties were distinguishable, albeit with a less detailed resolution compared to SEM. These differences were apparent from a number of morphological descriptors, in particular aspect ratio, circle fit, circularity, intensity and transparency (Table 2).

Table 1: Densities of polystyrene beads obtained by sedimentation velocity tracking with the density-matching method (Method I) and the Stokes derived method

Specifications provided by the manufacturer		Sedimentation velocity tracking		
Average size \pm SD (μm)	Average density (kg/m^3)	<i>Method I</i>		<i>Method II</i>
		Average density \pm SD (kg/m^3) ¹	Goodness of fit (R^2)	Average density \pm SD (kg/m^3) ²
29.8 \pm 0.4	1050	1050 \pm 3	0.988	1049 \pm 1
50.2 \pm 0.5		1049 \pm 3	0.968	1049 \pm 1
69.1 \pm 0.8		1050 \pm 2	0.994	1050 \pm 1

¹ mean and standard deviation ((SD), derived from measurements in 5-6 different suspending liquids) of the density and the goodness of fit.

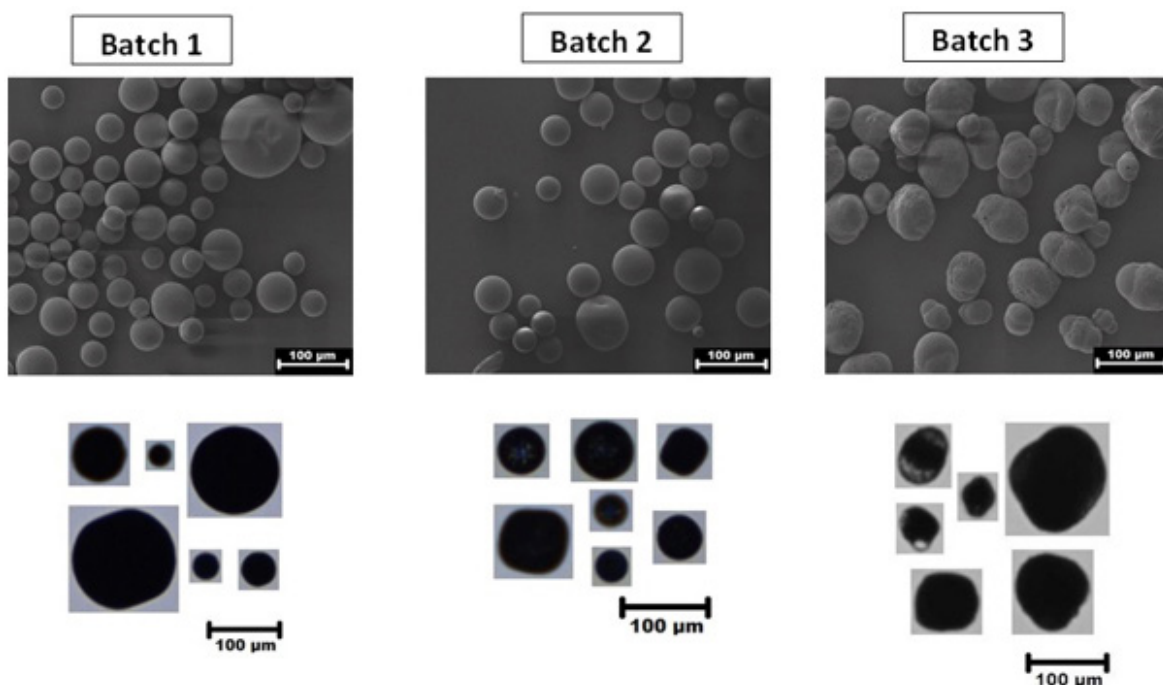
² density distributions (n = 20 particles)

Table 2: Morphological parameters of the different PLGA microsphere batches.

Micro-particle batch	Aspect ratio		Circle fit		Circularity		Intensity	
	Mean	SD	Mean	SD	Mean	SD	Mean	SD
1	0.982	0.010	0.959	0.004	0.954	0.006	52.83	3.93
2	0.980	0.007	0.957	0.003	0.927*	0.015	45.94	18.26
3	0.862*	0.070	0.844*	0.067	0.907*	0.027	19.80*	7.51

*Significantly different from the other batch(es) (one-way Anova ($p < 0.0001$) followed by post-hoc Tukey's multiple comparison test ($p < 0.05$))

compared to SEM. These differences were apparent from a number of morphological descriptors, in particular aspect ratio, circle fit, circularity, intensity and transparency (Table 2).

**Figure 4:** Representative high resolution scanning electron microscopy (upper panels) and FlowCAM images (lower panels) of the different PLGA microsphere batches.

The two validated methods were then used to obtain the microsphere porosity, derived from the density (calculated as shown in the *Materials and Methods* section), for 3 different PLGA microsphere batches. As shown in Figure 5A-C, for each of the batches a linear relation was found between fluid density and average v/d^2 , with a R^2 value above 0.9. According to the density-matching method (*Method 1*), the regression model for each batch was used to find the X-intercept, representing the average microsphere density, which

resulted for all batches in a similar porosity value as measured by MIP (Table 3). Noticeably, compared to the other two batches, batch 3 showed a relatively high standard deviation for the average porosity. In addition, the determined porosity of batch 3 tended to be lower than that obtained by MIP. For all batches, the Stokes derived method (*Method II*) showed similar porosity values as compared to those obtained by *Method I*. For this purpose the results from the fluid density closest to the matching density value (data point closest to the X-intercept in Figure A-C) were used. Furthermore, for each batch the porosity distribution was derived. As shown in Figure 5D, a relatively broad porosity distribution was found for batch 3 as compared to the other batches.

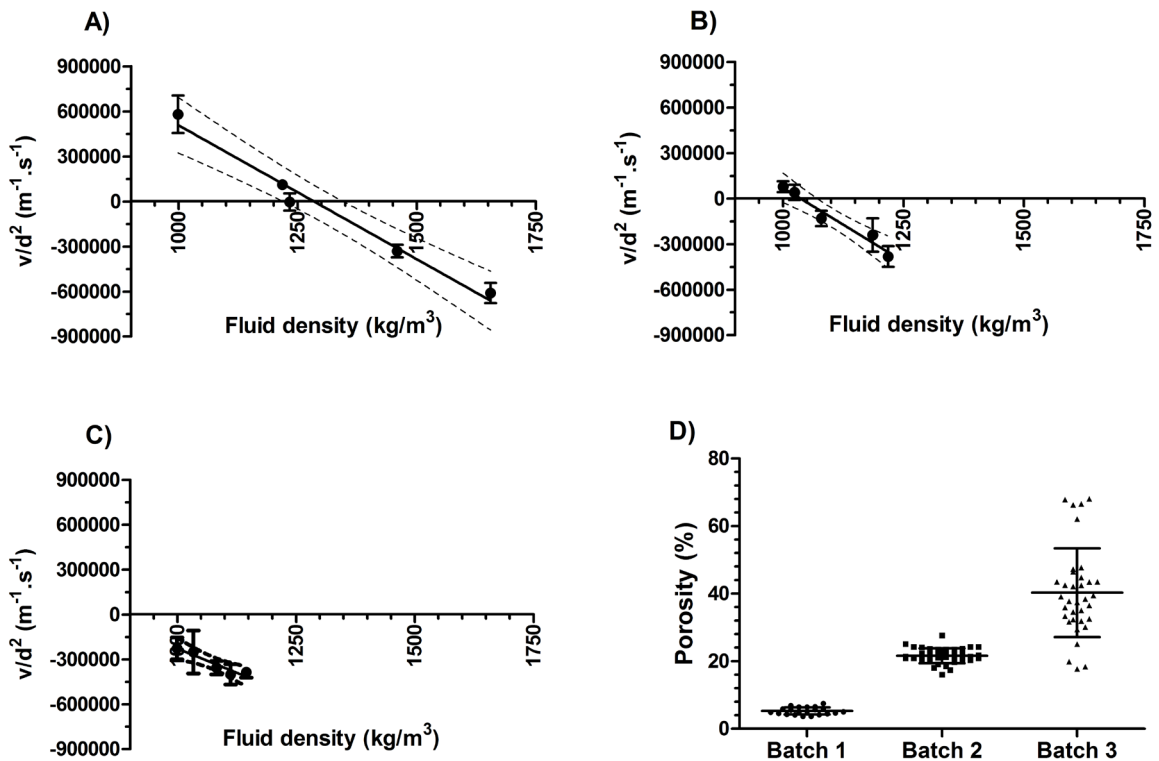


Figure 5: Results of the two sedimentation based methods applied for porosity measurements of the different PLGA microparticle batches. Panels A – C show the relation between fluid density and particle size-normalized sedimentation velocity (v/d^2) for three different batches (batch 1, 2 and 3, respectively). Each data point represents the average and standard deviation of the sedimentation velocities derived from tracking of at least 20 individual particles in the corresponding fluid density. The linear relation between fluid density and v/d^2 is denoted as the solid line, with the 95% confidence of interval of the linear relation between the dashed lines. Panel D shows porosity distributions of the investigated PLGA microparticle batches in fluids closest to the nominal PLGA microparticle density (i.e., fluid density of 1233, 1023 and 999 kg/m³, respectively, for batch 1, 2 and 3).

Table 3: Densities and porosities of 3 PLGA microparticle batches obtained by sedimentation velocity tracking with the density-matching method (Method I) and the Stokes derived method (Method II).

Micro-particle batch	Mercury intrusion porosimetry		Sedimentation velocity tracking				
	Porosity (%)	Expected density range (kg/m ³) ¹	Method I		Goodness of fit (R ²)	Method II	
			Average density ± SD (kg/m ³) ²	Average porosity ± SD (%) ²		Average density ± SD (kg/m ³) ³	Average porosity ± SD (%) ³
1	4.0	1313 – 1332	1284 ± 43	4.2 ± 3.2	0.979	1270 ± 11	5.2 ± 0.9
2	21.6	1028 – 1243	1036 ± 31	21.9 ± 2.3	0.960	1039 ± 29	21.6 ± 2.2
3	51.9	626 – 1135	823 ± 177	39.1 ± 13.3	0.903	801 ± 152	39.8 ± 11.4

¹ calculated from the known solid composition of the PLGA microparticle batch, assuming that the pores were filled with air (lower values) or suspending liquid (upper values). ² mean and standard deviation ((SD), derived from measurements in 5-6 different suspending liquids) of the density and the goodness of fit. ³ density or porosity distributions (n = 20 particles).

Discussion

With the increasing need for controlled drug release formulations, the characterization of these systems becomes increasingly important. This holds true in particular for the determination of the porosity, for which complex, time- and material-consuming methods such as MIP and gas adsorption are generally used. In our study we have evaluated the feasibility to determine the porosity of individual microparticles from their sedimentation rate in a liquid. Because of its reported applicability for sedimentation rate determination (12), we selected a FlowCAM for our investigation. Tracking of the sedimentation velocity of microparticles becomes possible by obstructing the liquid flow after introduction of the sample into the flow cell of the instrument.

The precision and accuracy of sizing are very important for the purpose of obtaining the correct particle density by sedimentation velocity tracking. Fortunately, the methods developed here do not require the counting (and sizing) of all particles in the suspension, unlike in conventional applications of flow imaging microscopy where particle concentration often is an important output parameter (10). Therefore, we have explored possibilities to use the image-derived data of individual particles to select only particles that are in focus (to allow accurate sizing) and show regular settling behavior (to enable accurate determination of the sedimentation velocity).

This resulted in a number of inclusion criteria that were used as indicators for the aforementioned characteristics (size and settling behavior). The considerable (quadratic) effect of particle diameter on the calculated sedimentation velocity (cf. Eq. 2) was in

particular important to consider. In order to decrease potential errors related to this effect, we investigated appropriate instrument settings for our method development. As FlowCAM offers the operator the advantage to choose the magnification, we have tested the influence of magnification magnitude on the sizing precision and accuracy of 5- μm and 20- μm beads in an additional study (Supplementary Figure S3). The outcome of that study indicates that the use of a lower lens magnification improves the sizing precision and accuracy of the instrument. An additional advantage of a lower magnification is that it would result in a larger field of view, thus in a larger sedimentation path that could be tracked, which is beneficial for the accuracy of the sedimentation velocity calculation.

We found the edge gradient parameter to be a useful indicator for focus, and therewith for accuracy of the sizing. The intensity of the outer border of the particle determines the edge gradient value. Here, a low edge gradient number may indicate that the edge of the particle is spread out, as that happens with out-of-focus particles, and a very high value indicates a very sharp contrast at the edge of the particle. All the pixels inside the edge border are eventually used to determine the area of the particles, which in turn is used to calculate the diameter (ABD). Our study indicates that very sharp contrast leads to underestimation of the particle size and therefore both a lower and an upper limit for the edge gradient were included in the particle selection criteria (100 – 200 a.u.). The edge gradient values of the PLGA microparticles were found to lie between 75 and 223. Polystyrene beads showed overall comparable (very dark) greyscale intensity as the PLGA microparticles that we studied. Also the refractive index of PLGA and polystyrene do not differ that much (1.46 and 1.59, respectively). In this case it is valid to consider that the edge gradient range that is chosen based on the polystyrene bead study, would be suitable for the PLGA microparticles as well. In case one wants to study the density (and/or porosity) of more transparent microparticles, the edge gradient range that represents in-focus particles may differ. Furthermore, the focal plane in the flow cell is ideally positioned in the middle of the depth of field of view, where particles in focus are assumed to have the maximum distance from the front and rear wall of the flow cell, hence the lowest resistance effects from these two walls. Despite these measures, one has to realize that the effect of imperfect focus and particle edge definition on the sizing may result in some errors in the density calculations and may be (at least partly) responsible for the distributions found for each group of the presumably uniformly dense polystyrene beads.

The methods we developed here can be deterrent because they may seem to involve time-consuming processes. This holds true for the utilization of the inclusion criteria for a dataset of settling particles and for the procedure in *Method 1* of tracking the sedimentation in different liquids and then finding the apparent density through intrapolation of the linear relation between fluid density and size-normalized sedimentation velocity (v/d^2). However,

the length of this part of the method can be easily reduced to even minutes if a computing toolbox based on a package like MatLab is used to test the named selection criteria on the whole data set and derivation of individual sedimentation rates with subsequent corrections and porosity calculations. This is particularly valuable when the method is used for routine analysis of, e.g., microparticle batches.

Suspending fluids with a higher density than the expected particle density were chosen to confirm the applicability of the method for particles with a relatively low density, such as highly porous PLGA microparticles. Such particles would move upwards (float) in conventional suspending media, resulting in negative sedimentation velocity values. In the experiments where polystyrene beads of different sizes were found to be floating, the calculated densities were the same as provided by the manufacturer. This highlights the applicability of this method for a wide range of particle sizes, densities and porosities. The altered conditions in our study concerned fluid density, but theoretically fluid viscosity could be another parameter to adjust.

For the density calculations using Stokes' formula we have only used the data of particles in fluids with a density close to the particle density. In addition, as seen from Figure 1, the precision of the sedimentation velocity determination increases when the particle density is close to the fluid density. A significant added value of *Method II* over *Method I* lies in the fact that the final mean and standard deviation of the density (and hence porosity) from second approach resembles the population mean and the variability in it. In *Method I* the averages and standard deviations of different populations in different liquids are used to calculate a mean and standard deviation of the batch density (and porosity).

One has to realize that the first raw outcome of the approaches presented in this study is the sedimentation velocity of particles, which is proportional to the apparent density of the particle. Therefore, the method is a reliable approach for measurement of the density of the particles as evidenced by investigation of the standard polystyrene beads. Deduction of porosity from the apparent density needs some assumptions, the most important of which concerns the filling of the pores, with air or suspending fluid.

In a preliminary study we have investigated the effect of the time lag (up to 4 days) between the preparation of the microparticle suspension (batch 3) and the measurement. We found that the equilibration time did influence the density of the particles, especially after 24 h of incubation. This may be caused by a change of pore properties due to release of the API and potential degradation of the PLGA. Therefore, we fixed the equilibration time to 3 hours, which should be long enough for wetting of the surface of the particles and short enough to avoid major changes in the pore properties.

Considering the hydrophobic properties of the PLGA and the use of aqueous suspending media, one can expect that the diffusion of water through a primarily hydrophobic matrix

would be considerably delayed. The assumption of air-filled pores for the porosity calculations appeared to be fair when the MIP data was compared to the porosity calculations based on flow imaging experiments. The results summarized in Table 4 indicate that the obtained densities of the PLGA particles from all batches are closer to those calculated from the MIP porosity data when pores are assumed to be filled with air. It has to be realized, however, that partial filling of the pores with liquid cannot be totally ruled out and it may be a source of the relatively large SD for batch 3 compared to the other 2 batches.

Due to low nominal density of some PLGA particle batches and the presence of air-filled pores, getting a particle density higher than the density of water was not possible for all particles and therefore conditions for particle settling could not always be achieved, not even in absence of cesium chloride. Decreasing density of an aqueous solution can be realized by addition of alcohols. However, it was observed in a small experimental trial that the presence of ethanol caused aggregation of microparticles. Nevertheless, velocity measurements in different fluids showed a good linear relation, in terms of R^2 values, in particular for the first two batches, suggesting that an extrapolation of the data points to obtain the intercept would be justified. PLGA microparticle batch 3 showed the lowest degree of linear fit and the lowest precision of the density and porosity determination. This may be due to the highly uneven shape and surface of these microparticles compared to the others, as well as the much higher porosity. Nevertheless, the obtained porosity was similar to the value obtained by MIP and significantly different ($p < 0.05$) from the porosities obtained for the other tested PLGA microparticles.

With *Method II* sedimentation of individual particles is measured (therewith porosity of individual particles) and the mean and standard deviation of the investigated particle population is calculated. The larger relative standard deviation in the density (and hence porosity) that is seen for batch 3 may also be considered as an existing wide porosity distribution for this specific batch. Therefore, the second approach provides better insight into the porosity details on particle level, which is an advantage over *Method I* and the conventional methods for porosity determinations.

Conclusion

In conclusion, we have developed, optimized and validated two sedimentation velocity tracking methods to assess the porosity of micron sized particles. For this purpose we used a FlowCAM instrument, but it is expected that the methods can be transferred to other flow imaging microscopes as well. For three batches of PLGA microparticles widely differing in porosity, both methods yielded porosity values that were similar to the values obtained by MIP, while requiring up to 100-fold smaller amounts of material. The methods could therefore be useful as a viable alternative to conventional methods for determining

microparticle density and porosity.

References

1. Park K. Controlled drug delivery systems: past forward and future back. *J Control Release*. 2014 Sep 28;190:3-8. PubMed PMID: 24794901. Pubmed Central PMCID: 4142099.
2. Mundargi RC, Babu VR, Rangaswamy V, Patel P, Aminabhavi TM. Nano/micro technologies for delivering macromolecular therapeutics using poly(D,L-lactide-co-glycolide) and its derivatives. *J Control Release*. 2008 Feb 11;125(3):193-209. PubMed PMID: WOS:000253745100002. English.
3. Klose D, Siepmann F, Elkharraz K, Krenzlin S, Siepmann J. How porosity and size affect the drug release mechanisms from PLGA-based microparticles. *International journal of pharmaceutics*. 2006 May 18;314(2):198-206. PubMed PMID: WOS:000237905200012. English.
4. Vyslouzil J, Dolezel P, Kejdusova M, Maskova E, Masek J, Lukac R, et al. Influence of different formulations and process parameters during the preparation of drug-loaded PLGA microspheres evaluated by multivariate data analysis. *Acta Pharm*. 2014 Dec;64(4):403-17. PubMed PMID: 25531782.
5. Mao SR, Xu J, Cai CF, Germershaus O, Schaper A, Kissel T. Effect of WOW process parameters on morphology and burst release of FITC-dextran loaded PLGA microspheres. *International journal of pharmaceutics*. 2007 Apr 4;334(1-2):137-48. PubMed PMID: WOS:000245774400017. English.
6. Ezekwe N. *Petroleum reservoir engineering practice*. First ed. New Jersey: Prentice Hall; 2010.
7. Espinal L. Porosity and its measurement. In: *Technology NloSa*, editor.: NIST; 2012.
8. Vay K, Scheler S, Friess W. New insights into the pore structure of poly(D,L-lactide-co-glycolide) microspheres. *International journal of pharmaceutics*. 2010 Dec 15;402(1-2):20-6. PubMed PMID: WOS:000287341200003. English.
9. Webb PA. *An Introduction To The Physical Characterization of Materials by Mercury Intrusion Porosimetry with Emphasis On Reduction And Presentation of Experimental Data*. Norcross, Georgia: Micrometrics Instrument Corp., 2001.
10. Zolls S, Weinbuch D, Wiggenghorn M, Winter G, Friess W, Jiskoot W, et al. Flow imaging microscopy for protein particle analysis--a comparative evaluation of four different analytical instruments. *The AAPS journal*. 2013 Oct;15(4):1200-11. PubMed PMID: 23996547. Pubmed Central PMCID: 3787219.
11. Batchelor GK. *An introduction to fluid dynamics*. Cambridge,: U.P.; 1967. xviii, 615 p. p.
12. Bach LT, Riebesell U, Sett S, Febiri S, Rzepka P, Schulz KG. An approach for particle sinking velocity measurements in the 3-400 μ m size range and considerations on the effect of temperature on sinking rates. *Mar Biol*. 2012 Aug;159(8):1853-64. PubMed PMID: WOS:000306731300020. English.
13. Batchelor GK. *An Introduction to Fluid-Dynamics - a Citation-Classic Commentary on an*

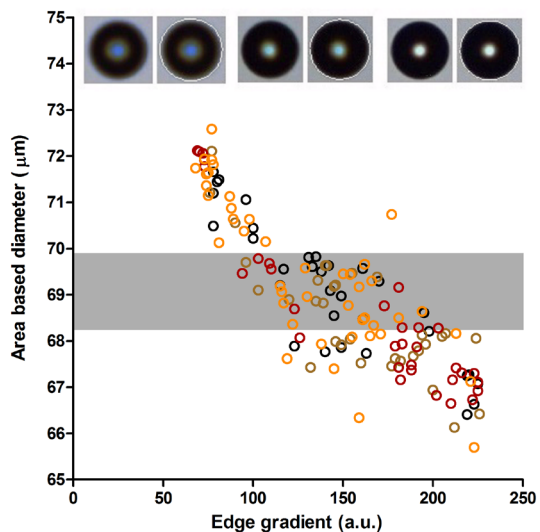
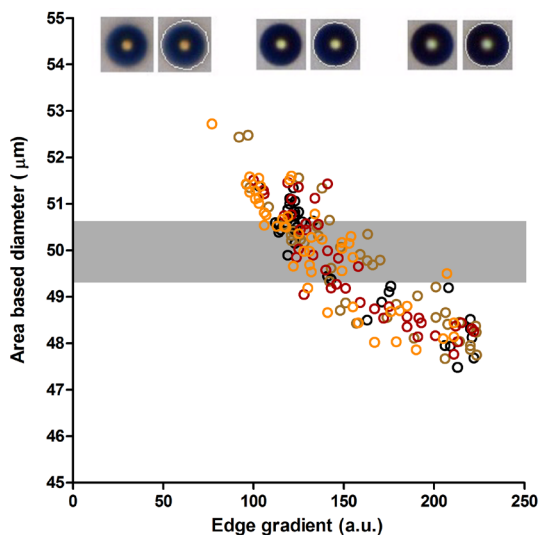
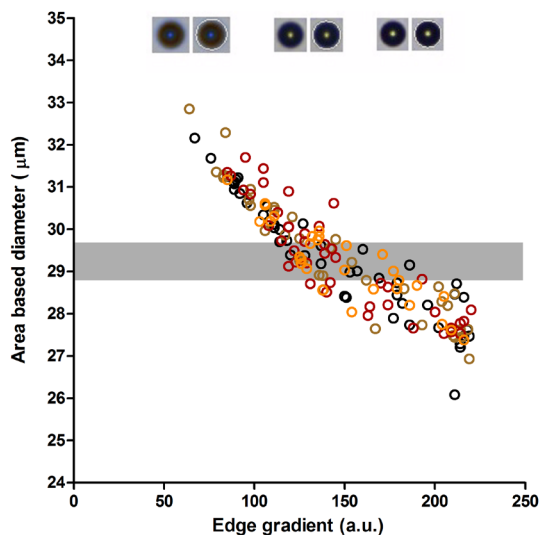
Introduction to Fluid-Dynamics by Batchelor,G.K. Cc/Phys Chem Earth. 1992 Oct 5(40):8-

PubMed PMID: WOS:A1992JN25000001. English.

14. Deo S, Datta S. Stokes flow past a fluid prolate spheroid. Indian J Pure Ap Mat. 2003

May;34(5):755-64. PubMed PMID: WOS:000184178400009. English.

Supporting Information



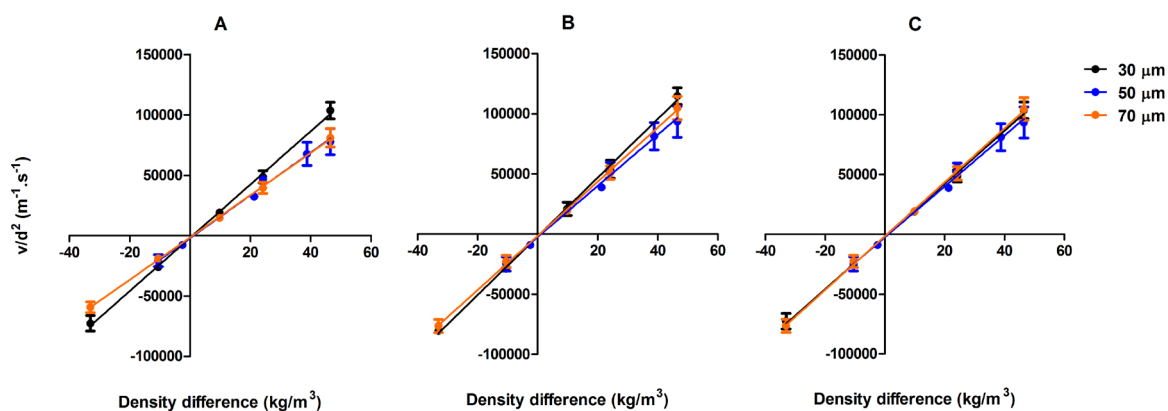
- 1003.5 kg/m^3
- 1025.8 kg/m^3
- 1040.1 kg/m^3
- 1060.5 kg/m^3

Supplementary Figure S1:

Area based diameter (ABD) of the three tested polystyrene beads plotted against the corresponding edge gradient value. The color of each open circle represents a single particle analyzed in a suspending medium having the density as indicated in the legend. The grey bar indicates the average and standard deviation of the size as stated by the manufacturer. Images on top of the graphs are deduced from the analysis, each pair corresponding to a particle

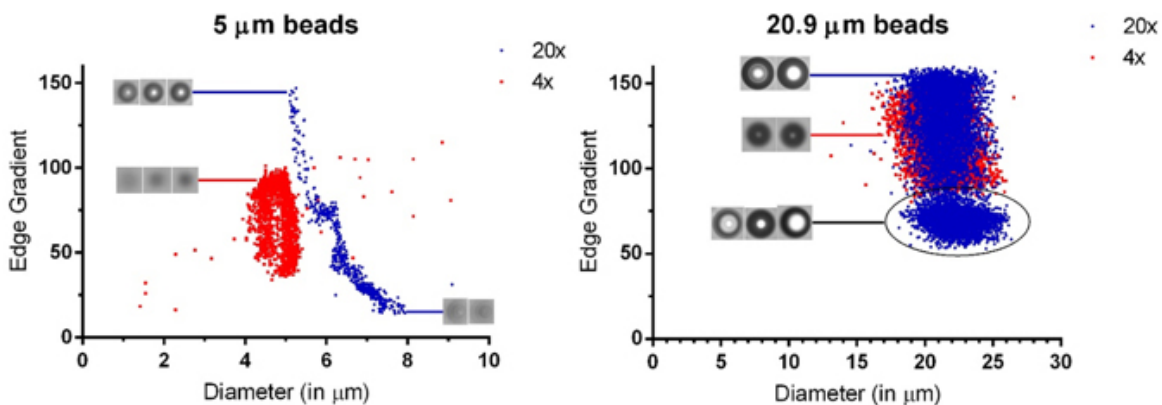
with the lowest (left pairs) medium (middle pairs) and highest (right pairs) edge gradient values. The paired images show on the left the original image of a particle and on the right an image with an edge trace. The edge gradient value provided by VisualSpreadsheet is the average intensity of the pixels making up the outside border of a particle. A low edge gradient number indicates that the edge of the particle is spread out, as that happens with out-of-focus particles, and a very high value indicates a very sharp contrast at the edge of the particle. The results from Figure 1 indicate that the edge gradient value between 100 and 200 corresponds with an ABD value within the range of specifications. Therefore, the edge gradient value was included as one of the criteria for selection of particles for the calculations applied further. Furthermore, the focal plane in the flow cell is ideally positioned in the middle of the depth of field of view, where particles in focus are assumed to have the

Supplementary Figure S1: Area based diameter (ABD) of the three tested polystyrene beads plotted against the corresponding edge gradient value. The color of each open



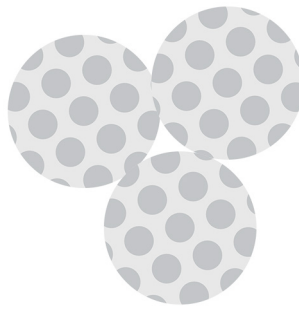
Bead size (μm)	Uncorrected for wall effect		Corrected for wall effect	
	Slope of linear regression	Goodness of fit (R^2)	Slope of linear regression	Goodness of fit (R^2)
30	2206 ± 45	0.9988	2442 ± 49	0.9988
50	1774 ± 73	0.9933	2127 ± 87	0.9934
70	1751 ± 20	0.9996	2253 ± 36	0.9993

Supplementary Figure S2: Average and standard deviation of the measured v/d^2 for different beads in liquids with different densities: 30- μm beads (black circles) 50 μm -beads (blue circles) and 70- μm beads (orange circles). Wall effect correction was (A) not applied, (B) applied for all beads, and (C) applied for 50- and 70- μm beads. In each graph the data points were fitted by linear regression. The slopes and R^2 values of each linear regression are shown in the table. It is seen that the slopes of the linear regression depends on the bead size, despite the use of v/d^2 . When wall correction is applied for the two largest bead sizes, the slopes become similar. Therefore, based on this study we chose to apply wall correction only for the microparticles with the size equal to or higher than 50 μm .



Supplementary Figure S3: Scatter plot showing the relation between edge gradient and area based diameter of 5- μm (left) and 20- μm (right) polystyrene beads (Thermo Scientific, Fremont, CA, USA), with different magnification lenses (i.e., 20x and 4x). The inserts of particle images show a number of representative particles in appointed parts of the scatter plot.

A flow imaging microscopy based method using mass-to-volume ratio to derive the porosity of PLGA microparticles



A.S. Sediq¹, S.K.D. Waasdorp¹, M.R. Nejadnik¹, M.M.C. van Beers^{1,2}, J. Meulenaar², R. Verrijck², W. Jiskoot^{1,*}

¹ Division of Drug Delivery Technology, Cluster Biotherapeutics, Leiden Academic Centre for Drug Research (LACDR), Leiden University, Leiden, the Netherlands

² Dr. Reddy's, IPDO Leiden, the Netherlands.

Abstract

The release of drugs from poly(lactic-co-glycolic acid) (PLGA) microparticles depends to a large extent on the porosity of the particles. Therefore, porosity determination of PLGA microparticles is extremely important during pharmaceutical product development. Currently, mercury intrusion porosimetry (MIP) is widely used despite its disadvantages, such as the need for a large amount of sample (several hundreds of milligrams) and residual toxic waste. Here, we present a method based on estimation of the volume of a known mass (a few milligrams) of particles using Micro-Flow Imaging (MFI) to determine microparticle batch porosity. Factors that are critical for the accuracy of this method (*i.e.*, particle concentration, density of the suspending fluid and post sample rinsing) were identified and measures were taken to minimize potential errors. The validity of the optimized method was confirmed by using non-porous polymethylmethacrylate microparticles. Finally, the method was employed for the analysis of seven different PLGA microparticle batches with various porosities (4.0 – 51.9%) and drug loadings (0 – 38%). Obtained porosity values were in excellent agreement with the MIP derived porosities. Altogether, the developed MFI based method is an excellent tool for deriving the total volume of a known mass of particles and therewith the porosity of PLGA microparticles.

Introduction

Particulate controlled release systems, such as poly(lactic-co-glycolic acid) (PLGA)-based microparticles, are established tools for increasing the therapeutic efficacy of small molecules and peptides by maintaining drug concentrations within target ranges¹. This property also decreases side effects caused by peak concentrations and repeated administrations. The formulation design² as well as the production method³ of drug-containing PLGA microparticles are determinative for the characteristics of the particles and hence their performance. Therefore, it is crucially important to have analytical methods available to measure the characteristics of PLGA microparticles. One of these characteristics is porosity, which is a measure of the volumetric void fraction of the particle. This parameter has been shown to greatly influence the burst release of the drug from PLGA microparticles⁴. Additionally, by enhancing the effective surface area pores can influence the extended release of the drug from the microparticles through several mechanisms⁵.

Several analytical methods exist for determination of the porosity of microparticles, such as mercury intrusion porosimetry (MIP), gas expansion method, scanning electron microscopy (SEM)⁶. MIP is currently one of the most commonly employed methods for porosity determination because of its robustness and ability to provide in-depth porosity information. The popularity of MIP has led to the development of standardized protocols, reference materials and automatized equipment for this method⁷. However, the method has several disadvantages: it requires extensive expertise and model based calculation processes, the use of mercury generates toxic waste, and relatively large amounts (typically hundreds of milligrams) of powder are needed to perform the analysis which especially is a problem in the early stages of formulation and process development. Given the abovementioned disadvantages of MIP, there is a need for an economical, robust and straightforward analytical method for porosity determination.

We hypothesized that flow imaging microscopy could be used for that purpose, because it accurately measures the number and size of microparticles^{8,9}, requires relatively small amounts and does not generate toxic waste. This technique uses imaging of particles in suspension to derive the particle concentration, morphology and size distribution. In the previous chapter, we successfully determined PLGA microparticle porosity by tracking particle sedimentation velocity using a flow imaging microscope. In this study, we developed a new methodology, using flow imaging microscopy, to determine the porosity of PLGA microparticles by sizing and counting all microparticles in a suspension with a known mass of microparticles. This allows for determination of the total volume of the particles and, together with the known mass, one can calculate the density and therewith the porosity. The developed method was used for porosity determination of 7 different PLGA microparticle batches using only a few milligrams of powder.

Materials and Methods

Materials

Cesium chloride (CsCl) and polysorbate 80 were obtained from Sigma (Sigma-Aldrich, Steinheim, Germany). Phosphate buffered saline (PBS; 8.2 g/L NaCl, 3.1 g/L Na₂HPO₄·12H₂O, 0.3 g/L NaH₂PO₄·2H₂O, pH 7.4) was purchased from Braun (B. Braun Melsungen AG, Germany) and filtered with a syringe driven 0.22- μ m polyethersulfone filter unit (Millex GP, Millipore, Carrigtwohill, Ireland). Ultrapure water (18.2 M Ω .cm) was dispensed from a Purelab Ultra water purification system (ELGA LabWater, Marlow, UK). Solutions of PBS containing 0.01% (w/v) polysorbate 80 (PBS-T) were prepared to facilitate wetting of the particles. Dry polymethylmethacrylate polymer beads (PMMA; average size 14.7 \pm 1.3 μ m; non-porous with a density of 1.19 g/mL) were purchased from Polysciences Europe GmbH (Eppelheim, Germany). Seven batches of PLGA microparticles were kindly provided by Dr. Reddy's (IPDO Leiden, the Netherlands). One of these batches contained no active pharmaceutical ingredient (API) and the other six were loaded with different amounts of API. A summary of these batches including their drug loading and porosity information (based on MIP) are shown in Table 1. The residual water and organic solvent contents of each PLGA microparticle batch were lower than 0.5% and not taken into account for the calculations.

Table 1: Properties of the microparticle batches used in this study.

Batch	MIP derived porosity (%)	Drug loading (w/w %)
A	4.0	0
B	13.6	1
C	21.6	11
D	24.4	35
E	26.1	38
F	29.1	33
G	51.9	10

Sample preparation for MFI measurements

For all the samples in individual studies about 1 mg of powder, accurately weighed using a microbalance (Sartorius model SE2, Goettingen, Germany) with a nominal resolution of 0.1 μ g, was used. Immediately after addition of the dry PMMA beads or PLGA microparticles to the suspending fluid (depending on desired concentration) the suspension was homogenized by vortexing. Thereafter, the suspension was sonicated for 20 minutes and left at ambient conditions for at least 24 hours. The suspension was vortexed again prior to the measurement.

Testing influential parameters with PMMA beads

As part of method development multiple factors were tested, namely the density of the suspending fluid, the microparticle concentration and post-sample rinsing during the measurement (explained in detail in the next section). Different concentrations of CsCl were added to PBS-T in order to vary the fluid density. Fluid densities of 1.15 g/mL and 1.27 g/mL were acquired with 0.63 g/mL and 1.25 g/mL CsCl, respectively. PMMA bead concentrations ranging from 0.1 mg/mL to 2.0 mg/mL were used for investigation of the effect of concentration on the accuracy of the method.

MFI measurements

Samples were analyzed by using a Micro Flow Imaging 5200 instrument (MFI; Protein Simple, Santa Clara, CA, USA) with MFI View System Software (MVSS) Version 2. The system was flushed with 3 mL of particle-free suspending fluid at 5 mL/min prior to each measurement. Flow cell cleanness was checked visually. The background was calibrated by performing the 'optimize illumination' procedure using particle-free suspension fluid. The MFI analysis was started without any discarded purge volume prior to the start of fluid imaging. For the study on the effect of concentration and density of the suspension, no post-sample rinsing was applied. The volume of the analyzed suspensions depended on the concentration of the sample, ranging from 0.5 mL to 10 mL. We strived to achieve at least 50,000 particle counts for the sake of statistical power of the measurement.

A 5-mL pipette tip was placed at the sample introduction inlet of the MFI, into which the suspension was poured for analysis. The whole suspension of each sample was analyzed. The MFI measurements that included a post-sample rinsing procedure were accompanied by the following additional steps. Just before the end of the sample measurement, 0.5 mL of particle-free suspending fluid was used to rinse the sample container and was poured over the whole inner surface into the 5-mL pipette tip while continuing to measure with MFI. For the optimization of the MFI analysis (see results section), the potential effect of adsorbed particles at the container, pipette tip and inner tubing surfaces on the porosity calculations was investigated and the required extent of rinsing during the analysis was determined. The number of rinsing steps used to measure the PLGA microparticle batches was chosen based on the results from these optimization studies. No software filters were applied during the runs. After the runs, MFI View Analysis Suite (MVAS) version 1.4 was used to analyze the data recorded by MVSS and to remove stuck, edge and slow moving particles. In a preliminary study a simple filter was developed based on the *Intensity* parameter to exclude all contaminants (such as dust, fibers, etc.) from the analysis. For all samples only particles with a mean intensity value equal to or lower than 300 were included (total intensity range = 0 – 1023; with 0 corresponding to a black pixel and 1023 to a white

pixel). The final size distribution of each sample was extracted, where the particle size was expressed as equivalent circular diameter (ECD), and used for further calculations.

Porosity calculations

Porosity (ϕ) is basically the ratio of the pore volume (V_{pores} in mL) to the total volume of a given (known) amount of suspended particles ($V_{particles}$ in mL) in a certain sample volume. The total particle volume was calculated from the final measured size distribution (size over counts) by MFI. For this purpose each size bin (from 1 μm and larger, with steps of 0.125 μm) was converted into a volume bin, by assuming a spherical shape. Thereafter, the sum of the multiplication of each bin volume with its corresponding total particle count was obtained. $V_{particles}$ consists of the total pore volume (V_{pores} in mL) and the skeletal volume (V_{solids} in mL) or the volume of the solid components in the entire particle population within a given sample volume. Porosity is then calculated based on the following equation:

$$\phi = \frac{V_{pores}}{V_{particles}} \times 100\% = 1 - \frac{V_{solids}}{V_{particles}} \times 100\% \quad \text{Eq. 1}$$

V_{solids} can be calculated from the mass of powder (m) that was used for the suspension and the density (ρ_{solids}) of the solid components:

$$V_{solids} = \frac{m}{\rho_{solids}} \quad \text{Eq. 2}$$

In case of PLGA microparticles the density can be calculated from the drug loading and the reported densities of the PLGA and API accordingly:

$$\rho_{solids} = f_{API} \times \rho_{API} + f_{PLGA} \times \rho_{PLGA} = f_{API} \times \rho_{API} + \rho_{PLGA}(1 - f_{API}) \quad \text{Eq. 3}$$

Here f_{API} (hence drug loading) and f_{PLGA} are the weight fractions of the API and the PLGA, respectively, in the solid content (derived from the drug loading). For the API and PLGA a density of 1.30 g/mL (as stated by the manufacturer of the microparticles) and 1.34 g/mL¹⁰, respectively, were used. By incorporating Eq. 3 into Eq. 2 and subsequently incorporating the resulting equation into Eq. 1, one can derive Eq. 4 to calculate the porosity of PLGA microspheres:

$$\phi = 1 - \frac{m}{(f_{API} \times \rho_{API} + \rho_{PLGA}(1 - f_{API})) \times V_{particles}} \times 100\% \quad \text{Eq. 4}$$

Results

Density of the suspending fluid

To optimize the sample preparation, we have investigated the influence of the density of the suspending fluid on the homogeneity of the PMMA bead suspension (in terms of particle concentration) during measurement. Homogeneity of the suspension is desired in order to minimize locally high particle concentrations that would lead to an increase of non-isolated particles. Non-isolated particles include true aggregates in the raw PMMA material, aggregates formed due to high bead concentration and optically overlapping particles during the measurement, all of which could compromise the accuracy of the method. The PMMA beads were suspended in PBS-T alone and in PBS-T containing two different concentrations of CsCl. For each suspension the total particle volume was measured with MFI. Thereafter, the analyzed particle volume relative to total particle volume at specific time points during the MFI measurement was calculated and the resulting graphs are presented in Figure 1. The error bars show the deviation caused by the size distribution of particles at different time points. Note that the size distribution becomes wider with the presence or increase in number of non-isolated particles. These graphics show in rough terms how changes in the density of the suspending fluid would influence the particle homogeneity in the sample liquid. All three graphs show low particle counts at 0 min due to initial dilution of the sample with the preceding particle-free suspending fluid used for the 'optimize illumination' step. At about 1 min, particle counts appeared to stabilize and all three graphs present a plateau stage. Suspending fluid containing no CsCl showed a slightly descending plateau stage, up to 3 minutes of measurement (Fig. 1A). Thereafter, the particle count decreased much faster. The standard deviation in the particle volume decreased at later stages of the plateau phase and thereafter. This indicates that percentage of non-isolated particles was not constant throughout the entire measurement. On the contrary, the suspending fluid with 0.63 g/mL CsCl having a density of 1.15 g/mL showed a much longer and more stable plateau stage (Fig. 1B). Here, the particle count started decreasing only after 4.5 min. During this measurement the standard deviation was relatively constant over a larger part of the plateau stage, indicating a constant percentage of non-isolated particles. Further increase of the fluid density to 1.27 g/mL (1.25 g/mL CsCl) resulted in relatively lower counts (Fig. 1C) during the first 3 minutes of the measurement compared to the other two suspensions. Thereafter, a progressive increase in analyzed particle volume was observed. A slight increase in the standard deviation of the particle volume was observed by the end of the measurement, indicating that the percentage of non-isolated particles increased towards the end of the measurement.

Observations seen in this set of experiments indicate that a homogeneous particle concentration over the entire (or large part of) MFI measurement can be achieved using a

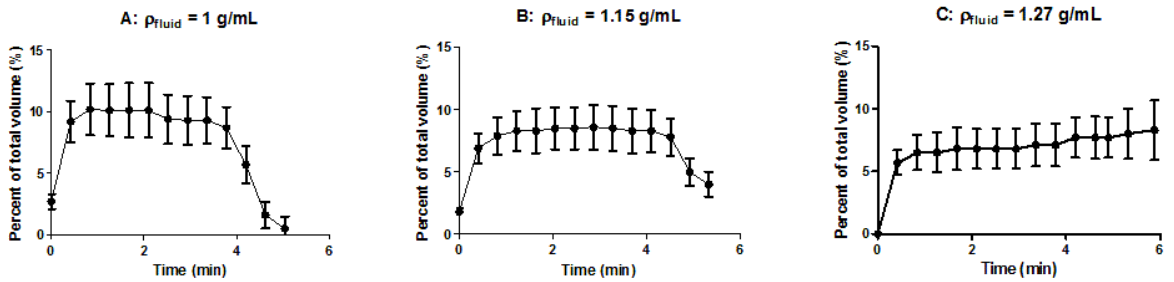


Figure 1: Percentage of the total particle volume over the measured time in samples of 0.3 mg/mL PMMA beads in different suspending fluids: A) PBS and 0.01% polysorbate 80 (density 1.03 g/mL); B) PBS, 0.01% polysorbate 80 and 0.63 g/mL CsCl (density 1.15 g/mL); and C) PBS, 0.01% polysorbate 80 and 1.25 g/mL CsCl (density 1.27 g/mL).

fluid density that matches the particle density. In our study we found a fluid density of 1.15 g/mL to be the best choice with respect to homogeneity during the measurement of PMMA beads and therefore used this as suspending liquid in following studies. In this suspending liquid the density difference between the particles and the fluid was about 3% (relative to the PMMA density).

Effect of particle concentration

During the second part of the study on influential factor, we focused on the particle concentration. Increasing particle concentration would theoretically result in increasing numbers of detected non-isolated, due to optically overlapping particles during the measurement. These non-isolated particles mostly do not have a spherical shape and therefore it is expected that the accuracy in total particle volume calculation would decrease with increasing number and volume of non-isolated particles. For this part, increasing concentrations of PMMA beads were prepared in duplicates using the suspending fluid with the density of 1.15 g/mL. After MFI measurement, the percentage of non-isolated particles (volume and number based) was calculated.

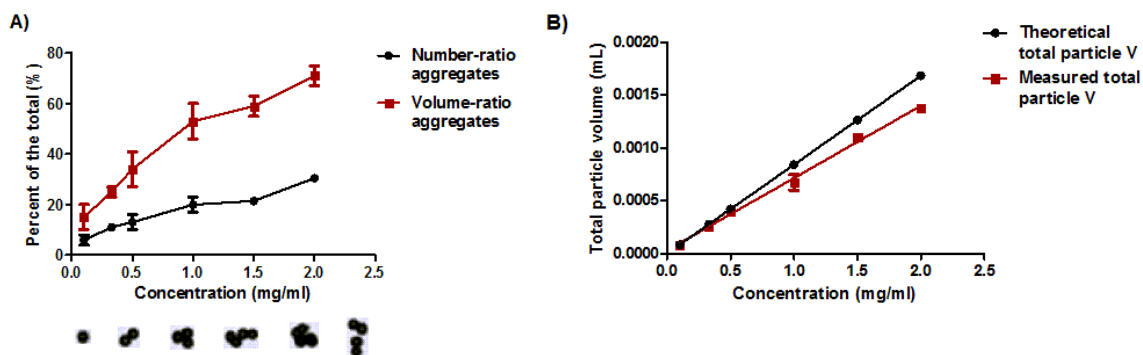


Figure 2: The effect of PMMA bead concentration on the accuracy of total particle volume calculation. A: Contribution of non-isolated (sum of aggregated and optically overlapping) particles to the total particle counts (black circles) and total particle volume (red squares) in suspensions with different PMMA concentration, as measured with MFI. Each data point shows the average and the upper and lower value of the duplicate measurement of suspensions. Examples of MFI images of a single and a few different non-isolated particles are displayed below the graph. B: Total particle volume of each sample displayed in graph A as function of particle concentration. The theoretical values derived from the sample concentration and known PMMA density (black circles) and measured total particle volumes with MFI (red squares) are compared.

Figure 2A shows that an increasing bead concentration resulted in more non-isolated particles, as expected. This in turn led to an increase in the number and volume of the non-isolated particles relative to the total counts and total particle volume, respectively. At the highest bead concentration tested (2 mg/ml) almost 70% of the total particle volume belongs to non-isolated particles. Using the density of the PMMA particles and the PMMA sample concentrations, the total particle volume per sample ($V_{\text{particles}}$) was calculated. In Figure 2B these theoretical values are compared with the experimentally determined total particle volume for each tested sample. It is seen that the measured particle volume started to significantly underestimate $V_{\text{particles}}$ at PMMA concentrations of 1 mg/mL and higher. For each following study with the PMMA beads a concentration of 0.1 mg/mL was used.

Post-sample rinsing during MFI measurement

The last potentially influential factor that was studied concerned the measurement procedure. Here an attempt was made to minimize loss of sample, which would lead to erroneous total particle volume measurements. Loss of sample could be due to adsorption of particles (and liquid containing particles) to the container, pipette tip and instrument tubing. After the entire suspension of 0.1 mg/mL PMMA beads was measured (after 22 minutes), 5 post-sample rinsing steps of 0.5 mL each were applied, as described in the

Methods section. As seen from the results in Figure 3A, over the whole measurement including the rinsing steps PMMA beads of about 15 μm were detected.

Although fewer particles were detected when the rinsing fluid passed through the flow cell and was being measured (see drop in particle volume after 22 minutes), still substantial amounts of particles were included in the measurement when rinsing was applied. Figure 3B shows that less than 80% of the total particle volume found in suspension had passed the camera view at the moment when the first 0.5 mL of rinsing fluid was added. Only after 3 rinsing steps were applied, almost all particles found in the suspension had passed the camera view.

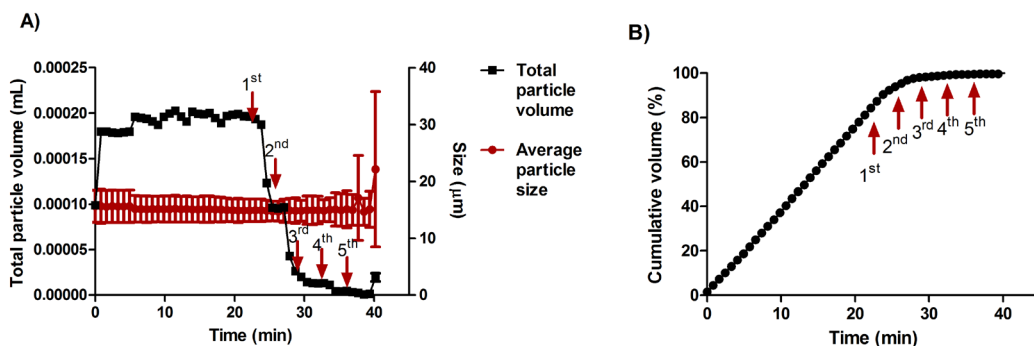


Figure 3: The effect of post-sample rinsing steps during the MFI measurement on analysis of adsorbed particles (and liquid containing particles) to the tubing and pipette tip. A: Particle size (mean and standard deviation; red circles) and total particle volume (mean and standard deviation; black squares) at different time points. The latter is achieved through multiplication of the particle count and single particle volume at given time points. Single particle volume is calculated from the average particle size and formula for volume of a sphere. B: Cumulative particle volume at different time points during the measurement expressed in percent, with 100% being the total particle volume measured in the experiment. The red arrows indicate the time points at which 0.5 mL of particle free suspending fluid was used to rinse the tubing, pipette tip and subsequently measured by MFI, as described in *Methods* section.

Therefore, for the following studies we have applied 3 post-sample rinsing steps with 0.5 mL of the particle free suspension in order to measure the particles adsorbed to the tubing and pipette tip.

Porosity measurements of PMMA beads (method validation)

For the validation of the presented method for porosity determination we used PMMA beads. Based on the previous experiments, the following conditions were used: the beads were suspended at a PMMA concentration of 0.1 mg/mL in a suspending fluid of PBS-T with 0.63 g/mL CsCl (and a density of 1.15 g/mL), the sample volume was 5 mL, and 3 0.5-mL

post-sample rinsing steps were applied.

The measurements resulted in a measured density of 1.17 ± 0.03 g/mL and a derived porosity of $2 \pm 2\%$ for the studied PMMA beads. These values are in excellent agreement with the given information by the manufacturer (density of 1.19 g/mL, 0% porosity).

Porosity measurements of PLGA microparticles (method application)

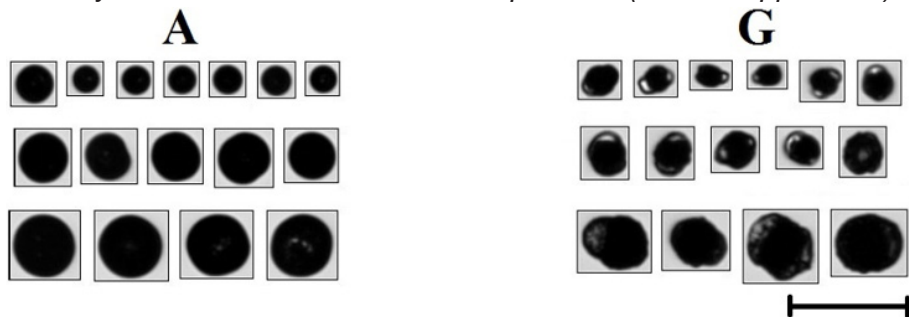


Figure 4: Examples of MFI pictures of individual particles in batch A and G of the studied PLGA microparticles. Batches B-F had particles looking similar to the ones from batch A. The scale bar at the right bottom depicts 100 μm .

The developed method was applied for determination of the porosity of 7 different batches of PLGA microparticles. Based on the MIP measurements these batches differed in porosity (see Table 1). For each PLGA microparticle batch the particle concentration was optimized according to the previous section. Briefly, the optimal concentration was chosen such that the percentage of non-isolated particles was lowest. In order to keep the measurement duration not more than 40 minutes per sample the suspension volume was limited to 5 mL. The optimal fluid density was based on the expected density of each PLGA microparticle batch when suspended in the liquid (calculated from the loading and porosity value derived with MIP). Given the almost similar density of the API and the PLGA raw material, for all the suspensions the same fluid density was used. The chosen fluid density differed less than 3% from each (expected) PLGA microparticle density. A summary of these suspension conditions and measured average and standard deviation of the particle sizes are given in Table 2. All the batches contained predominantly spherical particles, except for batch G, which showed more unevenly shaped particles (Figure 4). In Figure 5, the average and standard deviation of the calculated porosity ($n = 3$) values are plotted against the values obtained by MIP, illustrating that the results from the developed flow imaging microscopy based method are in excellent agreement with the ones found by MIP. The line shows the linear regression (goodness of fit: $R^2 = 0.9854$), with the dashed lines representing the 95% confidence interval (CI) range. The 95% CI range of the slope was 1.006 – 1.334, which indicates high similarity between the MFI derived and MIP derived porosity.

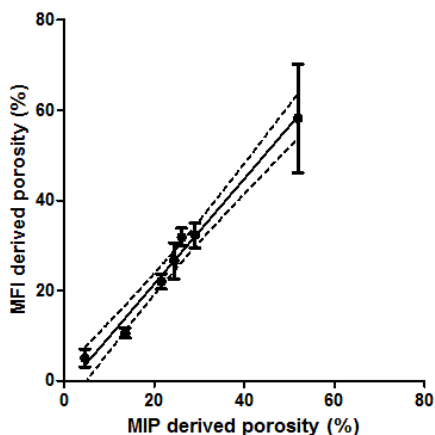


Figure 5: Porosity results gained from the MFI measurements against MIP derived porosity values for seven different PLGA microsphere batches. For each batch the mean and standard deviation of three measured samples are shown. The linear relation between MIP and flow imaging microscopy porosity is denoted as the solid line, with the 95% confidence of interval of the linear relation between the dashed lines.

Table 2: Summary of the conditions used for the studies with the 7 PLGA microsphere batches and the size and morphological parameters obtained by MFI.

Batch	Suspending fluid density used (g/mL)	Concentration used (mg/mL)	Average \pm standard deviation of particle size (μm)	Intensity (mean \pm standard deviation; a.u.)	Circularity (mean \pm standard deviation)	Aspect ratio (mean \pm standard deviation)
A	1.3	0.2	44.1 \pm 12.5	188 \pm 266	0.90 \pm 0.11	0.95 \pm 0.12
B	1.3	0.2	46.1 \pm 12.6	191 \pm 268	0.89 \pm 0.10	0.94 \pm 0.10
C	1.3	0.3	42.9 \pm 11.9	200 \pm 269	0.89 \pm 0.11	0.95 \pm 0.15
D	1.3	0.3	43.4 \pm 11.6	197 \pm 268	0.88 \pm 0.10	0.93 \pm 0.11
E	1.3	0.2	48.7 \pm 14.9	186 \pm 265	0.88 \pm 0.10	0.92 \pm 0.11
F	1.3	0.2	46.1 \pm 13.4	193 \pm 265	0.87 \pm 0.15	0.92 \pm 0.10
G	1.3	0.2	48.9 \pm 14.4	215 \pm 260	0.88 \pm 0.18	0.81 \pm 0.19*

*Significantly different from the other batch(es) (one-way Anova ($p < 0.0001$) followed by post-hoc Tukey's multiple comparison test ($p < 0.05$))

Discussion

The porosity of PLGA microspheres has been recognized as an important parameter for the release kinetics of the encapsulated drug^{4,11}. Currently, MIP is the most employed method for porosity measurements. Considering the limitations of the MIP method, there is a need for a more straightforward method. In this investigation we have developed a flow imaging microscopy based method using PMMA microsphere beads and applied the developed method for porosity determination of a number of PLGA microsphere batches. Our method depends on the precision and accuracy of two parameters that are included in the calculations, namely the mass of the particles used for the suspension preparation and the total particle volume as measured by MFI. The error in the weighing was minimized by the use of a microbalance for the masses of about 1 mg used for our measurements (translating into a theoretical weighing error of about 0.01%). However, other factors related to sample preparation and measurement also contribute to the overall error in the measurement and determination of the total particle volume.

The calculation of particle volume is based on the size distribution of the sample. For high

accuracy of the latter parameter, a flow imaging microscopy technique with high sizing and counting accuracy is essential. The sizing accuracy of MFI was shown to be high for small polystyrene beads (2 – 10 μm)¹². In a separate study we found that the sizing accuracy larger (30 – 70 μm) NIST-traceable polystyrene beads was also high (see Supplementary Table 1). Zölls and coworkers found high counting accuracy, which was suggested to be a result of high sample efficiency of the MFI 5200 system (about 85%)¹². The counting accuracy depends on the concentration and size of particles in the measured sample. Therefore, the manufacturer of the MFI provides concentration limitations for different particle sizes up to 10 μm , with respect to the counting accuracy of the system, with a recommended maximum concentration of 20,000 10- μm particles per mL¹³. In our study we have shown that this recommendation is also valid when total particle volume determination is the ultimate goal of a measurement. We found that the total particle volume calculation (from the average particle size and concentration) was accurate up to a (15- μm sized) PMMA bead concentration of 0.5 mg/mL, which corresponds to about 24,000 particles per mL.

One caveat with respect to volume determination of microparticles is that any significant swelling of the particles would lead to overestimation of the original size and total particle volume, which would consequently result in underestimation of the porosity. However, it has been shown that, for PLGA particles, detectable swelling appears at the later stages of the degradation, that is after several days when the molecular weight of the PLGA matrix gets lower than 20 kDa¹⁴. Including studies on optimizing the condition and replicate measurements the achievement of porosity value as presented in our investigation does not cost more than a couple of hours.

MFI derives the size of a particle from the measured particle area, by calculating the diameter of a circle with an equivalent projected surface area. In case of PLGA microparticles the nearly spherical shape reduces the chance of inaccurate sizing. However, optically overlapping particles and aggregates (possessing mostly non-spherical shapes) are more subjected to inaccurate sizing. The amount of non-isolated particles detected in the suspension was found to mainly depend on the particle concentration. More particles per volume unit of the liquid obviously lead to a higher chance that multiple particles would coincidentally overlap in the field of view. In some cases particles that are too close to each other in the field of view (but still obviously physically separated), are erroneously detected as one agglomerate (*e.g.*, see rightmost particle image in Figure 2). Probably this is caused by a combination of light diffraction from two particles close to each other and a very sensitive detection threshold used by the MFI software. This threshold together with the so-called minimum distance-to-the-neighbor setting in MFI (by default 3 μm), results in detection of the pixels between these particles as part of the agglomerated particle¹³. Naturally, the detected non-isolated particles may also be real aggregates, meaning that

the microparticles are physically bound to each other.

Measures can be taken to reduce the chances of optically occluded particles and presence of real particle aggregates in the PLGA microparticle batches. For the latter surfactants present in the suspending agent, vortexing steps and sonication should in principle reduce physical aggregation. For PLGA microparticles it is well known that the tendency of microparticles to aggregate on drying is related to the extent of the particle hydration and the residual ethyl acetate in wet microparticles¹⁵. According to the manufacturer, the residual solvent content in the different batches of the microparticles were measured to be of insignificant value (below 0.1%).

Reduction of the particle concentration in order to reduce the chance of overlapping particles in the field of view has its limitations. Namely that a very large volume of suspension must be measured to make sure that a high number of particles is counted. Therefore, it is necessary to define a threshold for the amount of non-isolated particles (relative to the total) that still delivers accurate particle volume determination. The threshold for this amount of non-isolated particles we had set at 30%. This threshold was based on our study with the PMMA beads, where even up to 30% (volume-based) non-isolated particles accurate total particle volumes were achieved (see Figure 2B). At the end the volume percentage of non-isolated particles for the studies with PLGA microparticle was not more than 12%.

These theoretical facts combined with our observations, brings us to the conclusion that, in order to reduce the error introduced by the non-isolated particles, low microparticle concentrations should be used for the MFI measurements. One should keep in mind that very low concentrations would require analysis of large suspension volumes to detect a sufficiently large number of particles (in this study the choice was detection of at least 50,000 particles in total) for the statistical power of the analysis. Analysis of large volumes would require tremendously prolonged measurement times. Therefore, finding a compromise between particle concentration, statistical power and measurement time is necessary for individual batches to be measured. In our study, typical analysis times per sample were between 20 – 40 minutes.

Decreasing the concentration of a microparticle batch with a broad size distribution cannot fully assure that coincidental particle overlap in the field of view will not occur. This has to do with the sedimentation of particles during the measurements. Particulate sedimentation in a fluid depends mainly on the size of the particle and the density difference between the particle and the fluid¹⁶. In case of a sample containing a broad size distribution (*e.g.*, PLGA microparticles), a big density gap between the particles and the suspending fluid will lead to rather fast settling particles. Since larger particles will settle faster, this can create locally high concentrations of (in particular large) particles. Decreasing the density difference between the particle and the fluid is an effective way to avoid this phenomenon. Cesium

chloride is known to be an inert salt and has the great advantage of being able to change the density of aqueous solutions with very limited change in the viscosity¹⁷, and therefore a good choice to be used for adjusting the fluid density.

Our results presented in Figure 1 clearly indicate that the bigger the difference between the density of the particle and the suspending liquid, the higher the chance of sample heterogeneity. This heterogeneity caused by settling/floating of particles during measurement, would hypothetically result into locally high numbers of non-isolated particles. We have proven this hypothesis for the condition where we had the largest gap in density between particle and the suspending liquid, *i.e.*, for the PMMA microparticle beads suspended in a CsCl free solution with a density of 1 g/mL. The low counts at start are caused by dilution with particle free liquid that was used to perform the 'optimize illumination' step and the low counts in the last part of the measurement are caused by creation of locally decreased particle concentration due to settling of particles earlier during the measurement. We have calculated the volume percentage of non-isolated particles at each time point, excluding the first and last minutes of the run where the low number of particles compared to the rest of the run could result in unreliability in calculation of the percentage of aggregates. The data in the Supplementary Figure S1 indicates that the percentage of non-isolated particles resembled a parabolic shape over the course of MFI analysis. This confirms the above-mentioned hypothesis that the settling of particle during the experiment can cause a locally high concentration of non-isolated particles (*i.e.* the peak of the parabola). Consequently this could lead to larger errors in estimation of the total volume of the particles.

Both the suspending medium and the PMMA particles may interact not only with the container, but also with the pipette tip on top of the MFI inlet port and the MFI tubing. This is also evident from the results in Figure 3A, where the first part of the measurement has a lower total particle volume than the rest of the measurement until post-rinsing steps. This could be overcome by a post-sample rinsing step with particle free suspending medium: the expected porosity (0% for control PMMA particles) was reached after 3 rinsing steps were included in the measurement. The tendency of suspending medium and suspended particles to interact with the tip and tubing materials will determine these rinsing conditions. Despite the attempts presented here, it appears to be difficult to have a homogenous suspension throughout the whole measurement. Also the loss of particles due to interaction with the tip and tubes would jeopardize the accuracy of the method even when fluid density is adjusted and a rather long-term homogeneity during the measurement is attained. Therefore, the presented method cannot be further simplified by calculating the particle volume (per volume of suspension) from a specific fraction of a MFI measurement; rather, it is advised to measure the entire sample and include post-sample rinsing steps to ensure measurement of all the particles within that sample.

After validation of the method with PMMA beads, we were able to find fairly similar porosities for 7 batches of PLGA microparticles compared to MIP derived ones. That is seen from the average slope of the linear regression that had a value of 1.17 ± 0.06 . Our investigation shows also that the method can be applied for a considerably wide range of porosities. For the batch with the highest MIP derived porosity (batch G), we found a relatively large standard deviation of the measured particle porosity. The reason for this is likely the non-spherical shape of the particles, resulting in irreproducible sizing and hence total particle volume determination. The latter is also obvious from the aspect ratio value, which is lower for batch G compared to all the other PLGA microparticle batches (see Table 2).

Overall, the method we propose in this study is very applicable as a tool to assess the porosity of microparticles. In addition, the instrument delivers particle size distribution of the batch and images of the particles as well as several morphological parameters. For the porosity determinations certain preparatory studies, as we described here, need to be performed in order to achieve accurate measurements.

Conclusion

In this study, we have investigated a novel method for the porosity determination of microparticles based on measurement using MFI. We have shown that optimization of the particle concentration, suspending fluid density and post-sample rinsing steps during measurement are advisable for obtaining the most reliable porosity outcome. The described method allowed for successful measurement of the porosity of (spherical) PMMA beads and 7 different PLGA microparticle batches. The method requires only a few milligrams of the particle powder, which is an asset for early stage formulation and process development operations.

References

1. Ma G 2014. Microencapsulation of protein drugs for drug delivery: strategy, preparation, and applications. *J Control Release* 193:324-340.
2. Makadia HK, Siegel SJ 2012. Poly Lactic-co-Glycolic Acid (PLGA) as Biodegradable Controlled Drug Delivery Carrier. *Polymers* 3(3): 1377-1397.
3. Ramazani F, Chen W, van Nostrum CF, Storm G, Kiessling F, Lammers T, Hennink WE, Kok RJ 2016. Strategies for encapsulation of small hydrophilic and amphiphilic drugs in PLGA microspheres: State-of-the-art and challenges. *International journal of pharmaceutics* 499(1-2):358-367.
4. Mao SR, Xu J, Cai CF, Germershaus O, Schaper A, Kissel T 2007. Effect of WOW process parameters on morphology and burst release of FITC-dextran loaded PLGA microspheres. *International journal of pharmaceutics* 334(1-2):137-148.

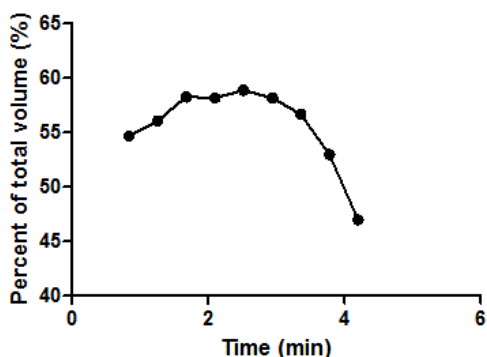
- 5.** Klose D, Siepmann F, Elkharraz K, Krenzlin S, Siepmann J 2006. How porosity and size affect the drug release mechanisms from PLGA-based microparticles. *International journal of pharmaceutics* 314(2):198-206.
- 6.** Qiu J, Khalloufi S, Martynenko A, Van Dalen G, Schutyser M, Almeida-Rivera C 2015. Porosity, Bulk Density, and Volume Reduction During Drying: Review of Measurement Methods and Coefficient Determinations. *Dry Technol* 33(14):1681-1699.
- 7.** Webb PA. 2001. *An Introduction To The Physical Characterization of Materials by Mercury Intrusion Porosimetry with Emphasis On Reduction And Presentation of Experimental Data.* ed., Norcross, Georgia: Micrometrics Instrument Corp. p 23.
- 8.** Corvari V, Narhi LO, Spitznagel TM, Afonina N, Cao S, Cash P, Cecchini I, DeFelippis MR, Garidel P, Herre A, Koulov AV, Lubiniecki T, Mahler HC, Mangiagalli P, Nesta D, Perez-Ramirez B, Polozova A, Rossi M, Schmidt R, Simler R, Singh S, Weiskopf A, Wuchner K 2015. Subvisible (2-100 µm) particle analysis during biotherapeutic drug product development: Part 2, experience with the application of subvisible particle analysis. *Biologicals* 43(6):457-473.
- 9.** Narhi LO, Corvari V, Ripple DC, Afonina N, Cecchini I, Defelippis MR, Garidel P, Herre A, Koulov AV, Lubiniecki T, Mahler HC, Mangiagalli P, Nesta D, Perez-Ramirez B, Polozova A, Rossi M, Schmidt R, Simler R, Singh S, Spitznagel TM, Weiskopf A, Wuchner K 2015. Subvisible (2-100 µm) Particle Analysis During Biotherapeutic Drug Product Development: Part 1, Considerations and Strategy. *Journal of pharmaceutical sciences* 104(6):1899-1908.
- 10.** Arnold MM, Gorman EM, Schieber LJ, Munson EJ, Berkland C 2007. NanoCipro encapsulation in monodisperse large porous PLGA microparticles. *J Control Release* 121(1-2):100-109.
- 11.** Schnieders J, Gbureck U, Vorndran E, Schossig M, Kissel T 2011. The effect of porosity on drug release kinetics from vancomycin microsphere/calcium phosphate cement composites. *J Biomed Mater Res B Appl Biomater* 99(2):391-398.
- 12.** Zolls S, Weinbuch D, Wiggenghorn M, Winter G, Friess W, Jiskoot W, Hawe A 2013. Flow imaging microscopy for protein particle analysis--a comparative evaluation of four different analytical instruments. *The AAPS journal* 15(4):1200-1211.
- 13.** ProteinSimple. 2011. *User Manual: Micro-Flow Imaging.* ed.
- 14.** Gasmi H, Danede F, Siepmann J, Siepmann F 2015. Does PLGA microparticle swelling control drug release? New insight based on single particle swelling studies. *J Control Release* 213:120-127.
- 15.** Sah H 1997. Microencapsulation techniques using ethyl acetate as a dispersed solvent: Effects of its extraction rate on the characteristics of PLGA microspheres. *J Control Release* 47(3):233-245.
- 16.** Batchelor GK. 1967. *An introduction to fluid dynamics.* ed., Cambridge,: U.P. p xviii, 615 p.
- 17.** Lyons PA, Riley JF 1954. Diffusion Coefficients for Aqueous Solutions of Calcium Chloride and Cesium Chloride at 25-Degrees. *J Am Chem Soc* 76(20):5216-5220.

Supplementary Information

The sizing accuracy of MFI was tested for bead larger than 10 μm . Therefore, 3 NIST-traceable polystyrene beads were used of different sizes (mean \pm standard deviation), namely $29.8 \pm 0.4 \mu\text{m}$; $50.2 \pm 0.5 \mu\text{m}$; $69.1 \pm 0.8 \mu\text{m}$. The results are shown in **Supplementary Table 1**. The measured values for each bead size were compared with the size provided by the manufacturer (using a paired t-test). All MFI derived sizes were shown to be statistically similar ($p > 0.05$) to the manufacturer's specifications.

Supplementary Table 1: Sizing accuracy of polystyrene standards with MFI.

Declared size by the manufacturer (μm)	MFI derived size (μm)	P value
29.8 ± 0.4	29.7 ± 0.1	< 0.0001
50.2 ± 0.5	50.1 ± 0.1	< 0.0001
69.1 ± 0.8	69.0 ± 0.2	0.0001



Supplementary Figure 1: Percent of non-isolated particles (based on volume) detected at each time point of the measurement presented in Figure 1A of the main document.

A label-free method for cell counting and viability determination using flow imaging microscopy



A.S. Sediq¹, R. Klem¹, M.R. Nejadnik¹, P. Meij², W. Jiskoot^{1,*}

¹ Division of Drug Delivery Technology, Cluster BioTherapeutics, Leiden Academic Centre for Drug Research (LACDR), Leiden University, Leiden, The Netherlands

² Department of Clinical Pharmacy and Toxicology, Leiden University Medical Center, Leiden, The Netherlands

Abstract

Two quality attributes of cell therapy products are cell concentration and percentage of viable cells. Despite the availability of techniques to determine cell concentration and viability, there is a need for label-free, robust and user-friendly techniques. In this study we have investigated the potential of two flow imaging microscopy (FIM) techniques (Micro-Flow Imaging (MFI) and FlowCAM) to determine cell concentration and viability. For this goal we have exposed B-lineage acute lymphoblastic leukemia (B-ALL) cells of 2 different donors to ambient conditions, in order to induce cell death. Samples were taken at different days and measured with MFI, FlowCAM, hemocytometry and automated cell counting. Dead and live cells from fresh B-ALL cell suspension were fractionated by flow cytometry in order to derive filters based on morphological parameters of separate cell populations with MFI and FlowCAM. The filter sets were used to assess the concentration of viable cells in the measured samples. All techniques gave fairly similar cell concentration values over the whole incubation period. However, MFI showed to be superior with respect to precision. Both FIM methods were able to provide similar results for viability as the conventional methods (hemocytometry and automated cell counting). Altogether, our investigation shows that FIM-based methods may be advantageous over conventional methods, as FIM measures much larger sample volumes, does not require labeling, is less laborious and provides images of individual cells. The latter asset we have successfully used to determine viability, but can potentially be employed to distinguish early stages of cell death and different cell types in a heterogeneous cell sample.

Introduction

Cell therapy products (CTPs) are receiving increasing attention by the pharmaceutical industry because of their demonstrated potential for use in treatment of a variety of diseases, such as cancers, viral infections, and autoimmune disorders^{1,2}. The quality of CTPs relies, among others, on the viability of the cells. During production, cells used for cell therapy may undergo different process steps, such as harvesting, purification, genetic manipulation, expansion, freezing and thawing³. These procedures, as well as other treatments, such as transport⁴ and storage in infusion medium/solution⁵, and even the administration to the patient⁶, can induce different types of stresses to the cells and potentially affect cell viability. While there are some regulations on what properties of CTPs should be tested⁷, quick testing of viability prior to administration to the patient is often neglected. As a result, changes in product quality that might occur between production and administration could remain undetected.

Two main techniques that are frequently applied to assess cell viability are hemocytometry⁸ and flow cytometry⁹. The determination of cell viability with a hemocytometer is based on staining of the dead cells using dyes like eosin and trypan blue⁸. In a flow cytometer a laser beam is focused on a flowing liquid. Individual cells in the flow scatter the laser light and are detected by the system. The type, size and other characteristics of the cells determines the degree of the scattering. The forward scatter (FSC) and side scatter (SSC) provide information about cell size and granularity, respectively. Granularity level has been shown to be inversely related with cell viability¹⁰. Intrinsic fluorescence of the cells and/or fluorescence from a fluorescent label can also be detected¹¹. Moreover, the use of fluorescently labeled antibodies directed against cell surface markers can aid in the evaluation of cell type and viability. Flow cytometry is known to be a very accurate and reproducible technique for cell viability tests. However, absolute cell concentrations are usually not easily obtained. In addition, the preparation and labeling of the cells can be time-consuming and expensive.

Hemocytometry is the currently the gold standard in the clinical practice for cell counting and viability determination. Whilst being a fast method, the method can be laborious and has certain weak points that could potentially harm the accuracy of the method. For example, the pipetting of the cell suspension and fitting the cover glass may disrupt the sample homogeneity at the cytometer surface. In addition, the method uses only a few microliters of the suspension for the actual counting of the (viable and non-viable) cells and extrapolates this number to a concentration unit of cells per milliliter. With respect to the quantity of cell suspension measured and the laborious nature of the method, automated cell counters provide improvement, especially for routine measurements, as they measure about 4x as much volume as a hemocytometer (0.4 vs. 0.1 μL). However, one should be

aware that non-cellular particles in the sample could be counted as a cell as well.

In this regard, less laborious, inexpensive techniques that allow for rapid and reliable counting of CTPs would be extremely beneficial for improving the success of CTPs in clinical practice. Emerging flow imaging microscopy (FIM) techniques may fulfill these needs. In these systems the sample flows through a flow cell where images are taken with a high-magnification digital camera. With the help of the dedicated instrument software, the quantity and several morphological parameters of the particles can be extracted from the images¹². FIM can give valuable information about cells, without the need for labeling, and detect small changes in cell size and morphology which have been shown to be related to cell viability^{13,14}. In addition, FIM techniques are generally easy and fast to perform.

One of these FIM techniques is Micro-Flow Imaging, which owes its popularity in this field mainly to its user-friendliness and robust operation. The application of MFI for cells is limited but not unexplored. For instance, Martin et al. have used MFI to study aggregation tendency of thawed hematopoietic stem cells¹⁵. A recent study of Farrell and coworkers used MFI to determine cell coverage and confluency on microcarriers used in culture-derived bioreactors¹⁶. Besides MFI, FlowCAM has been explored for its potential in biologic drug product development¹⁷⁻¹⁹ and drug delivery systems (*Chapter 4*).

The aim of this study was to evaluate the performance of two FIM techniques, *i.e.*, Micro-Flow Imaging (MFI) and FlowCAM, in their ability to determine cell viability. Even though the devices are based on the same measurement principle, they differ in several aspects. The FlowCAM has a higher resolution and provides more particle parameters, whereas the MFI tends to provide a more accurate determination of particle concentration^{19,20}. In the presented study, the two systems are used for the characterization of two cell lines and compared with hemocytometry and automated cell counting as well as with each other.

Materials and methods

Cell materials

B-lineage acute lymphoblastic leukemia (B-ALL) cells were used as model cells in this study. The cells were cultured from two different donors (ALL-CR and ALL-CM²¹; further referred to as cell line 1 and cell line 2) and provided by the Department of Hematology, Leiden University (LUMC, Leiden, the Netherlands). Cells were frozen in 60% v/v wash medium (BioWhittaker® Iscove's Modified Dulbecco's Medium (IMDM) 98.5% v/v, penicillin/streptomycin (Lonza) 1% v/v, HSA-20% 0.5% v/v) and a final concentration of 10% v/v HSA-20%, 10% v/v DMSO (LUMC, Leiden, the Netherlands) at a concentration of about $1 \cdot 10^7$ cells/mL and stored at -80°C until the start of incubation experiments. After controlled thawing, washing and counting, cells were suspended in NaCl 0.9% m/v + HSA-20% 2% v/v at a concentration of 10^6 cells/mL and were exposed to the stress condition described

below.

Stress condition

The chosen stress condition in which the cells showed a clear decrease in, but not a total loss of viability, was incubation at ambient temperature for up to 8 days. The cell concentration and morphological parameters of each sample were analyzed at different days by using MFI and FlowCAM. For cell line 1 the measurements were performed at day 0, 1, 2, 4, 6 and 8. The study performed with the 2nd cell line served as a confirmative study and therefore the measurements at day 4 and 6 were not performed. In parallel, the cell concentration and number of viable cells in the same samples were determined with a hemocytometer and an automated cell counter. For the data analysis of both flow imaging microscopy techniques we only included particles detectable with the hemocytometer and the automated cell counter, *i.e.*, particles $\geq 4 \mu\text{m}$.

Hemocytometry

Cell suspensions were diluted twofold with a trypan blue solution (0.4% (w/v) in 0.81% NaCl and 0.06% K_2HPO_4 (Bio-Rad, Hercules, California, USA)). Ten μL of the mixture was placed on a Bright-Line hemocytometer glass (Sigma-Aldrich, Steinheim, Germany), and analyzed by using a light microscope (Zeiss AxioStar Plus, Carl Zeiss Light Microscopy, Göttingen, Germany). Both viable (not stained) and non-viable (stained) cells were counted in 25 frames of the hemocytometer according to the manufacturer's recommendations and the percentage of viable cells to the total was calculated²². For each sample triplicate measurements were conducted.

Automated cell counting

Ten μL of the mixture prepared for the hemocytometry was introduced into the counting slide. Subsequently, the cell concentration and percentage of viable cells were measured by using a Bio-Rad TC20 Automated Cell Counter (Bio Rad, Hercules, California, USA). This procedure was repeated three times for each sample.

Micro-Flow Imaging (MFI)

In order to decrease the concentration of the cells and reduce the chance of detection of overlapping particles, samples were first diluted 4-fold with the particle free NaCl 0.9% m/v + HSA-20% 2% v/v . The diluted samples were analyzed by using a Micro Flow Imaging 5200 (Protein Simple, Santa Clara, CA, USA), with MFI View System Software (MVSS) Version 2. No filters were applied during the runs. The 100 μm silane coated flow cell was rinsed with flow of ultrapure water (18.2 $\text{M}\Omega\cdot\text{cm}$; dispensed by using a Purelab Ultra

water purification system (ELGA LabWater, Marlow, UK) and thereafter a background measurement was taken with particle free NaCl 0.9% m/v + HSA-20% 2% v/v. For the analysis, 0.50 ml of each sample was run at a flow rate of 0.17 mL/min. The data analysis was performed with MFI View Analysis.

Table 1: Morphological parameters used in this study and their descriptions as provided by MVAS (MFI) and Visual SpreadSheet (FlowCAM).

Parameter	Unit	Description
Micro-Flow Imaging		
Equivalent circular diameter (ECD)	Microns	The diameter of a circle occupying the same area as the particle
Intensity mean	Intensity (0 – 1023)	The average intensity of all image pixels representing the particle
Intensity standard Deviation	Intensity (0 – 1023)	The standard deviation of the intensity of all pixels representing the particle
Circularity	No units (0 – 1)	The circumference of a circle with an equivalent area divided by the actual perimeter of the particle
Aspect ratio	No units (0 – 1)	The ratio of the minor axis length over the major axis length of an ellipse that has the same second-moment-area as the particle
FlowCAM		
Area based diameter (ABD)	Microns	The diameter based on a circle with an area that is equal to that of the particle
Symmetry	No units (0 – 1)	A measure of the symmetry of the particle around its center. If a particle is symmetric then the value is one.
Aspect ratio	No units (0 – 1)	The ratio of the width (the shortest axis of the particle) and length (the longest axis of the particle)
Circle fit	No units (0 – 1)	Deviation of the particle edge from a best-fit circle, normalized to the zero to one range where a perfect fit has a value of one.
Circularity	No units (0 – 1)	A shape parameter computed from the perimeter and the area. A circle has a value of one. Formula: $(4 \times \pi \times \text{Area}) / \text{Perimeter}^2$.

Suite (MVAS) Version 1.2. Table 1 summarizes the main morphological parameters provided by the MVAS and their descriptions. The size distribution of each sample was presented in equivalent circular diameter (ECD). Each sample was measured three times with MFI.

FlowCAM

The second flow imaging technique used in this study was a FlowCAM VS1 (Fluid Imaging Technologies, Yarmouth, ME, USA). After rinsing the FC50 flow cell with ultrapure water, 100 μ L of each 4-fold diluted sample was run at a flow rate of 0.030 ml/min controlled by a C70 syringe pump. Images were taken with a Sony XCD-SX90 camera at 22 fps (shutter: 8,

gain: 224, 20x lens). The data were analyzed by Visual SpreadSheet Version 3 and a filter for area-based diameter ($ABD > 4\mu\text{m}$) was applied. Aspect ratio (> 0.3) and circle fit (> 0.1) were also chosen to exclude impurities with non-circular shapes. No additional filters were applied for derivation of total cell concentration. However, for study of the morphological parameters associated with non-viable cells and subsequent viability determination of different samples, additional filters were used. In order to remove edge particles (particles that were detected at the borders of the camera field, hence imaged partially), the acceptable detection field was reduced to 95 – 1183 and 6 – 952, respectively, for left-right and top-bottom orientations. The edge gradient parameter provided by FlowCAM was used to exclude out-of-focus particles. The acceptable range for edge gradient was determined in a preliminary study. In Table 1, descriptions of the main morphological parameters provided by the Visual SpreadSheet are given. It is worth mentioning that the FlowCAM can calculate the particle size through two different algorithms. In our study we chose to proceed with the area based diameter (ABD) only, because the principle of ABD and ECD is similar.

Fluorescence-activated cell sorting (FACS)

Flow cytometric cell sorting (FACS) on a FACSAria III (BD Biosciences, New Jersey, USA) was used to separate dead and/or dying cells from living cells based on the forward scatter (FSC) and side scatter (SSC) 'live gate' as shown in Supplementary Figure S1. The presumably dead and live cells that were collected with the FACS were then measured with MFI and FlowCAM. These FIM data were used to develop data filters for dead and live cells for each FIM technique. For this purpose the parameter that showed highest difference (for both instruments the size) between live and dead cells, was used as a primary filter. After applying this primary filter, the changes of all the other parameters were monitored. Consequently, threshold values for all the other parameters could systematically be fine-tuned. At the end, the filters were tested on the analyzed sorted fractions and FIM derived viability was compared to the trypan blue assisted values found for each cell sample.

Results

The two B-ALL cell lines were thawed, analyzed and then left at ambient temperature for 8 days and analyzed at predetermined time points, as described in materials and methods.

Monitoring cell concentration over the eight-days study period

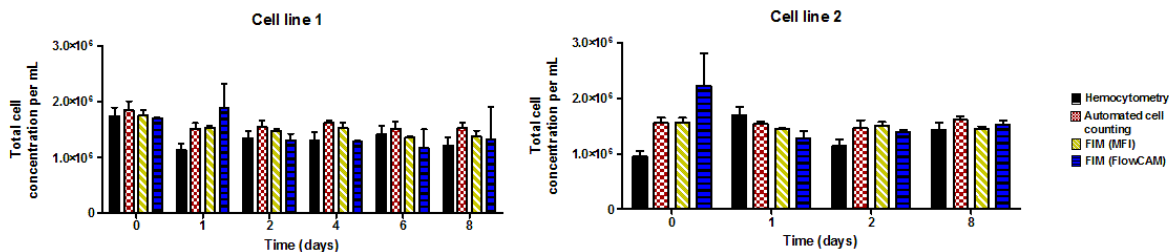


Figure 1: Total cell concentration of (A) cell line 1 and (B) cell line 2 measured at different time points during an 8-day incubation period, as measured by hemocytometry (black), automated cell counting (red), MFI (yellow) and FlowCAM (blue). Error bars represent the standard deviation of triplicate measurements with each technique.

Figure 1 shows the total (live and dead) cell concentrations as measured with all four techniques over the 8-days study period, for both investigated cell lines. The results indicate that all the techniques gave fairly similar cell concentrations. FlowCAM appeared to have the lowest precision, followed by hemocytometry, as judged by the standard deviations. The cell concentration of the cell line 1 showed a decreasing trend over time, whereas for cell line 2 the cell counts remained fairly stable.

Morphological parameters of B-ALL cells monitored with FIM techniques

Both flow imaging microscopy techniques provide morphological parameters of the detected particles (including cells) obtained from the individual images. A few representative images of individual particles detected by the two FIM techniques are shown in Figure 2. It is obvious that FlowCAM has a much higher lens magnification, as seen from the size of the image being larger for the same cell sizes measured with MFI. The high resolution images of FlowCAM compared to MFI may result in the ability to derive more morphological parameters using FlowCAM than MFI. Nevertheless, some of the most relevant parameters allowed a comparison of FlowCAM with MFI (see Table 1). In our 8-days study we monitored changes in all the 5 parameters listed in Table 1 for the studied cells.


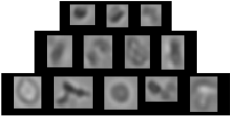
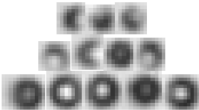
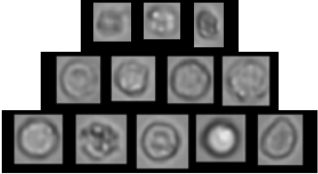

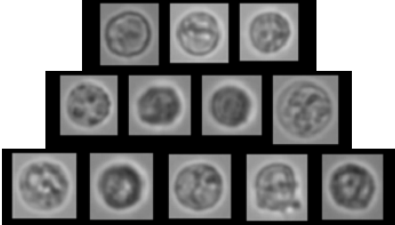

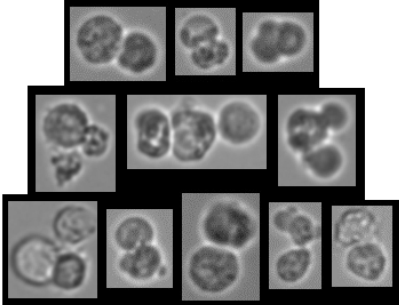
	MFI	FlowCAM
2 – 5 μm		
5 – 10 μm		
10 – 15 μm		
Aggregates		

Figure 2: Representative images of the cells detected by MFI (middle column) and FlowCAM (right column). The cells are categorized in three size ranges as shown in the left column.

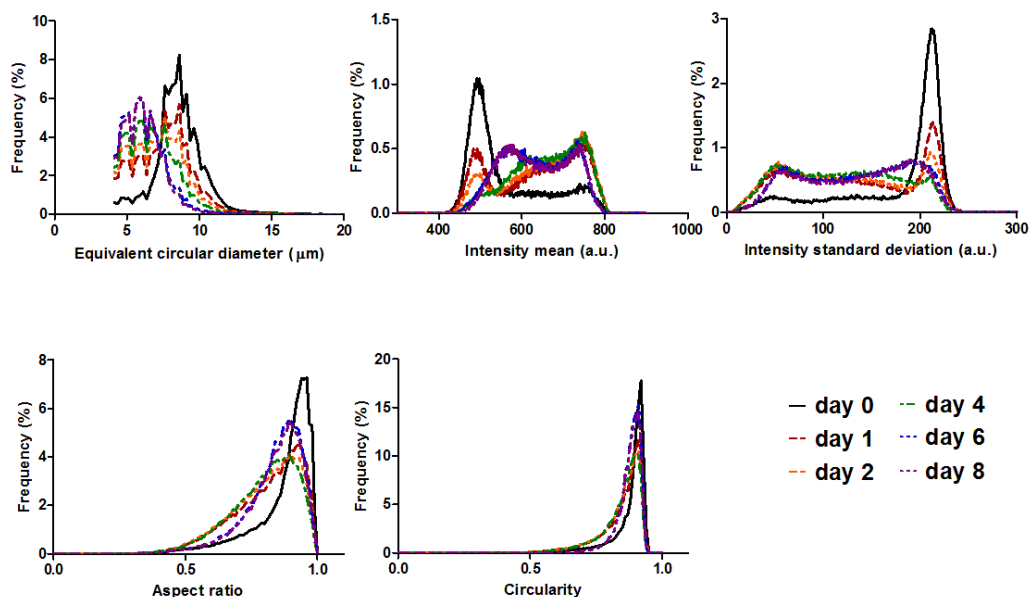


Figure 3: Overview of the changes in different morphological parameters, including size (equivalent circular diameter), of cell line 1, as observed with MFI, during the incubation study. Different line colors represent measurements at different days. For each parameter the frequency distribution of the corresponding parameter unit range is shown.

Figure 3 shows the distribution of particles over the parameters derived from the MFI analysis for cell line 1 during the 8-days incubation study. The size distribution graph shows that there was a decrease in the number of the larger particles and an increase in the number of smaller particles over time. The peak around 8 µm in the distribution of day 1 slowly descended, while a new peak around 6 µm rose and became apparent at day 8. The intensity frequency graphs showed a similar trend. Fresh cell suspension showed pronounced peaks around 490 and 210, respectively, for the mean and standard deviation of intensity. Incubation over time resulted in a decrease of aforementioned peaks and appearance of two other peaks in each graph, namely at 560 and 730 for the mean intensity and at 50 and 180 for the standard deviation of the intensity. For the shape related parameters, *i.e.*, circularity and aspect ratio, only the latter showed distinctive changes in its distribution graph. The aspect ratio value started to decrease and deviated further from 1 over time. The same trend in ECD and intensity mean was observed for cell line 2 (see Supplementary Figure S2). The intensity standard deviation for cell line 2 showed only a decrease and broadening in the main peak, whereas the changes in the shape related parameters were not considerable.

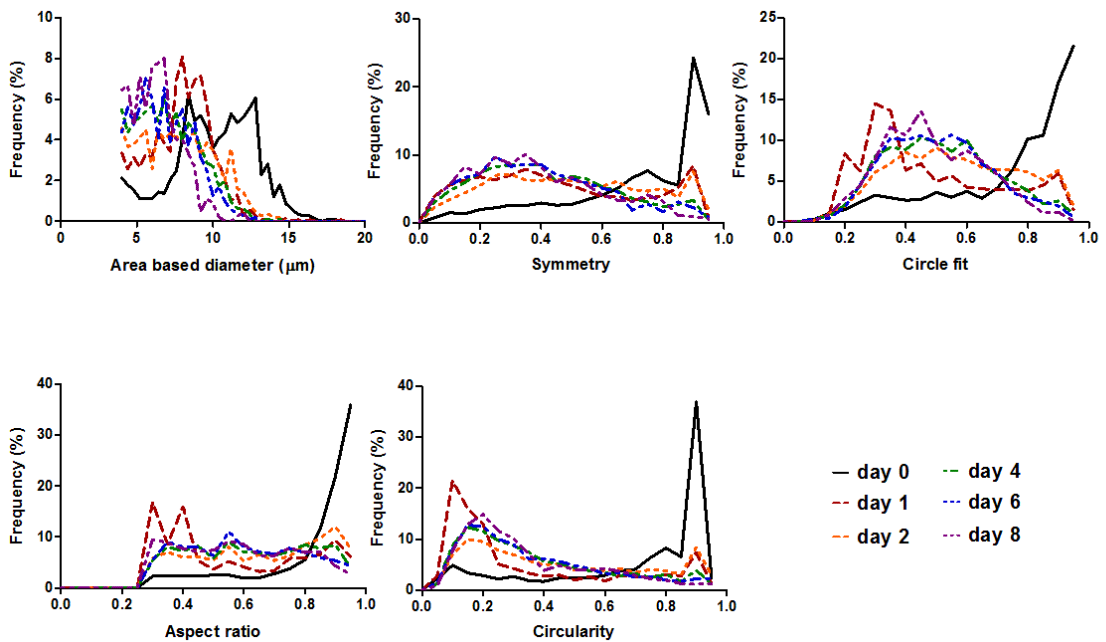


Figure 4: Overview of the changes in different morphological parameters, including size (area based diameter), of cell line 1, as observed with FlowCAM, during the incubation study. Different line colors represent measurements at different days. For each parameter the frequency distribution of the corresponding parameter unit range is shown.

The distribution of particles over the parameters studied with the FlowCAM is shown in Figure 4. The change in the ABD size distribution was fairly similar to the changes seen in the ECD size distribution with MFI. Fresh cell sample showed a distinct peak at about 12 µm and over time this peak disappeared and was replaced by relatively broad peak at a smaller size range (around 6 µm). However, there was also a third transient peak at about 8 µm seen, which was already present in the fresh sample and increased after 24 hours, and then diminished in the following days. In contrast to MFI, with FlowCAM the changes in the particle intensity were not monitored (further explained in the *Discussion* section), and the focus was only put on four shape related parameters. All these parameters showed a distinct peak with a value close to 1 for fresh cell sample, which gradually decreased over days. For symmetry and circle fit a broad peak at about 0.3 and 0.45, respectively, rose and for circularity a narrower peak with a value of 0.2 appeared. Noticeably, for the aspect ratio the frequency distribution did not change considerably after 24 hours of incubation. For cell line 2, all the studied morphological parameters followed a similar trend, although the changes were less pronounced (see Supplementary Figure S3).

Fractionation and FIM derived morphology of dead and live cells

The fresh cell suspension of the first cell line was analyzed with a flow cytometer to derive an appropriate gate for sorting dead and live cells (see Supplementary Figure S1). After the fractions of the dead and live cells as identified by flow cytometry were collected, a control trypan blue assisted viability test of each fraction was performed on the automated cell counter. From these control measurements it was found that the live population contained almost 90% viable cells, whereas the dead population contained no more than 20% viable cells. For comparison, the unfractionated cell population contained about 75% viable cells. The sorted populations were thereafter measured with both FIM techniques to derive the values for the different morphological parameters for live and dead cells separately. The results are shown in Table 2 and indicate that there was a statistically significant difference between the values of each parameter for live and dead cells, except for the circularity values derived from MFI and FlowCAM. The R^2 values indicate the extent of this difference, where a higher R^2 indicates a larger difference between live and dead for that particular parameter. Thereafter, we defined filters based on the monitored parameters for dead and live cells, as shown in Table 3. It has to be noted that although there was no statistically significant difference between the values

Table 2: Derived mean and standard deviation of the morphological parameters provided by MFI and FlowCAM for the two cell fractions of cell line 1 sorted using FACS. The morphological parameters of the dead and live cells are statistically compared, with the results presented in the two rightmost columns.

Flow imaging microscopy morphological parameters*		Live cell population	Dead cell population	Statistical comparison Different?	R^{2**}
Micro-Flow Imaging					
	ECD	$7.6 \pm 2.2 \mu\text{m}$	$5.8 \pm 1.8 \mu\text{m}$	Yes	0.171
	IntMean	546 ± 87	573 ± 81	Yes	0.026
	IntSD	179 ± 53	173 ± 55	Yes	0.003
	Cir	0.88 ± 0.06	0.88 ± 0.05	No	n.a.
	AR	0.85 ± 0.12	0.87 ± 0.10	Yes	0.008
FlowCAM					
	ABD	$7.7 \pm 3.0 \mu\text{m}$	$6.4 \pm 2.6 \mu\text{m}$	Yes	0.055
	Sym	0.74 ± 0.19	0.69 ± 0.17	Yes	0.019
	AR	0.82 ± 0.16	0.80 ± 0.13	Yes	0.005
	CF	0.77 ± 0.17	0.75 ± 0.13	Yes	0.004
	Cir	0.78 ± 0.17	0.78 ± 0.12	No	n.a.

*Tested morphological parameters: equivalent circular diameter (ECD), intensity mean (IntMean), intensity standard deviation (IntSD), circularity (Cir), aspect ratio (AR), area based diameter (ABD), symmetry (Sym) and circle fit (CF).

**Derived after applying t-test with GraphPad Prism 5[®]. R² quantifies the fraction of all the variations in the samples that is accounted for by a difference between the group means. n.a. = 0.

of circularity for live and dead cells, this parameter appeared to be distinctive (and useful in definition of the FlowCAM filters) when used on top of filters based on other parameters.

Comparing cell viability determination by FIM techniques, hemocytometry and automated cell counting

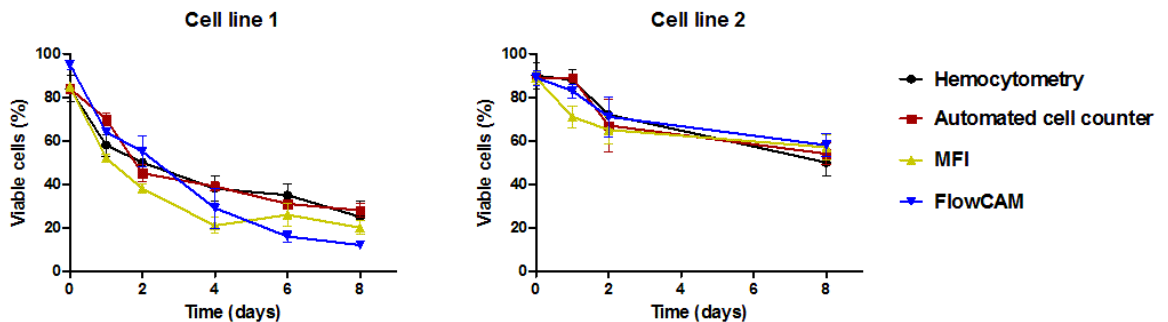


Figure 5: Percentage of viable cells determined with different analytical methods for the cell line 1 at different time points during the 8-day incubation period: hemocytometry (black), automated cell counting (red), MFI (yellow) and FlowCAM (blue). The error bars represent standard deviations of triplicate measurements with each technique.

With the help of the filters for fractionated cells, the percentage of viable cells was calculated for both cells at different time points (Figure 5). These percentages obtained from different techniques showed similar trends for the viability of both cell lines, *i.e.*, a gradually decreasing viability over incubation time. In addition, cell line 2 showed a stronger survival potency at the studied incubation conditions (75% decrease in viable cells after 8 days) than cell line 1 (50% decrease).

Discussion

In clinical practice, where CTPs are required to be checked for concentration and viability prior to administration, a more rapid and easier method would be highly beneficial. In this study we have investigated the potential of two different FIM techniques for this purpose and have shown that both techniques can be used to measure the concentration and the viability of cells, yielding comparable results to those obtained with conventional hemocytometry and cell counting methods.

Table 3: Comparison of the different aspects of the techniques evaluated in this study

Characteristics	Hemocytometry	Automated cell counting	FIM (MFI)	FIM (FlowCAM)
General				
Analyzed sample volume	0.1 μ L	0.4 μ L	260 μ L	20 μ L
Sample pretreatment	Labelling; dilution if needed	Labelling; dilution if needed	Dilution	Dilution
Analysis time per sample (measurement + data analysis)	5 minutes	1 minute	15 minutes	10 minutes (depends on measurement settings)
Cell counting and viability determination				
Accuracy	Moderate	Moderate	High	Moderate
Precision	Moderate	Moderate	High	Low
Additional features				
Non-cellular particles	Discarded visually from the cell counts	May interfere with the cell counting	Can be removed from the data afterwards	Can be removed from the data afterwards
Detection of cell debris	Depends on magnification lens used	Not possible	Possible	Possible
Cell identification	Visual identification	Not possible	Possible using morphology based filters	Possible using morphology based filters

The FIM methods, once developed, are easy to perform and do not require staining of the cells before the measurement (see comparison made in Table 3). These techniques measure a large sample volume and thus count considerably more cells than the conventional methods such as hemocytometry. This ability is a great asset for the accuracy and precision of both counting and cell viability determination. Another advantage of FIM lies in its ability to image individual cells and obtain morphological characteristics of each cell. This capability allows avoiding the usage of labels. Moreover, non-cellular materials can be manually removed from the data, to avoid inaccurate counting. Furthermore, the imaging likely allows the discrimination of different types of cells (and/or non-cellular particles) in a heterogeneous population.

Although hemocytometry, automated cell counting, MFI and FlowCAM are all able to provide an estimation of the cell concentration, standard deviations presented in Figure 1 indicate that the precision of methods with respect to the cell concentration measurement follows this pattern FlowCAM < hemocytometry < automated cell Counter < MFI. For FlowCAM the combination of the type of flow cell and image frequencies used in our settings resulted in a theoretical analysis efficiency of around 20%, meaning that only 20% of the dispensed cell suspension was actually imaged. This limitation in combination with the inability of

the analysis package in exclusion of stuck particles that appear in several images from the analysis may be the most important contributing factors to the relatively low precision. Despite the larger amount of suspension volume measured with the automated cell counter, automated cell counting did not show superior precision over hemocytometry with respect to cell concentration. This may be caused by the interference of non-cellular material with the cell counting. In contrast, MFI resulted in the highest precision. The large amount of imaged sample (more than 260 μL vs. 0.1 μL in hemocytometry), high analysis efficiency (about 85%) and ability to remove stuck particles from being counted multiple times may explain the pronounced performance of MFI with respect to the concentration determinations. Moreover, precision of hemocytometry may also be affected by the operator, since the method requires visual counting and viability assessment based on visual discrimination of the color of the cells.

Monitoring of the total concentration of cell line 1 over time revealed a decreasing trend in total cell concentration for all the methods. It is known that the dying and dead cells undergo fragmentation into smaller particles²³. Presumably these cell debris particles are below the lower size limit of the automated cell counting and the lower size limit chosen for FIM techniques (4 μm), while in hemocytometry non-cellular particles are visually excluded and therefore not counted. FIM data confirm this theory as the ECD and ABD size distribution diagrams (Figure 3 and Figure 4) show a clear increase in the number of particles below 7 μm over time. This increase was even more pronounced for particles below 4 μm , in particular for ECD (Supplementary Figure S4). This observation suggests that the FIM techniques are presumably able to detect and count cell fragments as well. Analysis of the FIM parameters for incubated cells revealed clear changes in the majority of the parameters highlighted in this study, namely ECD, intensity mean, intensity SD and aspect ratio for MFI; and ABD, symmetry, aspect ratio, and circle fit for FlowCAM. Both MFI and FlowCAM revealed a decreasing trend in the size (ECD and ABD, respectively) of the cells during the incubation. Moreover, cells at later time points appeared to have a higher intensity, a lower intensity SD and smaller aspect ratios. The latter, together with lower symmetry and circle fit values, indicate that the shape of the cells changes towards less symmetric and more elongated particles. All these observations point towards a decrease in the population of live cells and/or changes in the quality of the live cell population. Shrinkage of cell size and changes in cell shape are observed for dead and dying cells whose concentration is expected to increase under stress¹³. Furthermore a decrease in the intensity SD can be a sign of disappearance of the cell organelles that contributed to variations in intensity of the image in a cell. In order to investigate if all these changes are correlated, the data from day 1 and 8 were analyzed further by making 3D plots that show the distribution of cells over two MFI derived parameters at the same time (Supplementary

Figure S5). The peak at 480 a.u. in the intensity mean graph of Figure 3 at day 0 belongs to the ECD population around 8 μm (presumably live cells). At day 8 the decrease in cell size and increase in cell intensity result in appearance of a new peak with intensity mean of 730 and ECD of 6 μm (presumably dead cells). Similar changes in other parameters and FlowCAM (Supplementary Figure S6) are observed when the same approach is applied to look into different populations based on size. Overall, these correlated changes in all the morphology parameters for cell population exposed to stress strongly suggest that MFI and FlowCAM are able to pick up early stages of loss in viability that may cause changes in the transparency and shape of the cells¹³.

Table 4: Specification of the filters used to identify dead and live cells from analysis results

Flow imaging microscopy morphological parameters		Filter for live cell population	Filter for dead cell population
Micro-Flow Imaging			
	ECD	> 7.25 μm	4 – 7.25 μm
	IntMean	\leq 550	\geq 550
	IntSD	\leq 170	\geq 170
FlowCAM			
	ABD	> 7.0 μm	4 – 9 μm
	Sym	\geq 0.7	\leq 0.8
	AR	\geq 0.8	0.6 – 0.8
	CF	\geq 0.7	\leq 0.8
	Cir	\geq 0.8	0.3 – 0.8

In order to confirm the capability of FIM characterization for identification of live and dead cells and also to define filter conditions that allow quantitative analysis viability separated live and dead cells were obtained by FACS and analyzed. After gating and separation of the two distinct populations as seen in FSC-SCC plot, the live and dead cells were analyzed by both FIM techniques and filter values that allowed distinction of dead from live cells were determined. The filters were constructed by setting one value at a time starting from the most distinctive parameter until no change was observed in the populations. Filter values for MFI data do not include aspect ratio and circularity. After setting the primary filter the values of these two parameters did not change that much between live and dead populations. Filters for FlowCAM, however, included more parameters including circularity. These filters, summarized in Table 4, clearly depict the observations of the incubation experiments. For instance the average size and average intensity are smaller for dead cells.

It has to be noted that the two FIM techniques described herein offer several other morphological parameters that could be used in analysis of the cells. However, the combination of a high-magnification lens and a thin focus plane of the flow cell results in substantial numbers of imaged particles that were out of focus. These particles affect the values of a few morphological parameters (e.g., intensity), and therefore were not included

in our study.

In our study we aimed to develop a label-free FIM based method to derive viability of cells. In order to avoid complexity of the cell sample, we have used a model containing one type of cells, *i.e.*, B-ALL cell lines. However, CTPs may contain cells with different morphological properties than B-ALL cells or contain multiple cell types. For example, different hematopoietic progenitor cell products contain heterogeneous cell population²⁴. In principle one can apply the same approach to other cell types and heterogeneous cell populations. Therefore, one needs to develop specific filters for each type of cells.

Conclusion

In this study we have investigated the capability of two different FIM techniques, MFI and FlowCAM, to be used as a label-free method for cell concentration and viability determination. Our data suggests that both methods deliver fairly similar results for concentration and quality determination of cellular products as traditional methods, *i.e.*, hemocytometry and the automated cell counting. Whereas the MFI method showed a higher precision with respect to determination of the cell concentration, the FlowCAM method provides higher-resolution images. The latter may be useful to identify non-cellular particles and potentially discriminate between different types of cells.

References

1. Larijani B, Esfahani EN, Amini P, Nikbin B, Alimoghaddam K, Amiri S, Malekzadeh R, Yazdi NM, Ghodsi M, Dowlati Y, Sahraian MA, Ghavamzadeh A 2012. Stem cell therapy in treatment of different diseases. *Acta medica Iranica* 50(2):79-96.
2. Mason C, Brindley DA, Cume-Seymour EL, Davie NL 2011. Cell therapy industry: billion dollar global business with unlimited potential. *Regen Med* 6(3):265-272.
3. Moviglia GA, Vina RF, Brizuela JA, Saslavsky J, Vrsalovic F, Varela G, Bastos F, Farina P, Etchegaray G, Barbieri M, Martinez G, Picasso F, Schmidt Y, Brizuela P, Gaeta CA, Costanzo H, Brandolino MM, Merino S, Pes ME, Veloso MJ, Rugilo C, Tamer I, Shuster GS 2006. Combined protocol of cell therapy for chronic spinal cord injury. Report on the electrical and functional recovery of two patients. *Cytotherapy* 8(3):202-209.
4. Hickey MJ, Malone CC, Erickson KE, Gomez GG, Young EL, Liao LM, Prins RM, Kruse CA 2012. Implementing preclinical study findings to protocol design: translational studies with alloreactive CTL for gliomas. *American journal of translational research* 4(1):114-126.
5. Gomez-Lechon MJ, Lahoz A, Jimenez N, Bonora A, Castell JV, Donato MT 2008. Evaluation of drug-metabolizing and functional competence of human hepatocytes incubated under hypothermia in different media for clinical infusion. *Cell transplantation* 17(8):887-897.
6. Leverett LB, Hellums JD, Alfrey CP, Lynch EC 1972. Red blood cell damage by shear stress.

Biophysical journal 12(3):257-273.

7. Bravery CA, Carmen J, Fong T, Oprea W, Hoogendoorn KH, Woda J, Burger SR, Rowley JA, Bonyhadi ML, Van't Hof W 2013. Potency assay development for cellular therapy products: an ISCT review of the requirements and experiences in the industry. *Cytotherapy* 15(1):9-19.
8. Strober W 2001. Trypan blue exclusion test of cell viability. *Current protocols in immunology* / edited by John E Coligan [et al] Appendix 3:Appendix 3B.
9. Panterne BR, M.J., Sabatini C, Ardiot S, Huyghe G, Lemarie C, Pouthier F, Mouillot L. 2011. Ten Years of External Quality Control for Cellular Therapy Products in France. ed.: InTech. p 660.
10. Donner KJ, Becker KM, Hissong BD, Ahmed SA 1999. Comparison of multiple assays for kinetic detection of apoptosis in thymocytes exposed to dexamethasone or diethylstilbestrol. *Cytometry* 35(1):80-90.
11. Kurec A 2014. Flow cytometry: principles and practices. *MLO: medical laboratory observer* 46(5):28, 30-21.
12. Sharma DK, King D, Oma P, Merchant C 2010. Micro-Flow Imaging: Flow Microscopy Applied to Sub-visible Particulate Analysis in Protein Formulations. *Aaps Journal* 12(3):455-464.
13. Matsubayashi M, Ando H, Kimata I, Nakagawa H, Furuya M, Tani H, Sasai K 2010. Morphological changes and viability of *Cryptosporidium parvum* sporozoites after excystation in cell-free culture media. *Parasitology* 137(13):1861-1866.
14. Tsaousis KT, Kopsachilis N, Tsinopoulos IT, Dimitrakos SA, Kruse FE, Welge-Luessen U 2013. Time-dependent morphological alterations and viability of cultured human trabecular cells after exposure to Trypan blue. *Clinical & experimental ophthalmology* 41(5):484-490.
15. Wu L, Martin T, Li Y, Yang L, Halpenny M, Giulivi A, Allan DS 2012. Cell aggregation in thawed haematopoietic stem cell products visualised using micro-flow imaging. *Transfus Med* 22(3):218-220.
16. Farrell CJ, Cicalese SM, Davis HB, Dogdas B, Shah T, Culp T, Hoang VM 2016. Cell confluency analysis on microcarriers by micro-flow imaging. *Cytotechnology*.
17. Werk T, Volkin DB, Mahler HC 2014. Effect of solution properties on the counting and sizing of subvisible particle standards as measured by light obscuration and digital imaging methods. *European Journal of Pharmaceutical Sciences* 53:95-108.
18. Frahm GE, Pochopsky AW, Clarke TM, Johnston MJ 2016. Evaluation of Microflow Digital Imaging Particle Analysis for Sub-Visible Particles Formulated with an Opaque Vaccine Adjuvant. *PLoS one* 11(2):e0150229.
19. Zolls S, Weinbuch D, Wiggenhorn M, Winter G, Friess W, Jiskoot W, Hawe A 2013. Flow imaging microscopy for protein particle analysis--a comparative evaluation of four different analytical instruments. *The AAPS journal* 15(4):1200-1211.
20. Weinbuch D, Zolls S, Wiggenhorn M, Friess W, Winter G, Jiskoot W, Hawe A 2013. Micro-flow imaging and resonant mass measurement (Archimedes)--complementary methods to

quantitatively differentiate protein particles and silicone oil droplets. *Journal of pharmaceutical sciences* 102(7):2152-2165.

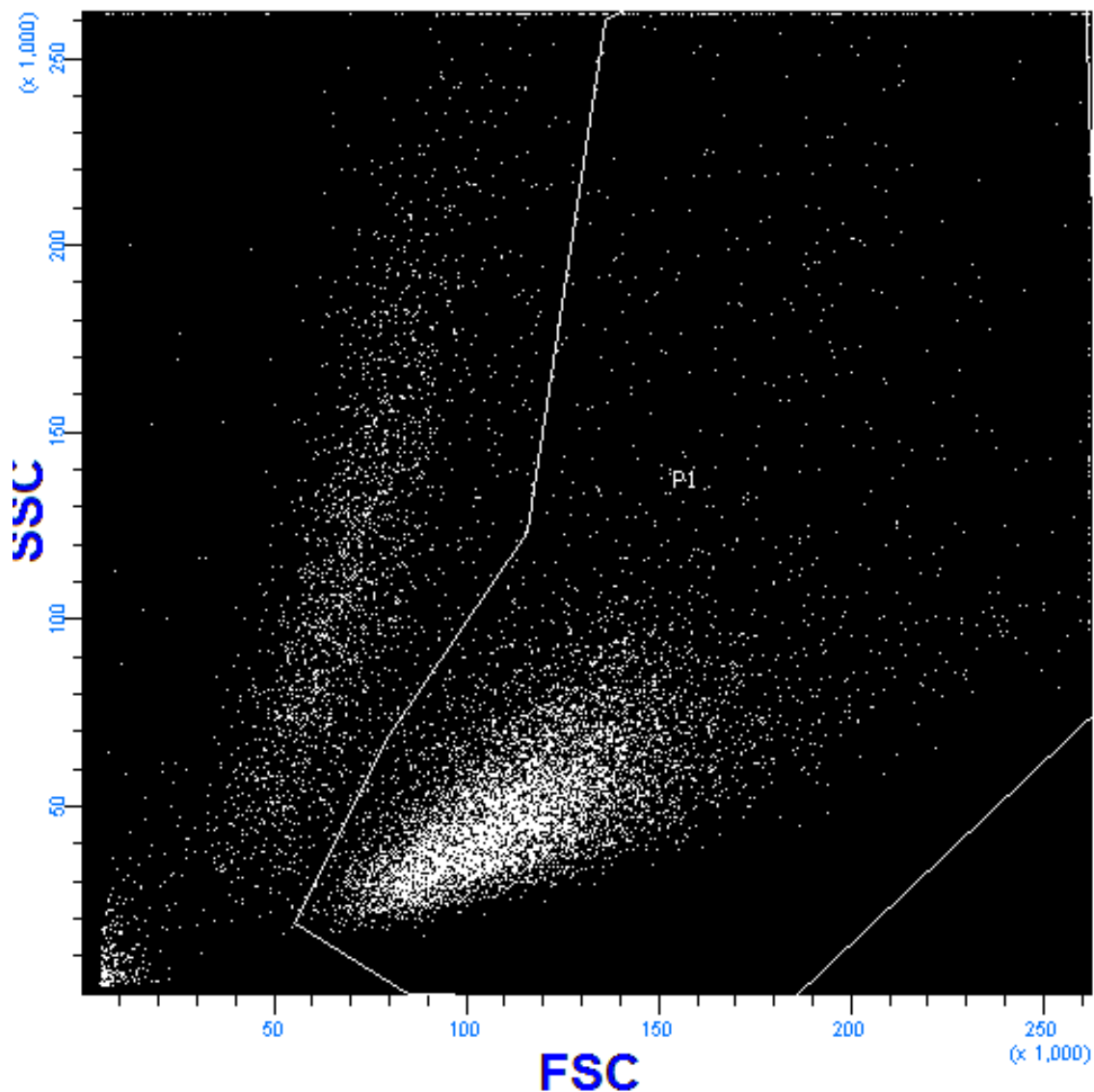
21. Nijmeijer BA, Szuhai K, Goselink HM, van Schie ML, van der Burg M, de Jong D, Marijt EW, Ottmann OG, Willemze R, Falkenburg JH 2009. Long-term culture of primary human lymphoblastic leukemia cells in the absence of serum or hematopoietic growth factors. *Exp Hematol* 37(3):376-385.

22. Louis KS, Siegel AC 2011. Cell viability analysis using trypan blue: manual and automated methods. *Methods in molecular biology* 740:7-12.

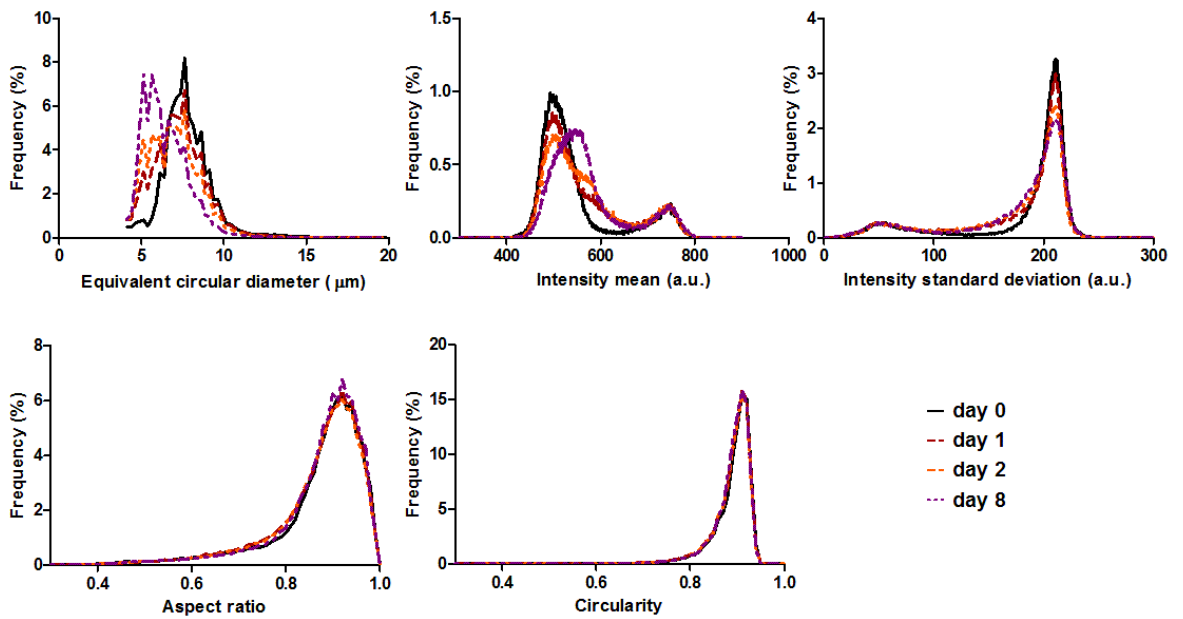
23. Kerr JFR, Wyllie AH, Currie AR 1972. Apoptosis - Basic Biological Phenomenon with Wide-Ranging Implications in Tissue Kinetics. *Brit J Cancer* 26(4):239-&.

24. Services USDoHaH. 2016. Cellular & Gene Therapy Products: Marketed Products. ed.

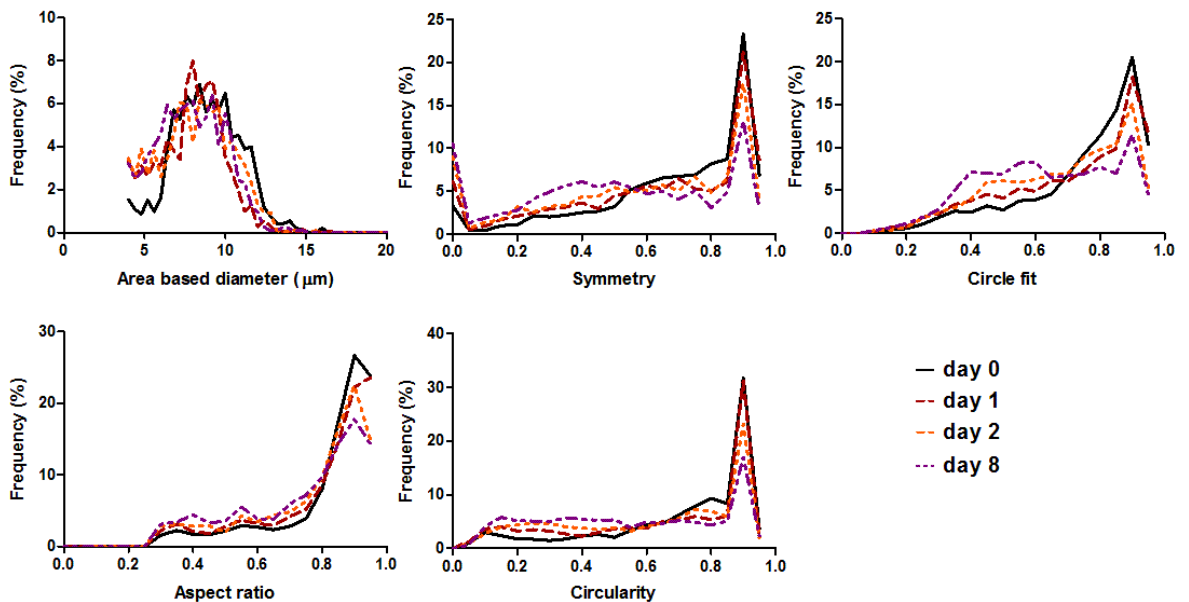
Supplementary Information



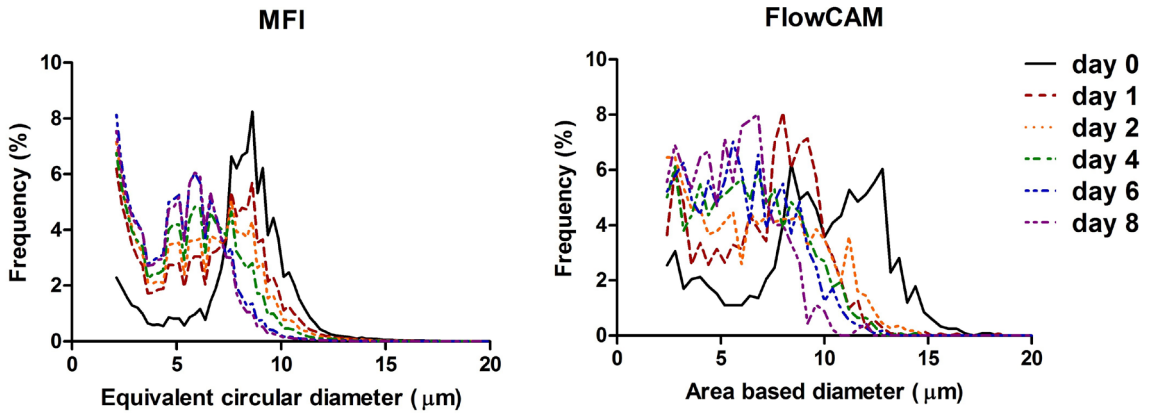
Supplementary Figure S1: Gating strategy for the FACS supported sorting of dead/dying and viable cells. The graph shows the FSC – SSC plot for the sample containing fresh cells from cell line 1. The gated population is considered viable.



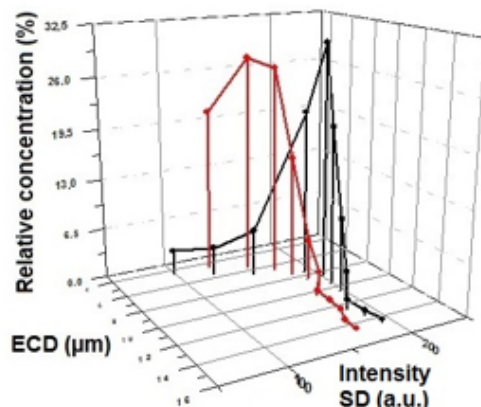
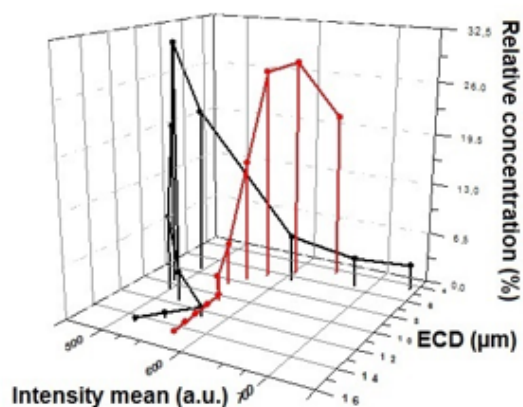
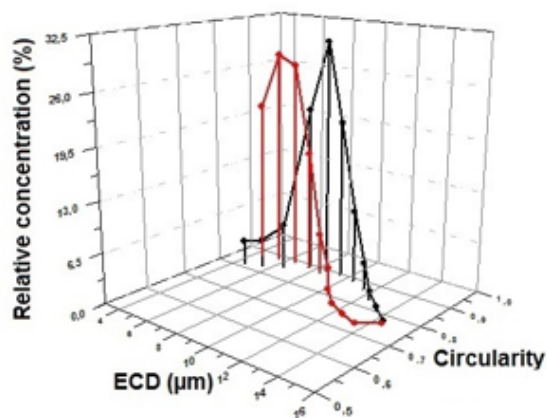
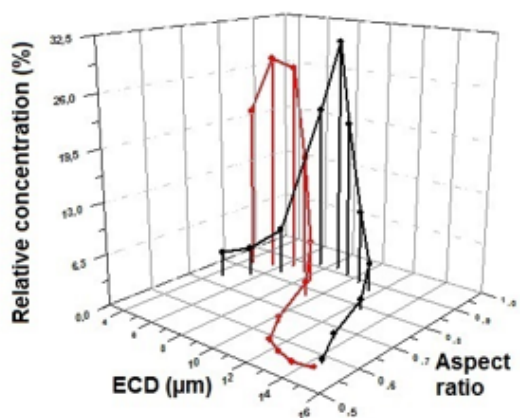
Supplementary Figure S2: Overview of the changes observed in different morphological parameters as function of incubation time of cell line 2, as observed with MFI, during the incubation study. For each parameter the frequency distribution of the corresponding parameter unit range is shown.



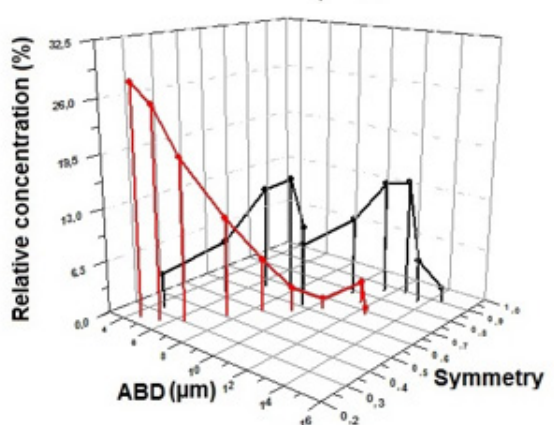
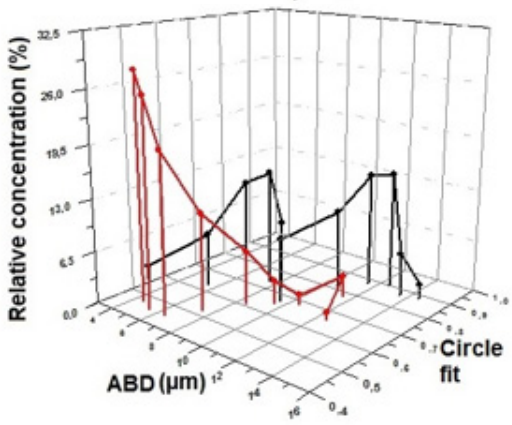
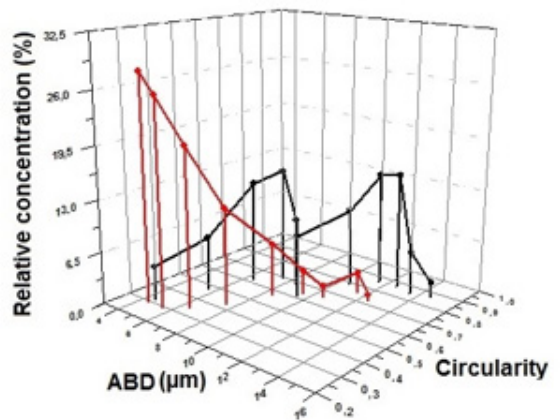
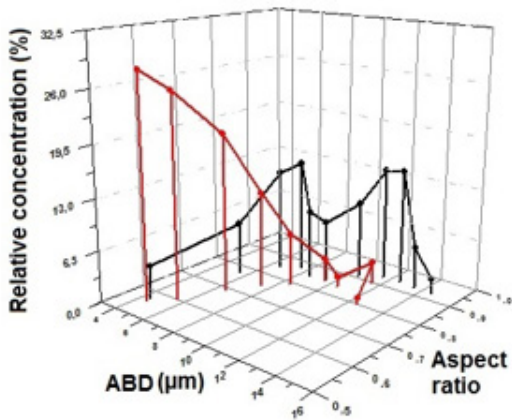
Supplementary Figure S3: Overview of the changes observed in different morphological parameters as function of incubation time of the cell line 2, as observed with FlowCAM, during the incubation study. For each parameter the frequency distribution of the corresponding parameter unit range is shown.



Supplementary Figure S4: Changes in MFI and FlowCAM sizing parameters, of cell line 1, during the incubation study.



Supplementary Figure S5: Overview of the MFI derived aspect ratio, circularity, average intensity and SD intensity for different ECD-based size populations. The x-axis in all the graphs shows these populations as 1- μm size bins (from 4 – 15 μm). The y-axis presents the concentration of each 1- μm size bin populations relative to the total concentration. In the z-plane the average values of different morphological parameters for each size-based population is shown. The results for samples of fresh cells (in black) and cells incubated for 8 days at ambient conditions (in red) are shown.



Supplementary Figure S6: Overview of the FlowCAM derived aspect ratio, circularity, circle fit and symmetry for different ABD-based size populations. The x-axis in all the graphs shows these populations as 1- μm size bins (from 4 – 15 μm). The y-axis presents the concentration of each 1- μm size bin populations relative to the total concentration. In the z-plane the average values of different morphological parameters for each size-based population is shown. The results for samples of fresh cells (in black) and cells incubated for 8 days at ambient conditions (in red) are shown.

Summary and perspectives



A.S. Sediq, M.R. Nejadnik, W. Jiskoot

Division of Drug Delivery Technology, Cluster BioTherapeutics, Leiden Academic Centre for Drug Research (LACDR), Leiden University, Leiden, The Netherlands

Summary

Complex injectable formulations, such as protein therapeutics¹, controlled release systems² and cell therapy products³, are gaining a paramount position in the therapy of many life-threatening and chronic diseases. Most of these products have in common that sub-visible particles (SVP), *i.e.*, particulate matter in the size range of about 1 – 100 μm , are critical quality attributes. Most protein therapeutics are liquid or freeze-dried formulations in which the presence of SVP is unwanted⁴; many injectable controlled release systems are based on particulate drug delivery systems in the sub-visible size range⁵; and cell concentration and viability are important characteristics of cell therapy products⁶. With the continuous improvement of existing and emerging particle analysis techniques, the potentials of these tools in addressing current characterization challenges in the field of complex injectable formulations have to be investigated. Therefore, the aim of this thesis was to develop methods, based on a set of state-of-the-art particle analysis techniques, for characterization of pharmaceutically relevant sub-visible particles and to study the value of these methods in the characterization of complex injectable formulations.

Stirring-induced protein aggregation is encountered at different stages of manufacturing of biologics. In *Chapter 2* we have investigated the cause of this particular type of aggregation due to mechanical stress. For this purpose we designed an overhead stirring set-up in order to manipulate the presence and magnitude of the contact between the stir bar and the container. It was found that contact sliding during stirring initially resulted in the formation of submicron protein aggregates (100 – 1000 nm) of tested protein, IgG, as measured by nanoparticle tracking analysis (NTA). Continuation of such stirring increased the number of aggregates and led to the growth of particles into sub-visible aggregates, as analyzed by Micro-Flow Imaging (MFI). Interestingly, no increase in oligomer content was seen in size-exclusion chromatography (SEC), suggesting a rapid particle formation. Our investigation showed that the adjustment of the contact area of stirring and pressure applied by the stir bar on the glass surface affected the extent of aggregation. Formation of particles during stirring could be prevented by either addition of polysorbate 20 or avoiding contact between the solid surfaces. Herewith we have provided new insight into the mechanism of stirring-induced protein aggregation, by pointing out its root cause and suggesting formulation and process strategies to inhibit this route of protein aggregation.

In *Chapter 3* we have used a combination of NTA and MFI to get new insights into the kinetics and mechanism of protein-polyelectrolyte complexation. In this study we used IgG and dextran sulfate (Mw = 5000) as the model protein and polyelectrolyte, respectively. A solution of each with equal mass based concentration was prepared, mixed with the other and the resulting mixture was homogenized gently. Samples were taken at different time points and analyzed for monomer content and quantity of nano- and microparticles.

SEC analysis showed that immediately after mixing all the protein was complexed into a high number of nanometer sized particles, which was detected, sized and counted by NTA. Thereafter, these nanoparticles were reduced in number and increased in size. After 1.5 hours microparticles were formed and also these particles continued to grow in size and be reduced in number, as observed by MFI measurements. With the help of the Smoluchowski's perikinetic coagulation model⁷, we fitted the changes in the total particle concentration, which enabled us to derive the so-called sticking probability of IgG-dextran sulfate complexes. The sticking probability is related to the interaction between the protein-polyelectrolyte complexes and can help determination of the growth rate of such complexes. We expect that this combination of particle analysis techniques could be used also for other systems, such as complexes between polymers and proteins, DNA and other biomacromolecules.

PLGA microparticle porosity is one of the critical parameters that affect the performance of these drug delivery systems with respect to the degradation of the particles and release of the drug. Our study in *Chapter 4* describes a novel method to derive microparticle porosity by tracking the sedimentation velocity of suspended particles using a flow imaging microscope. Two sedimentation based methods were investigated. In the first method we tracked sedimentation velocity of particles in liquids with different densities. Thereafter, we (intra- or) extrapolated to the point where the sedimentation velocity would be equal to 0. The fluid density value that matched that point was considered to be equal to the density of the particles under investigation. This value was then used to estimate the porosity with the given size and composition of the particles and the densities of the particle constituents. In the second method, we measured the size and sedimentation velocity of individual microparticles in a suspending fluid with known density. Then the density of the individual particles was calculated by using Stokes' law of sedimentation and porosity values were derived from density. We investigated the influential parameters and validated the methods using different sizes of polystyrene standard beads. Using the developed method, we determined microparticle porosity of different PLGA microparticle batches, and found similar results as the ones obtained by mercury intrusion porosimetry (MIP).

Chapter 5 introduces another method to derive PLGA microparticle porosity by using MFI. In this method, we suspended a known mass of microparticles in a fluid and measured the total microparticle volume accurately. The apparent density of particles was easily calculated based on the mass/volume ratio. Together with the known composition of the particles and the density of the components, we were able to derive the microparticle porosity. Parameters affecting the accuracy of the method, such as particle concentration, fluid density and particle adsorption to the container and instrument tubing, were investigated by using control PMMA beads. These influential parameters were optimized for the analysis of

7 different PLGA microparticle batches in order to derive the porosity of each. The results for all the 7 batches were fairly similar to the ones derived with MIP. The results indicate that this method can be used for a reliable assessment of PLGA microparticle porosity with only a few milligrams of powder.

In *Chapter 6* we have explored the applicability of flow imaging microscopy (MFI and FlowCAM) as a new technique to count cells in a suspension and determine cell viability. In this study, we have exposed B-lineage leukemia cells from two different donors to ambient conditions for several days, resulting in a reduction of cell viability. During this incubation study we measured samples from these cell suspensions with MFI, FlowCAM, hemocytometry and automated cell counting. The results from both flow imaging microscopy techniques showed changes in cell morphology that could be monitored with a number of parameters derived from each instrument. Using fluorescence assisted cell sorting (FACS) we were able to separate and collect dead and live cell populations. The morphological parameters of the separated dead and live cell populations were determined with FlowCAM and MFI, in order to develop morphological filters to discriminate dead and live cells in an unknown cell suspension. The filters were shown to be distinctive, as our analyses with flow imaging gave similar results for cell viability as the conventional methods (hemocytometry and automated cell counting). Also the cell concentration measurements delivered similar, if not better, results as hemocytometry and automated cell counting.

General discussion and perspectives

In the work described in this thesis we have investigated and developed new methods using either a combination of particle analysis techniques or a single particle analysis technique. All the methods described here have potential to be applied in pharmaceutical research and development.

In our study on protein aggregation induced by stirring (*Chapter 2*), the power of NTA to be able to track early stages of aggregation was shown. Although this method has its shortcomings with respect to reproducibility⁸, it still remains one of the few methods that can size and quantify particulate matter in the nanometer size range. Another interesting observation from *Chapter 2* was the concentration dependent average size of the micron sized particles that were formed: at higher protein concentration (0.5 mg/mL) the particles were consistently more than 1 μm larger than microparticles formed at lower concentration (0.1 mg/mL), as shown by MFI. This observation suggests that MFI is clearly able to reveal differences in the low-micrometer range and can be used for studying the kinetics of protein aggregation. Ideally, for investigation of the aggregation kinetics one needs to derive mass transfer or aggregation rate in relation to the influential parameters⁹, *i.e.*, for stirring induced aggregation the effect of the parameters such as surface area, protein concentration and

stirring rate (among others) on monomer/aggregate mass balance should be studied. One needs to recognize that converting aggregate size distribution to total aggregate mass is accompanied with a lot of assumptions with respect to the density of proteins and translation of the size to volume¹⁰. In this respect, the method for porosity assessment of microparticles described in *Chapter 4* might also be suitable to derive the density of protein aggregates (explained further in this section).

The method for determining particle growth and concentration presented in *Chapter 3* can be used to gain insight into the interaction strength between the polyelectrolyte-protein particles, which in turn affects the coagulation of complexes. The coagulation process continues until the aggregation and disintegration of complexes reach equilibrium, which in the end determines the final size of the complexes¹¹. The charge on both components of the complexes can be tailored by changing the pH and/or ionic strength of solution¹². In addition, concentration and ratio of the components have effects on the final size of the complexes¹³. The size of the final complexes determines their potential use in drug delivery¹⁴. Altogether, it can be concluded that the method presented in this thesis will serve as a valuable tool in the screening of the influential parameters on the size of protein-polyelectrolyte complexes. In addition, it is worth mentioning that in the field of vaccine product development protein-polyelectrolyte complexes form an important formulation platform¹⁵. The structural interplay between antigen and adjuvant in a vaccine formulation resembles same sort of interactions as mentioned above. Therefore, characterizing the interaction of these macromolecules is crucial for the vaccine potency¹⁶.

Our application of the two different flow imaging microscopy techniques for drug delivery systems such as PLGA microparticles shows that the described methods can be of more value than porosity determination only. The counting and imaging of the particles in suspension brings an important advantage, namely getting information on the morphology and size distribution of PLGA microparticles. The high-resolution images of FlowCAM result in a high number of observable morphological parameters. In comparison with MFI, FlowCAM is a more flexible system, where the operator can practically change any setting or aspect of the instrument. The high imaging/analysis efficiency of the MFI can be advantageous when rapid and accurate size distribution of the particles is needed. MFI is more user-friendly when it comes to the execution of the analysis. Also the supported data acquisition mode, MVAS, has certain features (e.g., removing stuck particles) that improve the counting accuracy.

In the development of drug delivery systems there is a need for exploratory studies to investigate if the platforms in development can be applicable to obtain a target product profile for the drug of interest. Quality-by-Design (QbD) approaches may facilitate development of controlled release products, by understanding the impact of the properties of material

components and manufacturing process on the product quality¹⁷. One of the tools in QbD is the implementation of process analytical technologies (PAT) during the development. The latter concern systems that allow designing, analyzing and controlling the manufacturing process, through timely measurements during processing¹⁸. In this context, systems such as FlowCAM ES[®] can automatically extract, dilute and run samples from within the production or processing line¹⁹. This speeds up the production process and delivers continuous data to monitor the process and keep track of the quality of the (intermediate) product.

In addition to using flow imaging microscopy for PLGA microparticles, the sedimentation method itself may already be of interest for other types of complex injectable formulations, e.g., for the determination of the density of the proteinaceous particles. The density of protein aggregates is frequently used to recalculate the number of micron size aggregates into mass of protein. In addition, resonant mass measurement (RMM) requires the density of aggregates in order to convert the buoyancy of the aggregate into an equivalent circular diameter²⁰. Although attempts have been made to determine the aggregate density by RMM itself²¹, the technique does not allow determination of the density of aggregates above 5 μm . With the sedimentation based method where we use fluids with different density, one could possibly attain the density of protein particles larger than 5 μm .

The last part of this thesis on counting and viability determination of cells (*Chapter 6*) opens a whole new field in the application list of flow imaging microscopy. In the cell therapy field knowledge about formulation development is very preliminary, and the availability of robust analytical tools that provide cell counts and various morphological characteristics can be of great value. In addition, the capability of flow imaging microscopy for cell product characterization may be broader than we have shown in our study. High-resolution images of FlowCAM may have added value for discrimination of different cells or perhaps a single cell at different stages of its differentiation. Moreover, certain FlowCAM models have a fluorescence detector that may open new opportunities to analyze fluorescently labeled cells. This option may increase the potential of flow imaging microscopy for the characterization of cell therapy products. The new application field for flow imaging microscopy that we introduced in *Chapter 6* is possibly useful directly in a clinical setting. In addition, flow imaging microscopy methods could be implemented to test the pharmaceutical quality of protein drugs as well as classical parenteral drug dosage forms that are manufactured aseptically in hospitals.

References

1. Leader B, Baca QJ, Golan DE 2008. Protein therapeutics: a summary and pharmacological classification. *Nature reviews Drug discovery* 7(1):21-39.
2. Pisal DS, Kosloski MP, Balu-Iyer SV 2010. Delivery of therapeutic proteins. *Journal of*

pharmaceutical sciences 99(6):2557-2575.

3. Mason C, Brindley DA, Culme-Seymour EJ, Davie NL 2011. Cell therapy industry: billion dollar global business with unlimited potential. *Regen Med* 6(3):265-272.
4. Carpenter JF, Randolph TW, Jiskoot W, Crommelin DJ, Middaugh CR, Winter G, Fan YX, Kirshner S, Verthelyi D, Kozlowski S, Clouse KA, Swann PG, Rosenberg A, Cherney B 2009. Overlooking subvisible particles in therapeutic protein products: gaps that may compromise product quality. *Journal of pharmaceutical sciences* 98(4):1201-1205.
5. He Y, Park K 2016. Effects of the Microparticle Shape on Cellular Uptake. *Molecular pharmaceuticals* 13(7):2164-2171.
6. Bravery CA, Carmen J, Fong T, Oprea W, Hoogendoorn KH, Woda J, Burger SR, Rowley JA, Bonyhadi ML, Van't Hof W 2013. Potency assay development for cellular therapy products: an ISCT review of the requirements and experiences in the industry. *Cytotherapy* 15(1):9-19.
7. Smoluchowski M 1916. Drei Vorträge über Diffusion, Brownsche Molekularbewegung und Koagulation von Kolloidteilchen. *Physikalisch Zeitschrift* 17:28.
8. Rios Quiroz A, Lamerz J, Da Cunha T, Boillon A, Adler M, Finkler C, Huwyler J, Schmidt R, Mahler HC, Koulov AV 2016. Factors Governing the Precision of Subvisible Particle Measurement Methods - A Case Study with a Low-Concentration Therapeutic Protein Product in a Prefilled Syringe. *Pharmaceutical research* 33(2):450-461.
9. Li Y, Roberts CJ. 2010. Protein Aggregation Pathways, Kinetics, and Thermodynamics. In Wang W, Roberts CJ, editors. *Aggregation of therapeutic proteins*, ed.: John Wiley & Sons. p 40.
10. Kalonia C, Kumru OS, Prajapati I, Mathaes R, Engert J, Zhou SX, Middaugh CR, Volkin DB 2015. Calculating the Mass of Subvisible Protein Particles with Improved Accuracy Using Microflow Imaging Data. *Journal of pharmaceutical sciences* 104(2):536-547.
11. Clark KM, Glatz CE 1987. Polymer dosage considerations in polyelectrolyte precipitation of protein. *Biotechnol Progr* 3:6.
12. Cooper CL, Dubin PL, Kayitmazer AB, Turksen S 2005. Polyelectrolyte-protein complexes. *Curr Opin Colloid In* 10(1-2):52-78.
13. Kizilay E, Kayitmazer AB, Dubin PL 2011. Complexation and coacervation of polyelectrolytes with oppositely charged colloids. *Adv Colloid Interfac* 167(1-2):24-37.
14. Kohane DS 2007. Microparticles and nanoparticles for drug delivery. *Biotechnol Bioeng* 96(2):203-209.
15. Amidi M, Mastrobattista E, Jiskoot W, Hennink WE 2010. Chitosan-based delivery systems for protein therapeutics and antigens. *Adv Drug Deliv Rev* 62(1):59-82.
16. Fox CB, Kramer RM, Barnes LV, Dowling QM, Vedvick TS 2013. Working together: interactions between vaccine antigens and adjuvants. *Therapeutic Advances in Vaccines* 1(1):13.
17. Patil SD, Burgess, D.J. 2010. Pharmaceutical development of modified-release parenteral

dosage forms using bioequivalence (BE), Quality by Design (QbD), and In Vitro In Vivo Correlation (IVIVC) principles. In Shargel L, Kanfer, I., editor Generic drug product development speciality dosage forms, ed., New York: Informa Healthcare USA, Inc. p 26.

18. Zidan AS, Habib MJ, Khan MA 2008. Process analytical technology: nondestructive evaluation of cyclosporine A and phospholipid solid dispersions by near infrared spectroscopy and imaging. *Journal of pharmaceutical sciences* 97(8):3388-3399.

19. Technologies R. 2016. Imaging Particle Analysis System for On-Line Analysis of Particulates in Process Fluids. ed., <http://www.ri.co.th/ipa-flowcam-es>.

20. Zolls S, Weinbuch D, Wiggernhorn M, Winter G, Friess W, Jiskoot W, Hawe A 2013. Flow imaging microscopy for protein particle analysis--a comparative evaluation of four different analytical instruments. *The AAPS journal* 15(4):1200-1211.

21. Folzer E, Khan TA, Schmidt R, Finkler C, Huwyler J, Mahler HC, Koulov AV 2015. Determination of the Density of Protein Particles Using a Suspended Microchannel Resonator. *Journal of pharmaceutical sciences* 104(12):4034-4040.

Appendices

Nederlands samenvatting

Complexe injecteerbare formuleringen, zoals therapeutische eiwitten, gereguleerde-afgiftesystemen en celtherapieproducten, nemen een steeds belangrijkere positie in bij de behandeling van vele levensbedreigende ziektes. Vrijwel alle complexe injecteerbare formuleringen hebben als gemeenschappelijk kenmerk dat niet-zichtbare deeltjes (NZD; deeltjes met een grootte van ongeveer 1 – 100 μm) een kritisch kwaliteitskenmerk van het product zijn. De meeste therapeutische eiwitproducten zijn vloeibare of gevriesdroogde formuleringen waarin de aanwezigheid van NZD ongewenst is; vele injecteerbare gereguleerde afgiftesystemen zijn gebaseerd op NZD; en cellen zijn levende NZD. Met de voortdurende verbetering van bestaande en nieuwe deeltjesanalysetechnieken, is het van belang om de toepasbaarheid van deze *tools* voor de karakterisering van complexe injecteerbare formuleringen te onderzoeken. Daarom was het doel van dit proefschrift om methodes te ontwikkelen voor karakterisering van farmaceutisch relevante NZD, op basis van *state-of-the-art* deeltjesanalysetechnieken.

Eiwitaggregatie geïnduceerd door roeren is een fenomeen dat in verschillende stadia van de productie van biologische farmaceutische producten plaats kan vinden. In **Hoofdstuk 2** hebben we de oorzaak van eiwitaggregatie als gevolg van roeren onderzocht. Hiervoor hebben we een roersysteem ontworpen waarmee het contact tussen roermagneet en glasbodem gemanipuleerd kon worden. Uit metingen met *nanoparticle tracking analysis* (NTA) bleek dat het contact tussen roermagneet en glasbodem cruciaal is voor het induceren van eiwitaggregatie. Tijdens het roeren van een monoklonaal IgG-oplossing werden aanvankelijk submicron eiwitaggregaten (100 – 1000 nm) gevormd, welke na verloop van tijd in aantal en grootte toenamen, hetgeen resulteerde in de vorming van NZD, zoals geanalyseerd met *Micro-Flow Imaging* (MFI). Uit *size-exclusion chromatography* (SEC) analyses bleek dat de hoeveelheid oligomeren niet toenam, wat aangaf dat de submicron eiwitaggregaten zeer snel gevormd werden. In dezelfde studie hebben we aangetoond dat de mate van aggregatie toeneemt bij een vergroting van het contactoppervlak tussen roermagneet en glasbodem en een verhoging van de druk uitgeoefend op de glasbodem tijdens het roeren. Aggregatie tijdens het roeren kon worden voorkomen door toevoeging van polysorbaat 20 of door te roeren zonder dat contact tussen de roerstaaf en de glasbodem. Met de uitkomst van deze studie hebben we nieuwe inzichten gecreëerd in het mechanisme van eiwitaggregatie als gevolg van roeren. Bovendien hebben we oplossingen aangedragen om deze vorm van eiwitaggregatie te onderdrukken door het proces of de formulering te optimaliseren.

In **Hoofdstuk 3** hebben we door SEC, NTA en MFI te combineren nieuwe inzichten verkregen in de kinetiek en het mechanisme van complexvorming tussen een eiwit en een polyelektrolyet. In dit onderzoek hebben we monoklonaal IgG en dextranulfaat

als respectievelijk model eiwit en polyelektrolyet gebruikt. Een mengsel van gelijke concentraties (op basis van massa) van IgG en dextran-sulfaat werd bereid en voorzichtig gehomogeniseerd. Monsters werden op verschillende momenten uit het mengsel genomen, geanalyseerd op hoeveelheid monomeer (niet gecomplexeerd) eiwit en hoeveelheid nano- en microdeeltjes. Uit SEC-analyse bleek dat direct na het mengen van de twee oplossingen er geen eiwit in monomere vorm meer in de oplossing aanwezig was. Het eiwit bleek gecomplexeerd te zijn in nanodeeltjes, zoals bleek uit NTA, waarmee de concentratie en de afmeting van de deeltjes bepaald konden worden. Daarna nam de hoeveelheid van deze deeltjes af en werd hun gemiddelde deeltjesgrootte steeds groter. Na 1.5 uur werden de eerste microdeeltjes met MFI gedetecteerd, en ook deze namen toe in grootte en namen af in aantal. Met behulp van het perikinetische coagulatiemodel van Smoluchowski hebben we de veranderingen in deeltjesconcentratie mathematisch kunnen modelleren, waarmee we vervolgens de zogenaamde *sticking probability* van IgG-dextran-sulfaatcomplexen hebben afgeleid. De *sticking probability* is gerelateerd aan de interactie tussen de eiwit-polyelektrolyetcomplexen en kan dus helpen bij het bepalen van de groeisnelheid van dit soort complexen. We verwachten dat deze combinatie van deeltjesanalysetechnieken ook voor andere systemen gebruikt kan worden, zoals complexvorming van polymeren met eiwitten, DNA en andere biomacromoleculen.

De porositeit van PLGA-microdeeltjes is een van de kritische parameters die bepalend zijn voor de afbraaksnelheid van het deeltje en het vrijkomen van het geneesmiddel. Onze studie in **Hoofdstuk 4** beschrijft een nieuwe methode waarmee de porositeit van dit soort deeltjes bepaald kan worden, namelijk door het meten van de sedimentatiesnelheid van gesuspendeerde deeltjes met behulp van een *flow imaging microscope*. Twee op sedimentatie gebaseerde methoden werden onderzocht. In de eerste methode werd de sedimentatiesnelheid van deeltjes in vloeistoffen van verschillende dichtheden bepaald. Hierna, hebben we geïnter- of geëxtrapoleerd naar een sedimentatiesnelheid van nul. De vloeistofdichtheid die met het nulpunt overeenkwam werd beschouwd als de dichtheid van het betreffende deeltje. Deze waarde voor de dichtheid werd dan gebruikt om de porositeit, door middel van de bekende deeltjessamenstelling en de dichtheden van de grondstoffen van het deeltje, te bepalen. In de tweede methode hebben we deeltjesgrootte en sedimentatiesnelheid van individuele deeltjes in een vloeistof met bekende dichtheid gemeten. Vervolgens werd de dichtheid van individuele deeltjes berekend aan de hand van de wet van Stokes, waaruit daarna de porositeit werd berekend. In dit onderzoek hebben we de verschillende factoren die van invloed zijn op het resultaat bestudeerd en de methoden met behulp van polystyreenstandaarddeeltjes gevalideerd. Vervolgens hebben we de porositeit van verschillende batches van PLGA microdeeltjes bepaald. De gevonden waarden kwamen goed overeen met de door middel van *mercury intrusion porosimetry*

(MIP) bepaalde porositeiten.

In **Hoofdstuk 5** hebben we een andere methode geïntroduceerd waarmee de porositeit van PLGA-microdeeltjes door middel van MFI kunnen worden bepaald. In dit geval hebben we een bekende massa van microdeeltjes in een vloeistof gesuspenseerd en hebben het totale volume aan deeltjes in de gehele suspensie nauwkeurig bepaald. De schijnbare dichtheid van de deeltjes kon gemakkelijk berekend worden door de massa/volume verhouding. Samen met het bekende samenstelling van het deeltje en de dichtheid van de grondstoffen, konden we de porositeit van het deeltje afleiden. Parameters die van invloed waren op de nauwkeurigheid van de methode, zoals concentratie van deeltjes, vloeistofdichtheid en adsorptie van deeltjes aan het oppervlak van de beker en buizen van het instrument, werden met behulp van PMMA-deeltjes onderzocht. Deze parameters werden vervolgens geoptimaliseerd voor de porositeitsbepaling van 7 verschillende batches van PLGA-microdeeltjes. De resultaten van al deze batches kwamen goed overeen met de door middel van MIP bepaalde porositeiten. De uitkomst van deze studie laat zien dat beide methoden geschikt zijn voor het bepalen van de porositeit van PLGA-microdeeltjes, met als voordeel dat hiervoor slechts enkele milligrammen microsferen nodig zijn.

In **Hoofdstuk 6** hebben we de toepasbaarheid van *flow imaging microscopy* (MFI and FlowCAM) voor het tellen van cellen in suspensie en het bepalen van hun levensvatbaarheid bestudeerd. In dit onderzoek hebben we *B-lineage* leukemiecellen afkomstig van twee verschillende donoren gedurende enkele dagen aan omgevingsomstandigheden blootgesteld, om daarmee afname in levensvatbaarheid te veroorzaken. Gedurende deze incubatieperiode hebben we op verschillende momenten monsters met MFI, FlowCAM, hemocytometrie en een geautomatiseerde cellenteller (TC-20) gemeten. De resultaten van beide *flow imaging microscopy* technieken lieten veranderingen in celmorfologie als functie van de incubatietijd zien, zoals bleek uit een aantal morfologische parameters. Door middel van *fluorescence assisted cell sorting* (FACS) waren we in staat om de dode en levende cellen te scheiden en deze in suspensie op te vangen. De morfologische parameters van de gescheiden dode en levende cellen werden met MFI en FlowCAM bepaald, om zodoende softwarefilters te ontwikkelen die onderscheid kunnen maken tussen dode en levende cellen in een onbekende celsuspensie. Hiermee bleek het mogelijk om met *flow imaging microscopy* levensvatbaarheidspercentages te verkrijgen die overeenkwamen met de waarden verkregen via gebruikelijke methoden (hemocytometrie en TC-20). Bovendien bleken de celconcentraties zoals bepaald met MFI, FlowCAM, hemocytometrie en TC-20 goed overeen te komen, waarbij de reproduceerbaarheid van MFI en FlowCAM superieur waren ten opzichte van hemocytometrie en TC-20.

List of publications

Sedq AS, Kubbinga M, Langguth P, Dressman J. 2014. The impact of the EMA change in definition of “dose” on the BCS dose-solubility ratio: a review of the biowaiver monographs. *J Pharm Sci* 103(1): 65-70.

Sedq AS, Nejadnik MR, El Bialy I, Witkamp GJ, Jiskoot W. 2015. Protein-polyelectrolyte interactions monitoring particle formation and growth by nanoparticle tracking analysis and flow imaging microscopy. *Eur J Pharm Biopharm* 93:339-345.

Sedq AS, van Duijvenvoorde RB, Jiskoot W, Nejadnik MR. 2016. No touching! Abrasion of adsorbed protein is the root cause of sub-visible particle formation during stirring. *J Pharm Sci* 105(2): 519-29.

Haji Abdolvahab M, Fazeli A, Halim A, Sedq AS, Fazeli MR, Schellekens H. 2016. Immunogenicity of recombinant human interferon beta-1b in immune-tolerant transgenic mice corresponds with the biophysical characteristics of aggregates. *J Interferon Cytokine Res* 36(4): 1-11.

Sedq AS, Waasdorp S, Nejadnik MR, van Beers MMC, Meulenaar J, Verrijk R, Jiskoot W. 2017. Determination of the porosity of PLGA microparticles by tracking their sedimentation velocity using a flow imaging microscope (FlowCAM). *Pharm Res* 34(4): 1-11

Jiskoot W, Nejadnik MR, Sedq AS. Potential issues with the handling of biologicals in a hospital. *J Pharm Sci*, manuscript accepted for publication.

Curriculum vitae

Ahmad Sediq was born on February 12th 1985 in Kabul, Afghanistan. In September 2004 he started his bachelor study in Pharmaceutical Sciences at Antwerp University, Belgium. After receiving his BSc diploma in 2008 Ahmad Sediq followed a year of pre-master before starting his master study in Pharmacy at Utrecht University, the Netherlands. During his research internship performed at Solvay Pharmaceuticals in Weesp, Ahmad Sediq developed dissolution based methods for characterization of active pharmaceutical ingredients. Ahmad Sediq gained his MSc diploma in 2012, thereafter he started his PhD project in September 2012 under supervision of Prof. Dr. Wim Jiskoot at the Leiden Academic Centre for Drug Research (LACDR) and Prof. Dr. Geert Jan Witkamp from Technical University Delft, the Netherlands. The PhD project was part of an STW project on controlled release of protein pharmaceuticals from biodegradable, hydrophilic microcapsules produced by supercritical fluid processing. Since October 2016 Ahmad Sediq works as a scientist in the Drug Product Development group of Janssen Vaccines & Prevention in Leiden.

